Towards improving the land-surface-atmosphere coupling in the Dutch Atmospheric Large-Eddy Simulation model (DALES).

Maurice Van Tiggelen

Master thesis - May 31, 2018

TU Delft - *Geoscience and Remote Sensing*
Grenoble INP ENSE3 - *Hydraulics, Civil & Environmental Engineering*

Grenoble INP ENSE3 TU Delft

Cover picture: CESAR meteorological observatory in Cabauw (Netherlands) on 08/06/2017, and imaginative view of the subsurface.

Towards improving the land-surface-atmosphere coupling in the Dutch Atmospheric Large-Eddy Simulation model (DALES).

by

Maurice Van Tiggelen

in partial fulfilment of the requirements for the degrees of

Master of Science
in *Geoscience and Remote Sensing*
at the Delft University of Technology,

and

Diplôme National d'Ingénieur
in *Hydraulic, Civil & Environmental Engineering*
at the Ecole Nationale Supérieure de l'Energie, l'Eau et l'Environnement,
Grenoble Institute of Technology

to be defended publicly in Delft on Thursday May 31, 2018

Student number: 4515129

Supervisor:	Dr. S. R. de Roode,	TU Delft
Thesis committee:	Prof. dr. A. P. Siebesma,	TU Delft
	Prof. dr. ir.. B. J. H. van de Wiel,	TU Delft

An electronic version of this thesis is available at `http://repository.tudelft.nl/`.

Grenoble INP ENSE3 TU Delft

Abstract

This report proposes improvements of the land surface model (LSM) used in the turbulence-resolving Dutch Atmospheric Large-Eddy Simulation model (DALES). Important changes include the infiltration of precipitation, the parametrization of the soil hydraulic functions and the formulation of the soil water extraction by vegetation roots. The performance of the improved LSM version is validated using offline simulations and observations from the CESAR meteorological observatory in Cabauw (Netherlands), during the year of 2015. An optimal parameter set for this location set is obtained from both satellite retrievals and in-situ observations. In particular, the seasonal dependence of both the Leaf Area Index (LAI) and the roughness lengths for heat and momentum is prescribed to the model.

The offline simulations determined that the improved version of the LSM is able to model the surface fluxes during the year of 2015 with an accuracy of 10 W/m^2. This accuracy was found to be strongly dependent on the chosen land surface parameters such as the LAI, the roughness lengths, the soil textures and the vegetation root profiles. Furthermore, the lower boundary for soil water transfer, set to free drainage, was found to cause too much vegetation stress after an extended simulation time.

Finally, the LSM is tested in a fully-coupled mode during three different meteorological events observed at the CESAR observatory. Firstly, stratocumulus simulations confirm the importance of the surface evaporation on the development of the stratocumulus layer, which is considerably reduced compared to simulations that assume the surface to be saturated with water. Secondly, the growth of the clear convective boundary layer was found to be greatly affected by the partitioning of the surface fluxes, as the sensible heat flux plays a key role in entrainment. Although the modelled sensible heat flux was found to be in agreement with the observations, the growth of the boundary layer was still substantially underestimated. Lastly, it was found that it is possible to model the main development stages of radiation fog in DALES, despite the fact that the modelled fog layer appears to be too persistent.

Résumé

Ce rapport propose des améliorations du modèle de surface terrestre (LSM) utilisé dans le modèle de simulation des Grandes Échelles de la turbulence atmosphérique DALES. Les modifications concernent l'infiltration de la précipitation dans le sol, le paramétrage des propriétés du sol et la formulation de l'extraction de l'eau dans le sol par les racines de la végétation. La performance du LSM est validée par des simulations découplées de l'atmosphère en utilisant des observations de l'observatoire météorologique CESAR à Cabauw (Pays-Bas) durant l'année de 2015. Un ensemble optimal de paramètres de surface pour cette location est obtenu à partir de méthodes de télédétection spatiale et de mesures in-situ. En particulier, la variation saisonnière de l'indice de surface foliaire (LAI) et des longueurs de rugosité est prescrite au modèle.

Les simulations découplées ont déterminé que la nouvelle version du LSM est capable de modéliser les flux turbulents à la surface pendant l'année de 2015 avec une précision de 10 W/m^2. La précision dépend fortement des valeurs numériques choisies pour les paramètres de surface tels que le LAI, les longueurs de rugosité, la texture du sol et la profondeur des racines dans le sol. De plus, il s'est avéré que la condition limite du transport d'eau dans le sol, fixé en écoulement libre, cause trop de stress de la végétation après une période de simulation prolongée.

Le LSM est ensuite testé en couplage avec l'atmosphère pendant trois phénomènes météorologiques différents observés au site CESAR. Tout d'abord, des simulations de stratocumulus confirment l'importance de l'évaporation à la surface sur le développement de la couche de stratocumulus, qui est d'ailleurs considérablement réduite comparée à des simulations qui supposent que la surface est saturée en eau. Ensuite, il a été constaté que la croissance de la couche limite convective sans nuages est considérablement affectée par le partitionnement des flux turbulents à la surface, dû au fait que le flux de chaleur sensible joue un rôle majeur dans l'entraînement atmosphérique. Bien que le flux de chaleur sensible modélisé s'avère très proche des observations, la croissance de la couche limite demeure tout de même fortement sous-estimée dans le modèle. Enfin, ce travail a démontré qu'il est possible de modéliser les principales phases d'évolution du brouillard radiatif dans DALES, bien qu'il s'est avéré que la couche de bouillard demeure trop persistante.

Samenvatting

Dit rapport stelt verbeteringen voor van het landoppervlakte model (LSM) die wordt gebruikt in het Dutch Atmospheric Large-Eddy Simulation (DALES) turbulentie-model. De belangrijke veranderingen bevatten de infiltratie van regen in de bodem, de parametrisatie van de bodemeigenschappen en de formulering van de extractie van bodemwater door de wortels van de vegetatie. De prestatie van het verbeterde LSM is gevalideerd met simulaties zonder koppeling met de atmosfeer, dankzij metingen van het CESAR meteorologisch observatorium in Cabauw (Nederland) tijdens het jaar 2015. Een optimale reeks van parameters voor deze locatie is afgeleid van satelliet remote-sensing en van in-situ observaties. Met name wordt de jaarlijkse gang van de bladoppervlakte-index (LAI) en van de ruwheidslengte voorgeschreven in het model.

De losgekoppelde simulaties hebben aangetoond dat het verbeterde LSM de oppervlakte turbulente fluxen tijdens het jaar 2015 kan modelleren met een nauwkeurigheid van 10 W/m^2. Deze nauwkeurigheid is erg afhankelijk van de gekozen waardes van de invoerparameters, zoals de LAI, de ruwheidslengte, de bodemeigenschappen en de diepte van de wortels van de vegetatie. Verder blijkt ook dat de bodem te veel water verliest, waardoor er te veel vegetatie stress komt te ontstaan na een langere simulatie tijd.

Het model is tenslotte gekoppeld met de atmosfeer en getest tijdens drie dagen met verschillende meteorologische verschijnselen, geobserveerd op het CESAR-observatorium. Ten eerste, stratocumulus simulaties bevestigen het belang van de verdamping bij het landoppervlak op de ontwikkeling van de stratocumulus laag, die overigens beperkt is ten opzichte van simulaties die ervan uit gaan dat de oppervlakte verzadigd is met water. Ten tweede, er wordt geconstateerd dat de groei van de convectieve grenslaag behoorlijk afhankelijk is van de verdeling van de turbulente fluxen aan het oppervlak, omdat de sensibele warmteflux een hoofdrol speelt in atmosferische menging. De groei van de grenslaag wordt onderschat in het model, ondanks het feit dat het sensibele warmteflux erg dicht bij de waarnemingen ligt. Ten laatste, dit rapport bewijst dat de belangrijkste ontwikkelingsfases van stralingsmist gemodelleerd kunnen worden in DALES, hoewel de mistlaag toch te langdurig blijkt te zijn.

Acknowledgements

This research would not have been possible without the help of many persons. In particular, I would like to thank my supervisors; Stephan, for his great availability, boundless enthusiasm and flawless guidance; and Pier for the regular discussions, the good advice, and for sharing the bigger picture when needed. Without their fascination for atmospheric modelling I would probably never have chosen a master thesis topic in this field. I would also like to thank Bas for the discussion and for taking the time reading this research, Louise for the useful advice, especially concerning scientific communication, Erwin for the help with the IT hard-and software and finally Christine for the encouraging conversations. I would also like to express my gratitude towards my master thesis tutor in Grenoble, Julien Chauchat, for his flexibility, and for taking the time to assess the quality of this report.

After one year of working on my master thesis at the department of Geoscience and Remote Sensing, at TU Delft, I've had the pleasure to work alongside some truly inspiring PhD students. I would like to thank all of them for sharing with me their PhD experience, and for giving me some advice when it was most needed.

This work did not only involve people in Delft. I want to thank in particular Fred Bosveld and Henk Klein Baltink from the KNMI for the help with the data from Cabauw and De Bilt, and all the KNMI staff I had the pleasure to discuss with during my visits in De Bilt. Thanks also to Prof. Jordi Vila-Guerau de Arellano from Wageningen University for giving me the opportunity to take part in the Boundary layer and turbulence BBOS workshop, and to Chiel van Heerwaarden, Prof. Harm Jonker and to the other participants from the workshop for the good discussions.

Finally, this master thesis was also greatly supported by my friends and family, both in France and in the Netherlands, who were patient enough during the busy periods, but who were there when I needed to take a break from running simulations and solving (complex?) problems. For this, thank you! And special thanks to my father for giving me (a lot of) valuable comments on the initial manuscript.

Contents

1 Introduction

The Earth's land surface is at the centre of many practical applications, such as agriculture, water management, numerical weather prediction and climate modelling (Seneviratne et al., 2010). From a scientific perspective, the land surface imposes the boundary conditions for heat and water transport processes in both the soil and in the atmosphere, and influences the Earth system as a whole through many feedback mechanisms. However, there is still an important uncertainty in the global estimation of the surface turbulent fluxes for atmospheric modelling purposes, especially under climate change, due to the lack of observations (Stephens et al., 2012).

The field of land surface modelling lies at the cross-section between atmospheric physics, soil physics and vegetation behaviour science, which causes some challenges due to the different timescales at which the physical processes take place. For instance, cloud coverage strongly affects vegetation activity within seconds through shading of available photosynthetic active radiation (Vilà-Guerau de Arellano et al., 2014). On the other hand, seasonal precipitation patterns and diffusive processes in the soil affect the long-term vegetation activity (Porporato et al., 2001). Hence, different practical applications or research objectives may require different modelling approaches that strongly differ by the space and time scales they aim to represent.

In this report, emphasis is given on the performance and on the necessary improvements of the land surface model (LSM) that is used to model the surface fluxes in the turbulence-resolving Dutch Atmospheric Large-Eddy Simulation (DALES) model (Heus et al., 2010).

Research aims

The main ambition of this research is to assess the performance of the default Land Surface Model (LSM) version used in the Dutch Atmospheric Large-Eddy Simulation (DALES) model. Necessary modifications will be implemented in order to improve the modelled surface fluxes in DALES on top of the short grassland at the CESAR meteorological observatory in the Netherlands (Russchenberg, 2005), and for time-scales ranging from seconds up to one year. The modifications in the LSM will allow us to answer the following three main research questions:

- *How well does the LSM in DALES model the surface fluxes at the CESAR observatory ?*

This will be quantified by using the modified LSM in a offline mode, meaning that the observed atmospheric conditions are prescribed to the LSM. The modelled surface fluxes are not routed back to the atmosphere and are compared to the observations from the CESAR observatory.

- *What are the important land surface parameters, and how accurate are their default values ?*

For this purpose, we will use both in-situ observations and satellite remote sensing retrievals to derive some land surface parameters at the CESAR observatory for the year of 2015. We will also perform offline sensitivity simulations to identify the weaknesses of a default version of the LSM, that uses tabulated values for the land surface parameters.

- *How do coupled LES-land surface results compare to observations at the CESAR observatory ?*

To this end, the LSM will be switched on for coupled land-atmosphere simulations in DALES, and the performance of the modified LSM will be tested with the aid of observations during three different meteorological cases: the development of stratocumulus, the growth of the clear convective boundary layer and finally the evolution of radiation fog.

Outline

This report is subdivided in six different chapters. The introduction was given in Chapter 1. Chapter 2 describes in detail the land surface model that is currently implemented in DALES and in Chapter 3, the important changes in the model are described. In Chapter 4, different in-situ and remote sensing observations are used to derive important land surface parameters for the CESAR observatory. These parameters are used for the offline land surface simulations, presented in Chapter 5. Finally, the results of the online simulations during three different cases observed at the CESAR observatory are presented in Chapter 6, and the final conclusions can be found in Chapter 7.

2 Model description

A land surface model (LSM) estimates how the net radiative energy received at the land surface is partitioned into turbulent fluxes of heat and moisture into the atmosphere and a heat flux into the soil, depending on the state of the soil and of the vegetation. Sub-surface processes, such as soil heat and water transport, are explicitly resolved, as they affect the heat flux from deeper levels to the surface and the amount of water available for vegetation activity (see figure 2.1).

Here we will give a detailed description of the land surface model that is already implemented in DALES4.1, and which we will call the 'default' version. The modifications of the model will be given in detail in a different chapter.
The default version of the model used in this report is a modified version of the Tiled European Centre for Medium-Range Weather Forecasts (ECMWF) Scheme for Surface Exchanges over Land (TESSEL) (full details are available in ECMWF (2017)), and was implemented in DALES by Chiel van Heerwaarden (WUR).

The first part describes the model equations used to calculate the tendencies of the soil moisture content and the soil temperature. Then, the surface energy balance equation that connects the soil and the atmosphere is presented. Finally, a short description of the modelled atmospheric processes is given.

2.1. Sub-surface processes

The soil in the first meters below the surface may in most cases be considered as a porous medium in which water diffusion occurs due to gradients of pressure- and gravity- forces. In reality, many processes take place, from small-scale molecular diffusion and vegetation root water extraction to large-scale gravity drainage, phase changes and infiltration of precipitation. To avoid the increasing complexity that comes with numerically solving for the three-dimensional transport processes in heterogeneous soils, some simplifying assumptions are used in this model:

- The soil is a homogeneous, unsaturated, porous medium;
- Heat and water are only transported vertically;
- There are no phase changes in the soil (e.g freezing, thawing,...);

These simplifying assumptions enable the definition of the porosity θ_{sat}, defined as the proportion of pore volumes in a volume of soil:

$$\theta_{sat} = \frac{V_v}{V_s} \tag{2.1}$$

where V_v is the volume of pore spaces and V_s the total volume of the soil. Porosity is the maximum volume of water that can be stored in a volume of soil, and it is usually higher close to the surface due to biological activity and ranges from 0.3 for coarse soils and sand to 0.8 in organic soils (Dingman, 2015, chap. 7). Typical values for the CESAR observatory are found in table 3.1.

In practice, the soil layers close to the surface are not saturated with water, so they have a volumetric water content smaller than porosity :

$$\theta = \frac{V_w}{V_s} \leq \theta_{sat} \tag{2.2}$$

where V_w is the volume of water contained in the soil.

2.1.1. Soil heat transfer

A gradient of heat flux must lead to local heating, expressed by the following equation of conservation of energy:

$$\frac{\partial T}{\partial t} = -\frac{1}{(\rho C)_{\text{soil}}} \frac{\partial F_T}{\partial z'} \tag{2.3}$$

where T is the soil temperature, z' is the vertical coordinate taken positive downwards and $(\rho C)_{\text{soil}}$ is the volumetric soil heat capacity (J/m^3/K). The subscript 'T' is used for the terms that are related to temperature diffusion. Numerical values are written in table 2.1. The flux of vertical heat diffusion is described by Fourier's law:

$$F_T = -\lambda_T \frac{\partial T}{\partial z'} \tag{2.4}$$

and λ_T is the soil heat conductivity (W/m/s). The heat flux F_T (W/m^2) is defined positive downwards.

Using the expression for the heat flux F_T in the heat

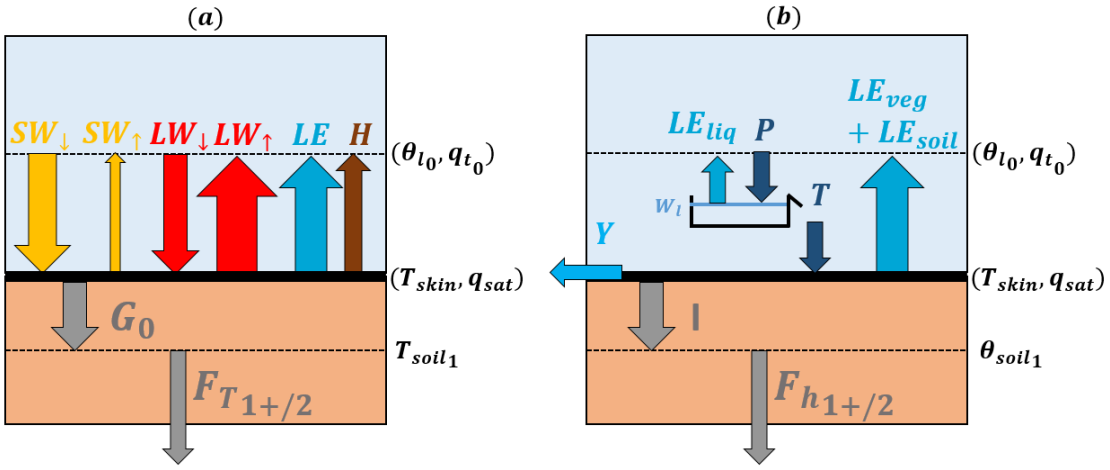

Figure 2.1: (a) Modelled surface energy balance and (b) modelled surface water balance. The relative size and orientation of the fluxes are shown for typical summer daytime at the CESAR meteorological observations site. The vertical soil heat and water fluxes are shown at the bottom.

conservation equation 2.3 yields a 1D diffusion equation for the vertical temperature profile, numerically solved in the LSM:

$$\frac{\partial T}{\partial t} = \frac{1}{(\rho C)_{\text{soil}}} \frac{\partial}{\partial z'} \left(\lambda_T \frac{\partial T}{\partial z'} \right) \tag{2.5}$$

The soil thermal conductivity depends on the volumetric water content and on the bulk properties of the soil (Farouki, 1981, chaps. 3-4-5). The following method is used for the parametrization of the volumetric soil heat capacity and soil heat conductivity (see Peters-Lidard et al. (1998) and Johansen (1977)):

$$(\rho C)_{\text{soil}} = (1 - \theta_{\text{sat}})(\rho C)_{\text{dry}} + \theta (\rho C)_{\text{water}}, \tag{2.6}$$

$$\lambda_T = Ke(\lambda_{T,\text{sat}} - \lambda_{T,\text{dry}}) + \lambda_{T,\text{dry}} \tag{2.7}$$

where $(\rho C)_{\text{dry}}$ and $(\rho C)_{\text{water}}$ are the heat capacities of a dry soil and water, respectively. The quantities $\lambda_{T,\text{sat}}$ and $\lambda_{T,\text{dry}}$ are the heat conductivities of a soil at saturation and of a dry soil respectively, and Ke is the Kersten number, defined as:

$$Ke \equiv \log_{10} \left[\max \left(0.1, \frac{\theta}{\theta_{\text{sat}}} \right) \right] + 1 \tag{2.8}$$

The heat conductivity of a soil at saturation is calculated as:

$$\lambda_{T,\text{sat}} = \lambda_{T,\text{s}}^{1-\theta} \lambda_{T,\text{water}}^{\theta} \tag{2.9}$$

where $\lambda_{T,\text{s}}$ is the effective solids thermal conductivity, which contains the contribution of the quartz and all the other minerals (Farouki, 1981, p.69-72). The quantity $\lambda_{T,w}$ is the heat conductivity of water.

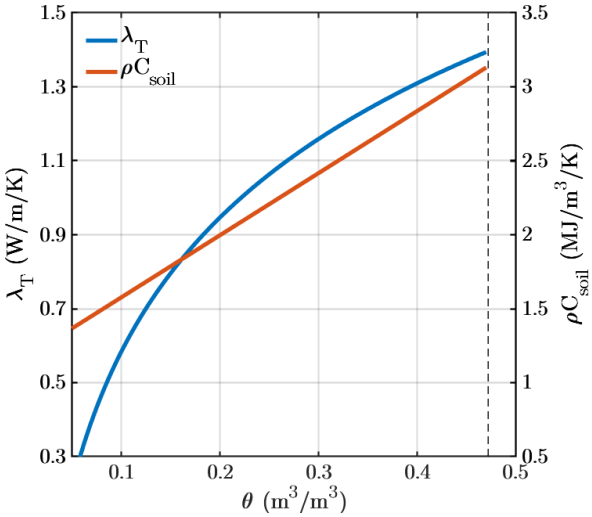

Figure 2.2: Parameterized heat conductivity (blue) and volumetric heat capacity (orange) of the soil as function of volumetric soil water content for a loamy soil with porosity $\theta_{\text{sat}} = 0.472\ m^3/m^3$ (vertical dashed line)

The numerical values used in this model (table 2.1) are obtained using the Peters-Lidard et al. (1998) formulation for a loamy soil (≈ 40% quartz content) with a dry density of 1425 kg/m^3, a porosity of θ_{sat} = 0.472 m^3/m^3 and by neglecting the effect of ice and phase changes on the thermal conductivity. The resulting parametrization of the soil thermal conductivity and volumetric heat capacity as function of soil water content is shown in figure 2.2.

This method for determining the soil heat conductivity, based on Johansen (1977), is an interpolation technique between the dry and the saturated values for the soil heat conductivity. This formulation assumes that the saturated value is not affected by the soil microstructure, and calculates it as a geometric

mean of the thermal conductivites of the soil components (water and soil minerals), and their respective volume fractions in equation 2.9 (Farouki, 1981, p.112-113).

Parameter	Value
$\lambda_{T,\text{dry}}$	0.19 W/m/K
$\lambda_{T,\text{s}}$	3.11 W/m/K
$\lambda_{T,\text{water}}$	0.57 W/m/K
$(\rho C)_{\text{dry}}$	2.19×10^6 J/m^3/K
$(\rho C)_{\text{water}}$	4.20×10^6 J/m^3/K

Table 2.1: Numerical values of soil heat transfer parameters used in the land surface model, adapted from ECMWF (2017) and Peters-Lidard et al. (1998).

2.1.2. Soil water transfer

The soil water mass balance is written:

$$\frac{\partial \theta}{\partial t} = -\frac{1}{\rho_w}\frac{\partial F_{hz'}}{\partial z'} - S \tag{2.10}$$

where ρ_w = 0.998 kg/m^3 is the density of liquid water at room temperature, S is the volumetric root water extraction, expressed in $m^3/m^3/s$ and that depends on the depth in the soil z' (positive downwards). The quantity $F_{hz'}$ is the specific mass flux of water in the soil (kg/m^2/s), defined positive downwards.

For a flow with small Reynolds numbers in a porous medium at saturation, the specific mass flux of water F_h (kg/m^2/s) in the upwards direction z, is proportional to the gradient of the hydraulic head according to Darcy's law (Dingman, 2015, chap. 7):

$$\begin{aligned} F_{hz} &= -\rho_w \gamma_{h_{\text{sat}}} \frac{\partial H}{\partial z} \\ &= -\rho_w \gamma_{h_{\text{sat}}} \frac{\partial (z+\Psi)}{\partial z} \\ &= -\rho_w \gamma_{h_{\text{sat}}} \left(1 + \frac{\partial \Psi}{\partial z}\right) \end{aligned} \tag{2.11}$$

where $\gamma_{h_{\text{sat}}}$ is the saturated hydraulic conductivity (m/s), H is the hydraulic head (m), Ψ is the pore pressure head (m) and z is an arbitrary height above a reference surface (m). The subscript 'h' is used for the terms that are related to soil water flow.

The hydraulic conductivity is defined as the bulk specific flow of liquid through a porous medium under a unit hydraulic gradient. It depends on the average grain diameter, on the grain shapes, on the grain size distributions, packing, but it also depends on the kinematic viscosity of the fluid. For water flow, measurements find that it ranges from 10×10^{-12} m/s for fine clay to 10×10^{-2} m/s for gravel (see Wösten et al. (2001) for measurements in the Netherlands).

The hydraulic head H is the sum of the gravitational head, written as the elevation above an arbitrary height, and the pore pressure head Ψ, defined as the water pressure in the soil, relative to the atmospheric pressure $p - p_0$ (Pa) and divided by it's weight density (Pa/m):

$$\Psi \equiv \frac{p - p_0}{\rho_w g} \quad (m) \tag{2.12}$$

Hence, the gradient of the hydraulic head is the gradient of potential energy that induces the bulk soil water flow (Dingman, 2015, chap.7). Below the groundwater table, the soil is saturated with water and the pore pressure is positive. However, in the soil layers between the surface and the groundwater table, also known as *Vadose* zone, the soil is unsaturated with water and the pore pressure is allowed to become negative due to capillary action.

The specific mass flux of water in the upwards z direction F_{hz} (kg/m^2/s), the specific water discharge q_{hz} (m/s) and the volume rate of water flow Q_{hz} (m^3/s) in the z direction are all three related according to :

$$\begin{aligned} F_{hz} &\equiv \rho_w q_{hz} \\ &\equiv \frac{\rho_w}{A} Q_{hz} \end{aligned} \tag{2.13}$$

where A is the unit area normal to the flow direction (in this case, the unit horizontal area).

In the previous equations, the hydraulic flux is defined upwards. If we define $z' = -z$ as the downward direction, the hydraulic (downwards) flux becomes:

$$F_{hz'} = \rho_w \gamma_{h_{\text{sat}}} \left(1 - \frac{\partial \Psi}{\partial z'}\right) \tag{2.14}$$

where $F_{hz'}$ is positive downwards.

For an unsaturated soil, the pore pressure head Ψ becomes negative (suction) due to capillarity. Together with the hydraulic conductivity, it is written as a function of soil water content:

$$F_{hz'} = \rho_w \gamma_h(\theta) \left(1 - \frac{\partial \Psi(\theta)}{\partial z'}\right) \tag{2.15}$$

where $\gamma_h(\theta)$ is the unsaturated soil hydraulic conductivity. The above equation can be rewritten as function of soil moisture only by introducing the soil hydraulic diffusivity and differential soil moisture capacity:

$$\begin{aligned} F_{hz'} &= \rho_w \gamma_h(\theta) \left(1 - \frac{\partial \Psi(\theta)}{\partial \theta}\frac{\partial \theta}{\partial z'}\right) \\ &= \rho_w \left(\gamma_h(\theta) - \lambda_h(\theta)\frac{\partial \theta}{\partial z'}\right) \end{aligned} \tag{2.16}$$

where λ_h is the soil hydraulic diffusivity (m^2/s) defined as:

$$\lambda_h(\theta) \equiv \frac{\gamma_h(\theta)}{C(\theta)} \quad (\text{m}^2/\text{s}) \tag{2.17}$$

and C is the soil differential soil moisture capacity (m^{-1}) defined as:

$$C(\theta) \equiv \frac{\partial \theta}{\partial \Psi(\theta)} \quad (m^{-1}) \tag{2.18}$$

The differential soil moisture capacity represents the ability of a soil to exchange water under a unit change of the pore pressure. It is therefore similar to the definition of volumetric heat capacity (energy required for a unit change in temperature). For instance a soil with high differential soil moisture capacity tends to exchange more water under the same change in pore pressure. Additionally, the hydraulic diffusivity represents ability of a soil to diffuse pore pressure disturbances.

Using the expression for the hydraulic flux $F_{hz'}$ (equation 2.16) in the soil water balance (equation 2.10) gives the 1D Richards equation for water diffusion in unsaturated soils, that is numerically solved in the LSM:

$$\frac{\partial \theta}{\partial t} = -\frac{\partial}{\partial z}\left(\gamma_h(\theta) - \lambda_h(\theta)\frac{\partial \theta}{\partial z}\right) - S \tag{2.19}$$

Solving the Richards equation 2.19 requires the parametrization of the soil hydraulic conductivity and diffusivity as a function of water content.

The Clapp and Hornberger parametrization uses hyperbolic functions proposed by Campbell (1974) and fitted to measurements by Clapp and Hornberger (1978):

$$|\Psi| = \Psi_{\text{sat}}\left(\frac{\theta}{\theta_{\text{sat}}}\right)^{-b} \tag{2.20}$$

$$\gamma_h(\theta) = \gamma_{h_{\text{sat}}}\left(\frac{\theta}{\theta_{\text{sat}}}\right)^{2b+3} \tag{2.21}$$

where Ψ_{sat} is the pressure head at saturation (m) and b is a non-dimensional constant that both depend on the soil type. The hydraulic diffusivity is derived by replacing Ψ and $\gamma_h(\theta)$ in equation 2.17 by their parametrizations in 2.20 and 2.21:

$$\lambda_h(\theta) = \frac{b\gamma_{h_{\text{sat}}}|\Psi_{\text{sat}}|}{\theta_{\text{sat}}}\left(\frac{\theta}{\theta_{\text{sat}}}\right)^{b+2} \tag{2.22}$$

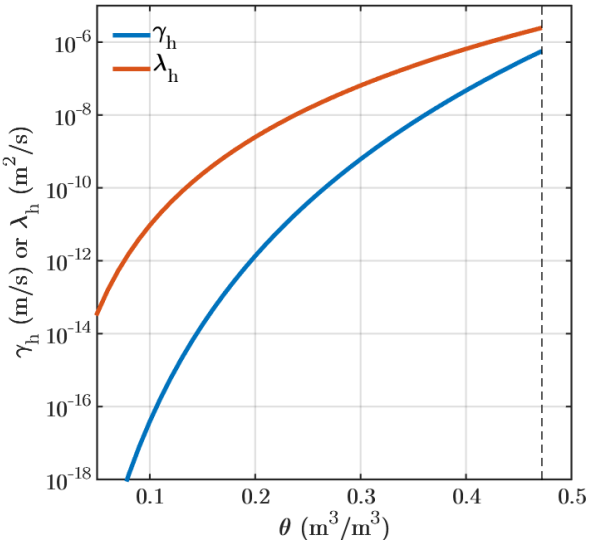

Figure 2.3: Parameterized soil water conductivity (blue) and soil water diffusivity (orange) as function of volumetric soil water content for a medium texture soil with porosity $\theta_{\text{sat}} = 0.472\ m^3/m^3$ (black vertical dashed line), using the Clapp and Hornberger parameterization

It must be noted that equation 2.20 is purely empirical, and equation 2.21 can be derived using 2.20 and Mualem's model (Mualem, 1976) which relies on assumptions about the soil pore size distribution. These hydraulic functions illustrate the fact that the soil pore pressure is a strong non-linear function of relative water content, and that both the hydraulic conductivity and the hydraulic diffusivity increase with increasing water content. They require three parameters : Ψ_{sat}, b and $\gamma_{h_{\text{sat}}}$, which are usually measured or derived from regression analysis on large amount of samples.

In the default version of the LSM, parameters corresponding to a medium soil texture class defined by the United States Department of Agriculture (USDA) are used, which can be found in table 2.2. The resulting hydraulic functions are shown in figure 2.3.

Parameter	Value
Ψ_{sat}	-0.338 m
b	6.04
$\gamma_{h_{\text{sat}}}$	0.57×10^{-6} m/s
θ_{sat}	0.472 m^3/m^3
θ_{fc}	0.323 m^3/m^3
θ_{wp}	0.171 m^3/m^3

Table 2.2: Numerical values of the soil hydraulic parameters for a medium-texture soil used in the land surface model, adapted from ECMWF (2017)

.

2.1.3. Discretization of the transport equations

In the code, the modelled soil column is divided into $k_{\max}$ horizontal layers of increasing thickness D_k, suggested by Deardorff (1978) as temperature variations caused by the atmospheric forcing are expected to decrease with depth. The maximum soil depth in the model is set to 2.89m. The soil temperatures and volumetric soil water contents are defined at the full levels, and the fluxes are diagnosed at the half levels (see figure 2.4). At each timestep, the conductivities and diffusivities at the half levels are diagnosed using two-layer averaging :

$$\begin{aligned} \lambda^i_{1/2} &= \lambda^i_1 \\ \lambda^i_{k+1/2} &= \frac{\lambda^i_{k+1}+\lambda^i_k}{2}, \quad k = 1,...,k_{\max}-1 \\ \lambda^i_{k_{\max}+1/2} &= \lambda^i_{k_{\max}} \end{aligned} \tag{2.23}$$

where i denotes the time index and k the vertical layer index. The thickness between the half layers is calculated according to:

$$D_{k+1/2} = \frac{D_{k+1}+D_k}{2}, \quad k = 1,...,k_{\max}-1 \tag{2.24}$$

The fluxes of heat and water, respectively, are then diagnosed using first order finite difference in the vertical direction:

$$\begin{aligned} &\text{for} \quad k = 1,...,k_{\max}-1 : \\ F^i_{Tz'_{k+1/2}} &= -\lambda^i_{T_{k+1/2}} \frac{T^i_{k+1}-T^i_k}{D_{k+1/2}} \\ F^i_{hz'_{k+1/2}} &= \rho_w \left(\gamma^i_{h_{k+1/2}} - \lambda^i_{h_{k+1/2}} \frac{\theta^i_{k+1}-\theta^i_k}{D^i_{k+1/2}} \right) \end{aligned} \tag{2.25}$$

Hence, the soil heat equation 2.5 and the Richards equation 2.19 are discretized using first order finite difference in the vertical direction:

$$\frac{T^{i+1}_k - T^i_k}{\Delta t} = -\frac{1}{(\rho C)_{\text{soil}_k}} \frac{F^i_{T_{k+1/2}} - F^i_{T_{k-1/2}}}{D_k} \tag{2.26}$$

$$\frac{\theta^{i+1}_k - \theta^i_k}{\Delta t} = -\frac{1}{\rho_w} \frac{F^i_{h_{k+1/2}} - F^i_{h_{k-1/2}}}{D_k} - S^i_k \tag{2.27}$$

In figure 2.4, the typical TESSEL configuration is shown, using values for the layer thicknesses in table 2.3. This configuration was chosen as an optimal trade-off between numerical cost and seasonal accuracy. Time integration is done using a third-order Runge-Kutta scheme (see Heus et al. (2010) for more details).

It is important to mention that first order finite difference in space has an accuracy of the order $(\Delta x)^2$, while the third-order Runge-Kutta scheme in time has an accuracy of the order $(\Delta t)^4$.

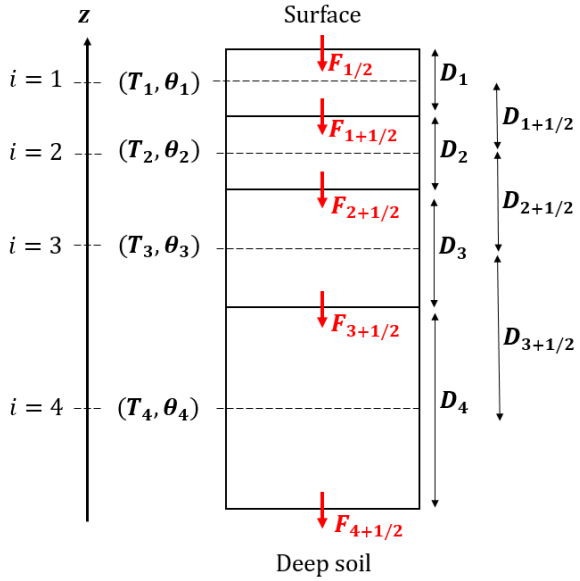

Figure 2.4: Schematic view of the numerical discretization of vertical diffusion equations of the soil.

Parameter	Value
D_1	0.07 m
D_2	0.21 m
D_3	0.72 m
D_4	1.89 m

Table 2.3: Numerical values soil transfer discretization parameters used in the land surface model, adapted from ECMWF (2017).

2.1.4. Boundary conditions and root extraction

The top boundary condition for the soil heat equation is the surface ground heat flux, parameterized as:

$$F_{T_{1/2}} = G_0 = \Lambda_{\text{skin}}(T_s - T_1) \tag{2.28}$$

where G_0 is the surface ground heat flux (W/m^2) and taken positive downwards, Λ_{skin} is the skin layer heat conductivity (W/m^2/K), T_s is the skin temperature and T_1 is the temperature in the first soil layer.

At the bottom of the model, the soil temperature is prescribed, which leads to the following soil heat flux:

$$F_{T_{k_{\max}+1/2}} = \lambda_{T\,k_{\max}} \frac{T_{\text{soil,deep}} - T_{k_{\max}}}{D_{k_{\max}}} \tag{2.29}$$

where $\lambda_{T\,k_{\max}}$ is the soil heat conductivity in the last layer, $T_{k_{\max}}$ is the soil temperature in the deepest model layer, $T_{\text{soil,deep}}$ is the deep soil temperature taken as a constant and $D_{k_{\max}}$ is the depth of the last soil layer.

The top boundary condition for the Richards equation is the evaporation from the bare soil :

$$F_{h_{1/2}} = -\frac{LE_{\text{soil}}}{L_v} \tag{2.30}$$

where LE_{soil} is the bare soil evaporation (W/m^2) and taken positive upwards and $L_v = 2.53 \times 10^6$ J/kg is the latent heat of evaporation.

At the bottom, the 'closed bottom' (no-flux) approach is used:

$$F_{h_{k_{\max}+1/2}} = 0 \tag{2.31}$$

An important sink of soil water content considered in this model is the root extraction, which depends on the root profile and on the amount of vegetation transpiration. The root extraction S_k in the k^{th} soil layer is a fraction of the total vegetation transpiration LE_{veg}:

$$S_k = \theta_{\text{frac}_k} LE_{\text{veg}} \tag{2.32}$$

Different expressions for the root extraction weights θ_{frac_k} can be found. The default version uses the formulation adopted in TESSEL (ECMWF, 2017):

$$\theta_{\text{frac}_k} = \frac{R_k \theta_k}{\sum_{j=1}^{k_{\max}} R_j \theta_j} \tag{2.33}$$

where R_k is the fraction of roots in the k^{th}soil layer. Equation 2.33 states that soil water is extracted from any soil layer as long as roots are present ($R_k > 0$) and as long as there is any soil water present ($\theta_k > 0$).

2.2. Surface energy balance

Balance equations are required to connect the subsurface to the atmosphere. Several assumptions are required for writing simplified balance equations:

- The surface is horizontally homogeneous
- There is no storage of heat and water in solid form (ice, snow)
- There is no local advection in an atmospheric control volume close to the surface

Under these assumptions, a control volume may be compressed to a control surface, and storage terms of heat and water may be ignored (Moene and van Dam, 2014, chap. 1). The Surface Energy Balance (SEB) may then be written as:

$$R_{net} - H - LE - G_0 = 0 \quad (\text{W/m}^2) \tag{2.34}$$

where R_{net} is the net input of radiation at the surface, H is the outgoing (upwards) sensible heat flux, LE is the outgoing (upwards) latent heat flux and G_0 the outgoing (downwards) ground heat flux.

A diagram summarising all the fluxes present in the surface energy balance is shown the left panel of figure 2.1.

The surface energy balance is used to partition the net absorbed radiation by the surface between turbulent fluxes towards the atmosphere and the ground heat flux. The net input of energy at the surface is written:

$$R_{net} = SW_{\downarrow} - SW_{\uparrow} + LW_{\downarrow} - LW_{\uparrow} \tag{2.35}$$

where $SW_{\downarrow}$ and $SW_{\uparrow}$ are the downward and upward shortwave radiation at the surface (wavelengths between 0.15 and 3 μm) and $LW_{\downarrow}$ and $LW_{\uparrow}$ are the downward and upward longwave radiation at the surface (wavelengths between 3 and 100 μm). The upward radiative fluxes depend on the surface albedo α and the the surface emissivity ϵ, according to :

$$SW_{\uparrow} = \alpha SW_{\downarrow} \tag{2.36}$$

$$LW_{\uparrow} = \epsilon \sigma T_s^4 \tag{2.37}$$

where $\sigma = 5.67 \times 10^{-8}$ W/m^2/K^4 is the Stefan-Boltzmann constant.

The ground heat flux is parameterized as:

$$G_0 = \Lambda_{\text{skin}} (T_s - T_1) \tag{2.38}$$

The surface turbulent fluxes of sensible and latent heat (H & LE) depict the ability of the surface to exchange energy with the atmosphere in the form of sensible energy (thermal convection) and latent energy (evaporation of water). Across a wet surface, both fluxes are expressed by the Penman resistance approach:

$$H = \frac{\rho_a C_p}{r_{ah}} (\theta_s - \theta_0) \tag{2.39}$$

$$LE_{\text{liq}} = \frac{\rho_a L_v}{r_{aq}} \left(q_{sat}(T_s) - q_0 \right) \tag{2.40}$$

where ρ_a is the air density at the lowest atmospheric level, $C_p = 1004$ J/kg/K is the specific heat capacity of air at constant pressure, θ_0 is the potential temperature at the lowest atmospheric level, θ_s is the surface potential temperature, q_0 is the water vapour specific humidity at the lowest atmospheric level, q_{sat} is the saturation specific humidity (an approximate expression is written in equation A.17) and r_{ah} and r_{aq} are the aerodynamic resistances to heat and moisture, which depend on wind speeds and atmospheric stability.

The potential temperature is introduced in equation

2.39 in order to take into account the adiabatic cooling of a rising air parcel (decrease in pressure). It is defined as:

$$\theta \equiv \left(\frac{p_0}{p}\right)^{\frac{Rd}{Cp}} T \tag{2.41}$$

where $p_0 = 10^5$ Pa, p is the atmospheric pressure, and $R_d = 287.05$ J/kg/K is the gas constant for dry air.

The skin temperature connects the lower atmospheric temperature to the upper soil temperature through the amount of emitted upwelling longwave radiation, the surface turbulent fluxes and the ground heat flux. If the skin temperature is known, then the whole surface energy is known, and all the fluxes can be diagnosed. However, in the land surface model, the skin temperature is assumed to be unknown and needs to be calculated by solving for the surface energy balance. The full details describing the prognostic equation for the skin temperature in this model can be found in Appendix A.

It is assumed that the aerodynamic resistances to heat and moisture are identical :

$$r_{ah} = r_{aq} \tag{2.42}$$

The expression for surface latent heat flux in equation 2.40, also called Penman evaporation, is only valid over wet surfaces. For land surfaces covered with vegetation, the Penman-Monteith resistance approach is used to calculate the vegetation transpiration:

$$LE_{\text{veg}} = \frac{\rho_a L_v}{r_{aq} + r_{c,\text{veg}}} \left(q_{sat}(T_s) - q_0\right) \tag{2.43}$$

where $r_{c,\text{veg}}$ is an additional surface vegetation canopy resistance that reduces the amount of transpiration from vegetated surfaces compared to wet surfaces (figure 2.5).
The Penman-Monteith transpiration may be rewritten by introducing an effective surface specific humidity:

$$LE_{\text{veg}} = \frac{\rho_a L_v}{r_{aq}} \left(q_s - q_0\right) \tag{2.44}$$

where the effective surface specific humidity q_s is defined as:

$$q_s \equiv \frac{r_{aq}}{r_{aq} + r_{c,\text{veg}}} q_{sat}(T_s) + \frac{r_{c,\text{veg}}}{r_{aq} + r_{c,\text{veg}}} q_0 \tag{2.45}$$

The Penman-Monteith transpiration reduces to the Penman evaporation if there is no surface canopy resistance.

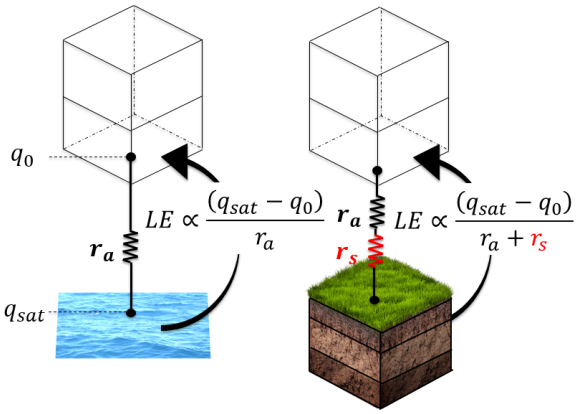

Figure 2.5: Schematic view of the difference between the Penman evaporation (left) and the Penman-Monteith transpiration (right)

In the LSM, a single gridbox is made of vegetation, bare soil and liquid water (interception reservoir). The contributions of the different parts on the total surface evapo-transpiration are separated :

$$LE = LE_{\text{soil}} + LE_{\text{liq}} + LE_{\text{veg}} \tag{2.46}$$

The partitioning of the latent heat flux depends on the fractional vegetation cover and the amount of liquid water in the interception reservoir:

$$\begin{aligned} LE_{\text{soil}} &= (1 - c_{\text{veg}}) \frac{\rho_a L_v}{r_{aq} + r_{s,\text{soil}}} \left(q_{sat}(T_s) - q_0\right) \\ LE_{\text{veg}} &= (1 - c_{\text{liq}}) c_{\text{veg}} \frac{\rho_a L_v}{r_{aq} + r_{c,\text{veg}}} \left(q_{sat}(T_s) - q_0\right) \\ LE_{\text{liq}} &= c_{\text{veg}} c_{\text{liq}} \frac{\rho_a L_v}{r_{aq}} \left(q_{sat}(T_s) - q_0\right) \end{aligned} \tag{2.47}$$

where c_{veg} is the fractional area of vegetation, which is prescribed, and c_{liq} is the relative storage of the liquid water interception reservoir, defined in equation 3.3 and which is a prognostic variable of the model. The quantities $r_{s,\text{soil}}$ and $r_{c,\text{veg}}$ are the bare soil surface resistance (s/m) and the vegetation canopy resistance (s/m), respectively.

Different approaches exist for the parametrization of the canopy resistance $r_{c,\text{veg}}$. The most common one, and used in this model, is the single-leaf approach, which writes the surface resistance as a function of plant density:

$$r_{c,\text{veg}} = \frac{r_{s,\text{veg}}}{LAI} \tag{2.48}$$

where $r_{s,\text{veg}}$ is the diagnosed single leaf stomatal resistance (in s/m) and LAI is the prescribed vegetation leaf area index (in m^2/m^2). The LAI is defined as the one-sided surface area of leaves per surface of ground. The stomatal resistance of a single leaf is then parameterized as function of key meteorolog-

ical variables using the Jarvis-Steward parametrization (Jarvis, 1976):

$$r_{s,\mathrm{veg}} = r_{s,\mathrm{veg}_{\min}} f_1(SW_\downarrow) f_{2,\mathrm{veg}}(\theta) f_3(q_0) f_4(T_0) \quad (2.49)$$

where f_1, $f_{2,\mathrm{veg}}$, f_3 and f_4 are vegetation stress functions and T_0 is the temperature at the lowest atmospheric level. In optimal conditions, the vegetation resistance has a minimum surface resistance $r_{s_{\min}}$. This means that the vegetation evapo-transpiration is always smaller than the Penman evaporation on top of a wet surface.

The bare soil surface resistance only depends on the soil water content:

$$r_{s,\mathrm{soil}} = r_{s,\mathrm{soil}_{\min}} f_{2,\mathrm{soil}}(\theta) \quad (2.50)$$

where $r_{s,\mathrm{soil}_{\min}}$ is the minimum (optimal) bare soil surface resistance and $f_{2,\mathrm{soil}}$ the bare soil water stress function.

The vegetation stress function f_1 for the available photo-synthetically active radiation is a function of downward shortwave radiation:

$$\frac{1}{f_1} = \min\left[1, \frac{bSW_\downarrow + c}{a(bSW_\downarrow + 1)}\right] \quad (2.51)$$

where $a = 0.81$, $b = 0.004 W^{-1} m^2$ and $c = 0.05$. The stress function f_1 is close to 1 for high values of $SW_\downarrow$ but increases to 16 for very small downward radiations (figure 2.6). This translates the effect of reduced vegetation photosynthesis for small amounts of incoming solar solar radiation.

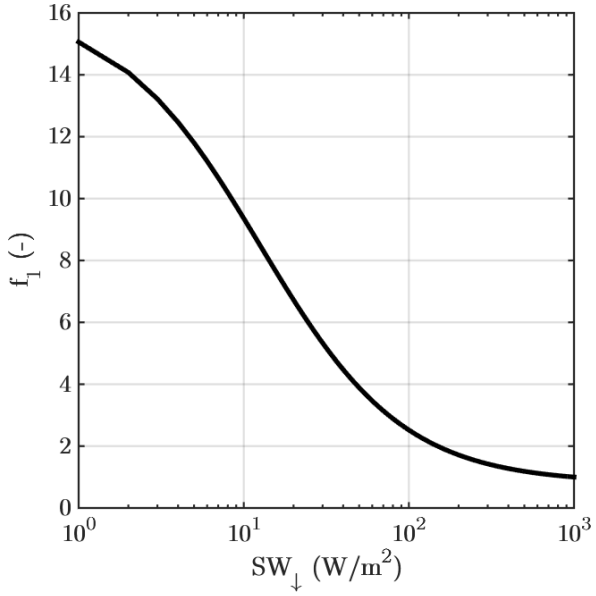

Figure 2.6: Vegetation stress function for downwelling shortwave radiation at the surface used in the land surface model

The introduction of a soil field capacity and a permanent wilting point is necessary to account for the inability of vegetation to extract water in case of soil water stress.
The wilting point is defined as the water content in the soil when plant transpiration ceases. In this model the following definition is used for the permanent wilting point:

$$\theta_{\mathrm{wp}} \equiv \theta(|\Psi| = 150m) \quad (2.52)$$

And the field capacity is defined as the soil water content at which gravity drainage ceases and when water content can only be reduced by evapo-transpiration:

$$\theta_{\mathrm{fc}} \equiv \theta(|\Psi| = 1m) \quad (2.53)$$

These two parameters are derived from the closed-form parametrization of the soil pore pressure (equation 2.20). Numerical values for the USDA medium-texture soil are shown in table 2.2.

Following the TESSEL scheme (ECMWF, 2017), the layer-averaged vegetation water stress function is a weighted average of each layer soil water content:

$$f_{2,\mathrm{veg}} = \frac{\theta_{\mathrm{fc}} - \theta_{\mathrm{wp}}}{\overline{\theta} - \theta_{\mathrm{wp}}} \quad (2.54)$$

where the root-fraction averaged soil water content $\overline{\theta}$ is written as:

$$\overline{\theta} = \sum_{k=1}^{k_{\max}} R_k \max\left[\theta_{\mathrm{wp}}, \theta_k\right] \quad (2.55)$$

The soil water stress function f_2 is equal to 1 when all the soil layers are at field capacity, but increases if the water content in any soil layers where roots are present decreases to the permanent wilting point (figure 2.7). This models the inability of plants to extract water from soils with high water pore suction.

The bare soil water stress function only depends on the water content in the first soil layer:

$$f_{2,\mathrm{soil}} = \frac{\theta_{\mathrm{fc}} - \theta_{\mathrm{wp}}}{\theta_1 - \theta_{\mathrm{wp}}} \quad (2.56)$$

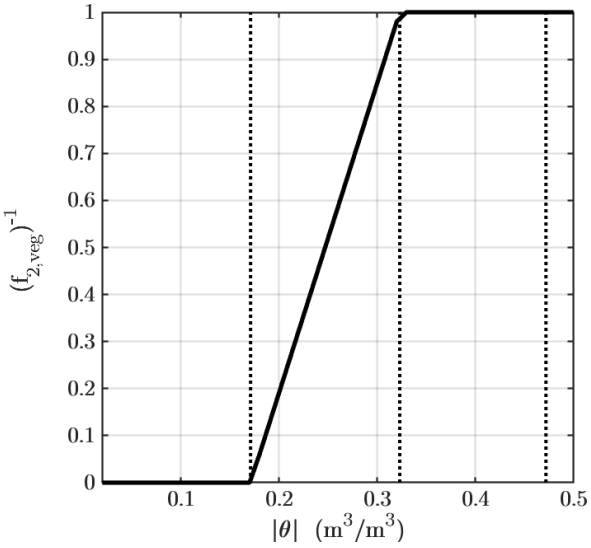

Figure 2.7: Inverse of the vegetation water stress as function of root-averaged soil water content using the ECMWF (2017) formulation for a USDA medium-texture soil layer. Vertical lines denote the permanent wilting point, field capacity and porosity, respectively

For high vegetation, evapo-transpiration becomes dependent on atmospheric humidity. This effect is included through the f_3 vegetation stress function:

$$\frac{1}{f_3} = \exp\left(-g_D(e_{sat}(T_0) - e_0)\right) \tag{2.57}$$

where e_{sat} is the atmospheric saturation water vapour pressure (equation A.15), e_0 is the actual atmospheric water vapour pressure and g_D is a vegetation dependent parameter (Pa^{-1}). The stress function f_3 exponentially increases for increasing atmospheric humidity deficit (figure 2.8).

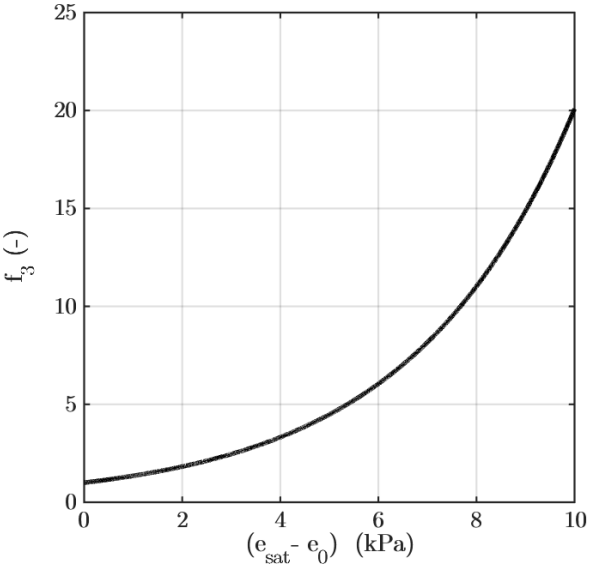

Figure 2.8: Vegetation stress function for the atmospheric water vapour deficit used in the land surface model

Finally, atmospheric temperature might play a role in vegetation activity, e.g. very cold temperatures reducing plant activity. This is present in the model through the vegetation stress function f_4:

$$\frac{1}{f_4} = 1 - 1.6 \times 10^{-3}(T_0 - 298.15)^2 \tag{2.58}$$

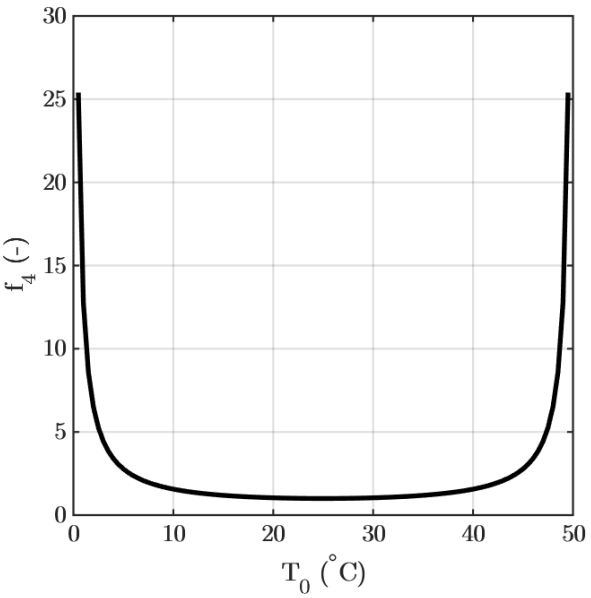

Figure 2.9: Vegetation stress function for the atmospheric temperature used in the land surface model

The atmospheric temperature stress function f_4 is optimal for a temperature of 25°C, and rapidly increases for temperatures below 5°C and higher than 45°C.

The only unknown in the surface energy balance equation is the skin temperature T_s, which is required for the calculation of the surface fluxes. There is no explicit solution to the SEB due to the non-linear dependence of the saturation specific humidity (in equation 2.43) and of the upwelling longwave radiation (in equation 2.37) on the surface temperature.
In this model the non-linear dependencies are linearized in order to allow for the explicit calculation of the skin temperature. The detailed derivation is given in Appendix A.

2.3. Atmospheric boundary layer processes

The solution of the LSM depends directly on processes in the atmospheric boundary layer, such as the strength of turbulence near the surface, and the amount of incoming radiation and precipitation.

2.3.1. Atmospheric surface model

The intensity of turbulence is not resolved by the LES model between the surface and the first model level, but instead it is parameterized by the aerodynamic resistances for momentum and heat r_{am} and r_{aq} in the following equations:

$$\tau = \rho_a \frac{u_0}{r_{am}} \tag{2.59}$$

$$H = \frac{\rho_a C_p}{r_{ah}} (\theta_s - \theta_0) \tag{2.60}$$

where τ is the surface shear stress, u_0 is the wind speed at the lowest atmospheric level, θ_s is the surface potential temperature and θ_0 is the is the potential temperature at the first atmospheric level . The aerodynamic resistances are related to the drag coefficients according to:

$$r_{am} = \frac{1}{C_m \times u_0} \tag{2.61}$$

$$r_{ah} = \frac{1}{C_s \times u_0} \tag{2.62}$$

where C_m is the drag coefficient for momentum and C_s is the drag coefficient for heat and moisture.

In this model, Monin-Obukhov similarity theory (MOST) is used to relate the surface turbulent fluxes to the corresponding vertical gradients of the transported quantities. MOST relies on the key assumptions that mean turbulent quantities are stationary, horizontally homogeneous and are not influenced by processes further away from the surface. Using MOST, dimensionless gradients of a transported quantity are proportional to universal functions. In this model, the surface fluxes are diagnosed in each grid brox separatly. For instance, for the wind speed u and the potential temperature θ, MOST yields :

$$\frac{\partial u}{\partial z} \frac{\kappa z}{u_*} = \phi_m \left(\frac{z}{L} \right) \tag{2.63}$$

$$\frac{\partial \theta}{\partial z} \frac{\kappa z}{\theta_*} = \phi_h \left(\frac{z}{L} \right) \tag{2.64}$$

where $\kappa = 0.40$ is the von-Kármán constant, L is the Obukhov length, defined as the ratio between buoyancy and shear production of turbulent kinetic energy (TKE), and ϕ_m and ϕ_h are the flux-gradient relationships for momentum and heat, respectively, which are specified in the next part. The scaling terms are expressed using the corresponding surface fluxes:

$$u_* = \sqrt{\frac{\tau}{\rho_a}} = \sqrt{|-\overline{u'w'}|} \tag{2.65}$$

$$\theta_* = -\frac{H}{\rho_a C_p u_*} = -\frac{\overline{w'\theta'}}{u_*} \tag{2.66}$$

Integration of equations 2.63 and 2.64 between the surface and the lowest atmospheric model level height yields the following vertical profiles:

$$u_0 = \frac{u_*}{\kappa} \left[\ln\left(\frac{z_1}{z_{0m}} \right) - \Psi_m \left(\frac{z_1}{L} \right) + \Psi_m \left(\frac{z_{0m}}{L} \right) \right], \tag{2.67}$$

$$\theta_0 - \theta_s = \frac{\theta_*}{\kappa} \left[\ln\left(\frac{z_1}{z_{0h}} \right) - \Psi_h \left(\frac{z_1}{L} \right) + \Psi_h \left(\frac{z_{0h}}{L} \right) \right] \tag{2.68}$$

where u_0 and θ_0 are the wind speed and potential temperature in each grid-box at the lowest atmospheric level z_1, respectively. The heights z_{0m} and z_{0h} are the roughness lengths for momentum and heat, and Ψ_m and Ψ_h are the integrated flux-gradient relationships for momentum and heat, respectively. The roughness length for momentum (resp. heat) is interpreted as the height above the surface where the logarithmic profile of the wind speed (resp. potential temperature) extrapolates to zero (resp. to the surface potential temperature).

By rearranging the expressions of the surface fluxes (equations 2.59 and 2.60) together with the definition of the scaling terms (equations 2.65 and 2.66) and the integrated profiles (equations 2.67 and 2.68), the drag coefficients for momentum and heat may be expressed as :

$$\begin{aligned} C_m &= \kappa^2 \left[\ln\left(\frac{z_1}{z_{0m}} \right) - \Psi_M \left(\frac{z_1}{L} \right) + \Psi_M \left(\frac{z_{0m}}{L} \right) \right]^{-2}, \\ C_s &= \kappa^2 \left[\ln\left(\frac{z_1}{z_{0m}} \right) - \Psi_M \left(\frac{z_1}{L} \right) + \Psi_M \left(\frac{z_{0m}}{L} \right) \right]^{-1} \times \\ &\quad \left[\ln\left(\frac{z_1}{z_{0h}} \right) - \Psi_H \left(\frac{z_1}{L} \right) + \Psi_H \left(\frac{z_{0h}}{L} \right) \right]^{-1} \end{aligned} \tag{2.69}$$

The calculation of the drag coefficients requires the knowledge of the integrated flux-gradient relationships Ψ and the Obukhov length L. In this model, the experimental Businger-Dyer flux-gradient relation-

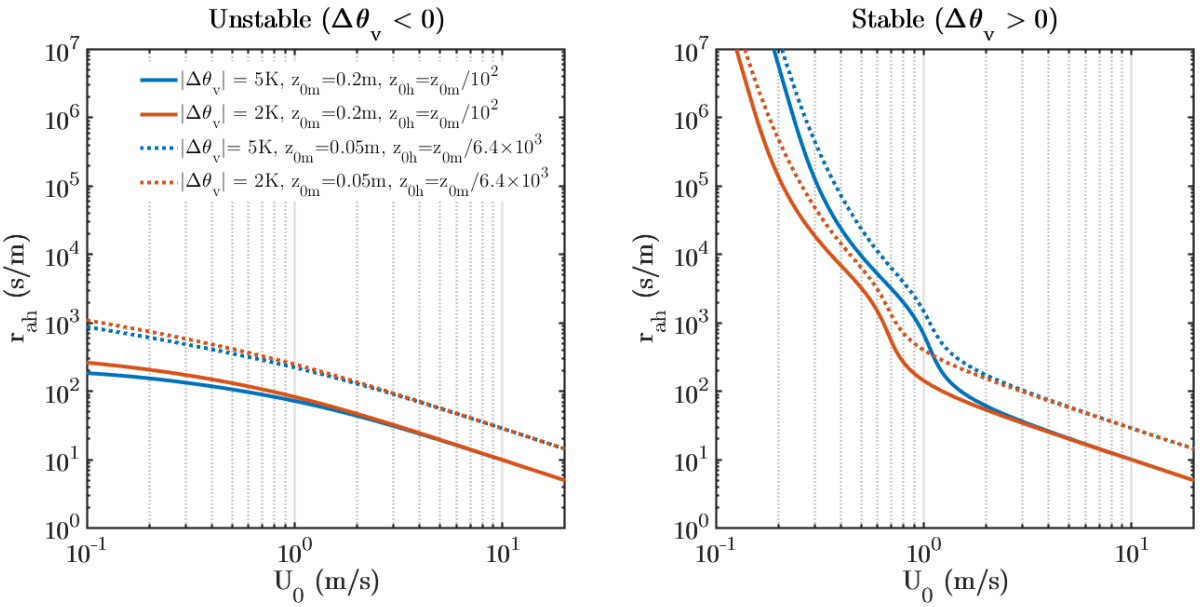

Figure 2.10: Modelled aerodynamic resistance for heat and moisture as function of lowest model level wind speeds in the unstable (left) and stable (right) regimes for two different virtual potential temperature gradients (colours) and two different surface roughness lengths (line styles)

ships are used for the case of unstable stratification:

$$\text{For } \frac{z}{L} \leq 0:$$
$$\Psi_M\left(\frac{z}{L}\right) = 2\ln\left(\frac{1+x}{2}\right) + \ln\left(\frac{1+x^2}{2}\right) - 2\tan^{-1}(x) + \frac{\pi}{2}$$
$$\Psi_H\left(\frac{z}{L}\right) = 2\ln\left(\frac{1+x^2}{2}\right), \tag{2.70}$$

where

$$x = (1 - 16z/L)^{1/4}$$

For the case of stable stratification, the experimental flux-gradient relationships from Beljaars and Holtslag (1991) are used:

$$\text{For } \frac{z}{L} > 0:$$
$$-\Psi_M\left(\frac{z}{L}\right) = a\frac{z}{L} + b\left(\frac{z}{L} - \frac{c}{d}\right)\exp\left(-d\frac{z}{L}\right) + \frac{bc}{d}$$
$$-\Psi_H\left(\frac{z}{L}\right) = \left(1 + \frac{2}{3}\frac{az}{L}\right)^{3/2} + b\left(\frac{z}{L} - \frac{c}{d}\right)\exp\left(-d\frac{z}{L}\right) + \frac{bc}{d} - 1 \tag{2.71}$$

where $a = 1, b = 0.667, c = 5$ and $d = 0.35$.

One single Obukhov length is determined for the whole horizontal model domain by using two different expressions for the horizontal slab averaged bulk Richardson number. The bulk Richardson number is defined as:

$$Ri_b = \frac{g}{\overline{\theta_0}}\frac{z_1\left(\overline{\theta_{v0}} - \overline{\theta_{v_s}}\right)}{\overline{u_0}^2} \tag{2.72}$$

where $\overline{\theta_{v0}}$ and $\overline{\theta_{v_s}}$ are the horizontal slab mean virtual potential temperatures at the lowest model level and at the surface respectively. The quantity $\overline{u_0}$ denotes the horizontal slab mean wind speed at the lowest model level. The virtual potential temperature is defined as:

$$\theta_v \equiv \theta_l\left(1 + (\frac{R_v}{R_d} - 1)q_t\right) \tag{2.73}$$

where $R_d = 287.05$ J/kg/K is the gas constant for dry air an $R_v = 461.5$ J/kg/K is the gas constant for water vapour.

Using MOST, the bulk Richardson number can also be expressed using the integrated flux-gradient relationships and the Obukhov length:

$$Ri_b = \frac{z_1}{L}\frac{\left[\ln\left(\frac{z_1}{z_{0h}}\right) - \Psi_H\left(\frac{z_1}{L}\right) + \Psi_H\left(\frac{z_{0h}}{L}\right)\right]}{\left[\ln\left(\frac{z_1}{z_{0m}}\right) - \Psi_M\left(\frac{z_1}{L}\right) + \Psi_M\left(\frac{z_{0m}}{L}\right)\right]^2} \tag{2.74}$$

A Newton-Raphson iterative method is used to minimise the difference between equations 2.72 and 2.74, which provides a best estimate for the Obukhov length L.

Then the aerodynamic resistance for momentum and heat in each grid-box can be calculated using expressions for the drag coefficients in equation 2.69 and the definitions in expressions 2.61 and 2.62. The

resulting aerodynamic resistance as function of wind speeds is shown in figure 2.10. The aerodynamic resistance ranges between 10^7 s/m for very weak wind speeds in the stable regime to less than 10 s/m for high wind speeds in the unstable regime.

It can thus be concluded that the magnitude of the surface fluxes increases for increased wind speeds, which aims to model a increase in vertical turbulent mixing with an increasing intensity of turbulence. The amount of stratification increases (resp. decreases) the surface fluxes for an unstable (resp. stable) stratification, which aims to model the strengthening (resp. weakening) of turbulent mixing in an unstably (resp. stably) stratified fluid due to buoyancy. Using the parametrization in this model, the effect of stratification is only visible for wind speeds smaller than 2 m/s.

2.3.2. Atmospheric large-eddy simulation

For the fully coupled 3D simulations (chapter 6), the land surface model is coupled to the atmospheric large-eddy simulation model DALES (Heus et al., 2010), which consists of several main parts:

- The dynamical core, that numerically solves the filtered equations of fluid motion using the Boussinesq approximation. This enables the explicit treatment of turbulence up to a certain filter length scale that depends on the model resolution.
- The Subfilter-scale model, which uses a prognostic equation for the subfilter-scale turbulent kinetic energy and a one-and-a-half order closure technique to diagnose the subgrid buoyancy flux, wind shear, turbulent transport and viscous dissipation.
- The Rapid Radiative Transfer Model for General Circulation Models (RRTMG) that is used to estimate radiation absorption by gases, and the radiative transfer through liquid clouds.
- A bulk two-moment microphysics scheme based on Seifert and Beheng (2001) that is used for the calculation of the microphysical processes (e.g droplet autoconversion, sedimentation, collection,...). The cloud droplet concentration number N_c is a prescribed parameter, and a gamma distribution and a Marshall and Palmer distribution are assumed for the cloud droplets and rain droplets probability density functions, respectively. Prognostic equations for droplet number and droplet mass are used to estimate the whole droplet distribution, hence all the relevant microphysical processes.

The Reynolds-averaged budget equation for a conserved variable ϕ is written as:

$$\frac{\partial \overline{\phi}}{\partial t} = -\overline{u_h}\frac{\partial \overline{\phi}}{\partial x_h} - \overline{w}\frac{\partial \overline{\phi}}{\partial z} - \frac{\partial \overline{w'\phi'}}{\partial z} - \overline{\frac{\partial S_\phi}{\partial z}} \tag{2.75}$$

In DALES, $\phi \in \{\theta_l, q_t\}$. Equation 2.75 separates the tendency of a conserved variable in the contributions of large scale horizontal advection, large-scale vertical subsidence, vertical divergence of the turbulent fluxes and the additional source/sink terms. In the case of $\phi = \theta_l$ and a clear boundary layer, the source term $\overline{S_\phi}$ only contains the temperature tendency due to both net longwave and net shortwave radiation, written F_{rad}. The subscript $'h'$ indicates the two horizontal dimensions and w denotes the vertical velocity.

2.4. Summary

The Land Surface Model (LSM) calculates the fluxes of heat and moisture between the surface and the atmosphere using the surface energy balance. The soil temperature and volumetric soil moisture are treated explicitly, and are used to diagnose the ground heat flux and the vegetation water stress. The intensity of turbulence between the surface and the atmosphere is parameterized using the Monin-Obukhov similarity theory (MOST).

The LSM is connected to the turbulence-resolving large-eddy simulation model DALES, which solves for the filtered balance equations of wind speeds, potential temperature and total specific humidity. DALES accounts for additional source/sink terms such as radiation, microphysics and large-scale tendencies.

3 Modifications of the land surface model in DALES

The 'default' land surface model already implemented in DALES4.1 was not yet suited for simulations extending for more then several months, because it did not yet incorporate the precipitation routing from the atmosphere to the surface and into the soil. For this reason, the surface water balance was implemented. The surface water balance allows the LSM to capture the interception of precipitation by the plant leaves, which then either infiltrate into the soil, or is evacuated horizontally by surface runoff (figure 2.1 (b)).

3.1. Surface water balance

The surface water runoff equation is written as:

$$Y = T - \mathrm{I} \quad (\mathrm{kg/m^2/s}) \tag{3.1}$$

where Y is the surface runoff (surface water leaving the model), T the throughfall precipitation (total precipitation minus vegetation interception) and I is the infiltration of precipitation in the upper soil layer.

At the surface, precipitation is first intercepted by the vegetation liquid water reservoir (the vegetation leaves), then the remaining non intercepted precipitation, called throughfall, either infiltrates in the first soil layer or permanently escapes the model by surface runoff (equation 3.1).

The size of the infiltration reservoir depends on the Leaf Area Index:

$$W_{l\max} = W_{\max} LAI \quad (\mathrm{m}) \tag{3.2}$$

where $W_{\max} = 10^{-4} m$ is the maximum thickness of liquid water on a single leaf.
The relative storage of the liquid water reservoir is written:

$$c_{\mathrm{liq}} = \frac{W_l}{W_{l\max}} \tag{3.3}$$

Precipitation is always immediately routed to the interception reservoir, but the amount of interception can't exceed the liquid water reservoir capacity:

$$P_I = \frac{\rho_w}{\Delta t} \min\left[(W_{l\max} - W_l), P\frac{\Delta t}{\rho_w}\right] \quad (\mathrm{kg/m^2/s}) \tag{3.4}$$

where P_I is the intercepted precipitation, W_l is the storage of water in the interception reservoir (m), and P is the precipitation mass flux at the surface (positive downwards, in $\mathrm{kg/m^2/s}$)

The new liquid water storage is then computed:

$$W_l^{t+1} = W_l^t + P_I \frac{\Delta t}{\rho_w} - LE_{\mathrm{liq}} \frac{\Delta t}{\rho_w L_v} \quad (m) \tag{3.5}$$

The throughfall flux T is defined as the remaining precipitation after interception:

$$T = P - P_I \quad (\mathrm{kg/m^2/s}) \tag{3.6}$$

Throughfall is then partitioned between infiltration and runoff depending on the maximum possible infiltration:

$$\begin{aligned} \mathrm{I} &= \min\left[\mathrm{I}_{\max}, T\right] \quad (\mathrm{kg/m^2/s}) \\ Y &= T - \mathrm{I} \quad (\mathrm{kg/m^2/s}) \end{aligned} \tag{3.7}$$

where the maximum infiltration rate is parameterized as a function of upper soil water content and upper soil hydraulic properties:

$$\mathrm{I}_{\max} = \rho_w \left[\lambda_{h,1} \frac{\theta_{sat} - \theta_1}{0.5 D_1} + \gamma_{h,1}\right] \quad (\mathrm{kg/m^2/s}) \tag{3.8}$$

3.2. Boundary conditions for soil water transfer

The top boundary condition for the Richards equation, defined for the default version in equation 2.30, was modified to include the infiltration of precipitation :

$$F_{h_{1/2}} = \mathrm{I} - \frac{LE_{\mathrm{soil}}}{L_v} \tag{3.9}$$

where I is the infiltration of water ($\mathrm{kg/m^2/s}$) (equation 3.7) and taken positive downwards.

The lower boundary condition for water transport was changed from the 'no-flux condition' (equation 2.31) to 'free drainage'. The no-flux lower boundary condition is not adapted, as the modelled soils are then allowed to fill above porosity (not shown). This is an non realistic model artefact caused by the fact

that soil hydraulic fluxes occur under uniform soil moisture profiles ($\partial\theta/\partial z = 0$ in equation 2.16), which would cause the soil water to be transported to the deepest soil layer, even when it is already saturated. In reality, the water table would then rise, and the pore pressure Ψ would become positive.

The free drainage boundary condition assumes that there is no vertical gradient of soil water content:

$$\left(\frac{\partial\theta}{\partial z'}\right)_{k_{\max}+1/2} = 0 \tag{3.10}$$

This means that Darcy's law for the unsaturated soil water flux at the domain bottom (equation 2.16) becomes:

$$\begin{aligned} F_{h_{k_{\max}+1/2}} &= \rho_w \left(\gamma_{h_{k_{\max}}}(\theta) - \lambda_{h_{k_{\max}}}(\theta)\frac{\partial\theta}{\partial z'}\right) \\ &= \rho_w \gamma_{h_{k_{\max}}}(\theta) \end{aligned} \tag{3.11}$$

This lower boundary condition is most suited for simulations where the water table is far from the lower soil boundary. However, this is not the case at CESAR, where both KNMI and WUR measurements indicate a groundwater table at a depth of maximum 2m during dry summer months. For more shallow groundwater tables, a predefined soil pore pressure Ψ as lower boundary condition (Dirichlet type boundary condition) would be more realistic. The latter can however not be implemented in the current version of the model, as the soil pore pressure Ψ is not a prognostic variable.

A necessary improvement of the model for realistically modelling soil water flow and storage at CESAR would be to solve for the Richards equation for saturated-unsaturated soil water flow, in which the differential soil moisture capacity (defined in equation 2.18) occurs as a numerator and not as a denominator (in equation 2.19). This is needed because the differential soil moisture capacity $C(\theta)$ is equal to zero when the soil becomes saturated, which causes the soil water diffusivity to reach infinity (equation 2.17). This approach is adopted in most soil water transfer models, such as the Soil-Water-Atmosphere-Plant (SWAP) model (van Dam, 2000). Another possibility would be to couple a more complex soil-water transfer model with DALES.

3.3. Root water extraction and water stress

The initial formulation of the root water extraction, already described in chapter 2 (equation 2.33) was taken from TESSEL (ECMWF, 2017) and is repeated here for convenience:

$$S_k = \frac{R_k\theta_k}{\sum_{j=1}^{k_{\max}} R_j\theta_j} LE_{\text{veg}} \tag{3.12}$$

and the vegetation stress function for soil water was written as:

$$f_{2,\text{veg}} = \frac{\theta_{\text{fc}} - \theta_{\text{wp}}}{\overline{\theta} - \theta_{\text{wp}}} \tag{3.13}$$

where the root-fraction averaged soil water content $\overline{\theta}$ was written as:

$$\overline{\theta} = \sum_{k=1}^{k_{\max}} R_k \max\left[\theta_{\text{wp}}, \theta_k\right] \tag{3.14}$$

R_k denotes the normalised vegetation root fraction in the k^{th} layer, LE_{veg} is the total vegetation transpiration and θ_{wp} and θ_{fc} represent the soil moisture at permanent wilting point and field capacity respectively.

In the old formulation, roots were allowed to extract water from the k^{th} layer, provided that they are present (R_k>0) and provided that soil water is present (θ_k>0). It did, however, not acknowledge the capacity of the plants to extract water from the deeper soil layers only if the upper soil layers are very dry. In fact this formulation caused root water extraction from all the soil layers simultaneously. This caused too much water extraction from the shallow dry soil layers, while in reality, plants only extract water from deeper layers.

In the adapted land surface model, the root extraction is taken from the SURFEX model (Le Moigne et al., 2009) and is written as:

$$S_k = \frac{\xi_k\Theta_{n,k}}{\sum_{j=1}^{k_{\max}} \xi_j\Theta_{n,j}} LE_{\text{veg}} \tag{3.15}$$

and the vegetation stress function for soil water content is defined as:

$$\frac{1}{f_{2,\text{veg}}} = \sum_{k=1}^{k_{\max}} \xi_k\Theta_{n,k} \tag{3.16}$$

where the transpiration weights ξ_i are a function root profile and layer thickness:

$$\xi_k = \frac{R_k D_k}{\sum_{j=1}^{k_{\max}} R_j D_j} \tag{3.17}$$

And the normalised soil water factors are written:

$$\Theta_{n,k} = \left(\frac{\theta_k - \theta_{\text{wp}}}{\theta_{\text{fc}} - \theta_{\text{wp}}}\right) \tag{3.18}$$

Equation 3.15 states that soil water is only extracted from a soil layer if roots are present ($\xi_k > 0$) and if

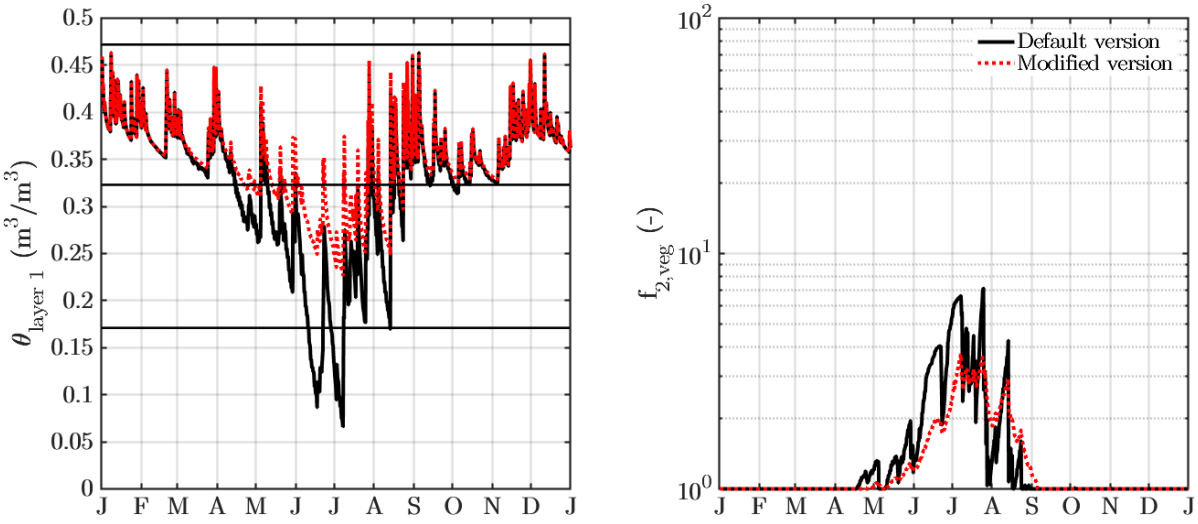

Figure 3.1: (a) Modelled volumetric water content in the first soil layer and (b) modelled vegetation soil water stress function at the CESAR observatory in 2015. The old version uses the TESSEL formulation for root water extraction and water stress, while the new version uses SURFEX formulation. The horizontal lines in (a) represent the porosity, the field capacity and the permanent wilting point, respectively from top to bottom.

the soil water content in this layer is above the permanent wilting point ($\Theta_{n,k} > 0$). Equation 3.16 is bounded by fixed values, which prevent the denominators from reaching zero. The soil water stress function f_2 is equal to 1 when all the soil layers are at field capacity, but increases if the water content in any soil layers where roots are present decreases to the permanent wilting point (figure 3.2). This translates the inability of plants to extract water from soils with high water pore suction.

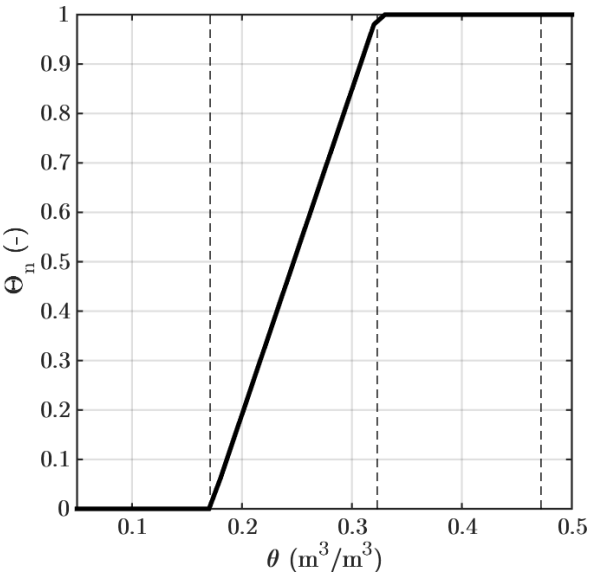

Figure 3.2: Normalised soil water factor as function of the soil water content for a USDA medium-texture soil layer. Vertical lines denote the permanent wilting point, field capacity and porosity, respectively

The bare soil water stress function is not changed and still only depends on the water content in the first soil layer:

$$\frac{1}{f_{2,\text{soil}}} = \Theta_{n,1} \tag{3.19}$$

This new formulation takes into account the different thickness of each layer and calculates the vegetation stress for each layer separately before calculating the total water stress function. The resulting modelled water content at the CESAR observatory in 2015 using the two approaches is shown in figure 3.1. The new version of the model provides a more physically sound soil water content evolution, as the soil water content remains above the permanent wilting point (left panel). This effect, combined with the new formulation of the vegetation soil water stress function, causes less water stress during summer (right), which consequently increases the latent heat flux during these months (not shown).

3.4. Parametrization of the hydraulic functions

The modified Land surface model in DALES now also offers the possibility to use the more complex Van Genuchten parametrization of the soil hydraulic functions. This parametrization uses S-shaped functions proposed by van Genuchten (1980) for the soil water retention curve :

$$|\Psi| = \frac{1}{\alpha_v}\left[\left(\frac{\theta-\theta_r}{\theta_{sat}-\theta_r}\right)^{\frac{n-1}{n}} - 1\right]^{\frac{1}{n}} \tag{3.20}$$

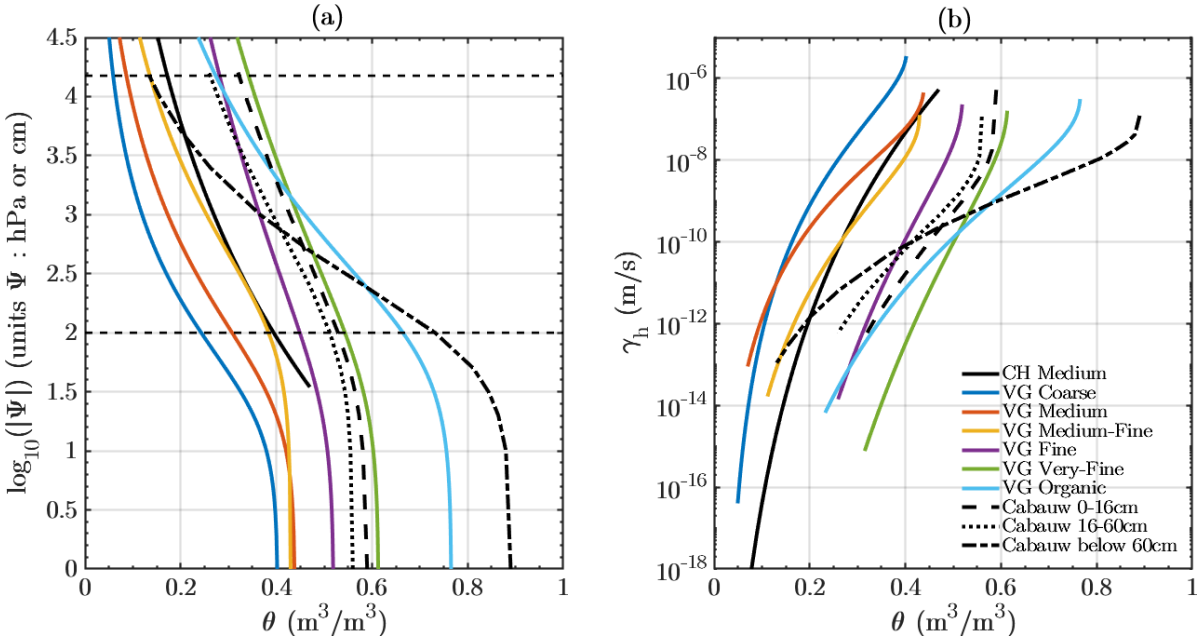

Figure 3.3: Modelled and measured a) Soil water retention curve and b) soil water conductivity. 'CH' stands for the Clapp and Hornberger and 'VG' for the van Genuchten parametrization. Adapted from ECMWF (2017). Measured values are from Wösten et al. (2001) The horizontal lines in a) highlight the soil water contents at permanent wilting point and field capacity.

Soil type (Source)	θ_{sat} (m^3/m^3)	θ_{fc} (m^3/m^3)	θ_{wp} (m^3/m^3)	θ_r (m^3/m^3)	$\gamma_{h_{sat}}$ $(10^{-6}m/s)$	α_v (m^{-1})	l (–)	n (–)
Coarse (H-TESSEL)	0.403	0.244	0.059	0.025	6.94	3.83	1.250	1.38
Medium (H-TESSEL)	0.439	0.347	0.151	0.010	1.16	3.14	-2.342	1.28
Medium-Fine (H-TESSEL)	0.430	0.383	0.133	0.010	0.26	0.83	-0.588	1.25
Fine (H-TESSEL)	0.520	0.448	0.279	0.010	2.87	3.67	-1.977	1.10
Very fine (H-TESSEL)	0.614	0.541	0.335	0.010	1.74	2.65	2.500	1.10
Organic (H-TESSEL)	0.766	0.663	0.267	0.010	0.93	1.30	0.400	1.20
Medium (TESSEL)	0.472	0.323	0.171	-	0.57	-	-	-
B11 (Wösten) *top 16cm*	0.590	0.528	0.320	0.010	0.52	1.95	-5.901	1.11
O12 (Wösten) *16-60cm*	0.560	0.512	0.262	0.010	0.12	0.95	-4.295	1.16
O16 (Wösten) *below 60cm*	0.890	0.732	0.134	0.000	0.12	1.03	-1.411	1.38

Table 3.1: Numerical values for the soil water transfer parameters, adapted from ECMWF (2017) and Wösten et al. (2001)

Then Mualem's model (Mualem (1976)) is used to derive an equation for the soil water conductivity:

$$\gamma_h(\theta) = \gamma_{h_{sat}} \left(\frac{\theta-\theta_r}{\theta_{sat}-\theta_r}\right)^l \times \left(1-\left[1-\left(\frac{\theta-\theta_r}{\theta_{sat}-\theta_r}\right)^{\frac{1}{m}}\right]^m\right)^2 \tag{3.21}$$

The definition in equation 2.17 yields the following expression for the soil hydraulic diffusivity:

$$\lambda_h(\theta) = \frac{(1-m)\gamma_{h_{sat}}}{\alpha_v m(\theta_{sat}-\theta_r)}\left(\frac{\theta-\theta_r}{\theta_{sat}-\theta_r}\right)^{l-\frac{1}{m}} \times \left[\left(1-\left(\frac{\theta-\theta_r}{\theta_{sat}-\theta_r}\right)^{\frac{1}{m}}\right)^{-m} + \left(1-\left(\frac{\theta-\theta_r}{\theta_{sat}-\theta_r}\right)^{\frac{1}{m}}\right)^{m} - 2\right] \tag{3.22}$$

The resulted functions are more complex but much closer to the observations (figure 3.3). The main difference with the Clapp and Hornberger hyperbolic parametrization is that it adds a residual water content and an air entry point in the soil water retention curve. It requires 4 parameters : α_v, l, n and γ_{sat}.

In the Hydrology TESSEL (H-TESSEL) model

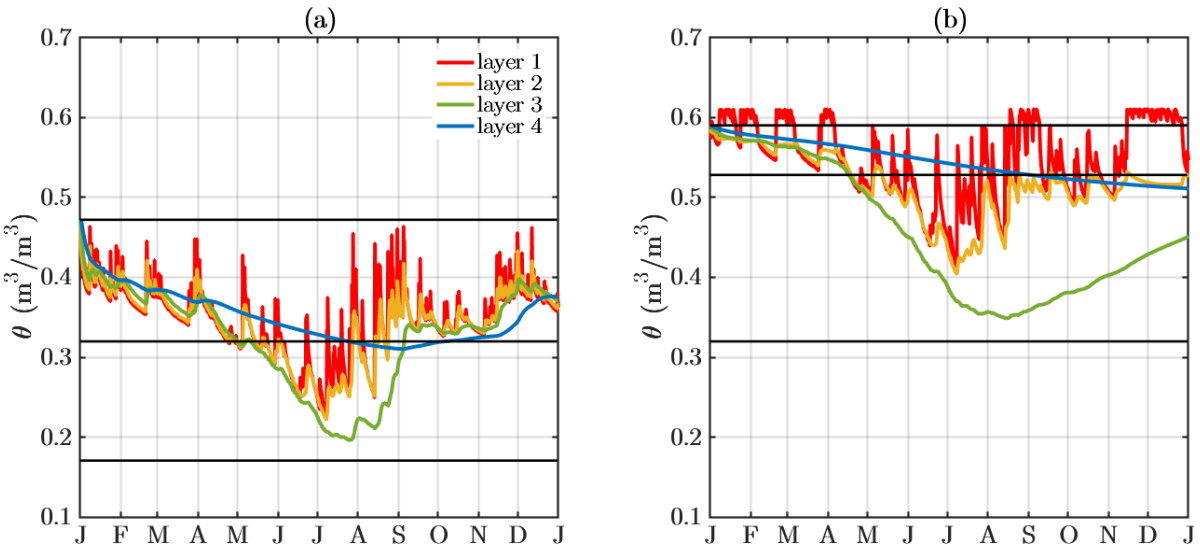

Figure 3.4: Modelled columetric soil water content in Cabauw in 2015 using (a) the Clapp & Hornberger parametrization with a medium class USDA soil texture and using (b) the Van Genuchten parametrization with the B11 soil texture from Wösten et al. (2001). The horizontal lines represent the porosity, the field capacity and the permanent wilting point, respectively from top to bottom.

(ECMWF, 2017), six different soil textures are used, from coarse to organic soils. Based on soil samples at several locations by Jager et al. (1976) at the CESAR observatory, and the soil texture classification in the Netherlands by Wösten et al. (2001), Beljaars and Bosveld (1997) established that the top 18 cm soil at CESAR is close to the upper-soil type B11 (fairly heavy clay), while the soil layer at 16-60 cm is close to the deep-soil type O12 (fairly heavy clay) and the deeper soil layer below 60 cm is close to the deep-soil type O16 (peat). All the corresponding parameters are shown in table 3.1 and in figure 3.3.

The modelled soil water contents using the two different parametrizations are shown in figure 3.4. The volumetric water contents modelled using the Clapp & Hornberger parametrization for a medium USDA soil (panel (a)) are far from the measured water contents (shown in figure 4.13). Likewise, the more complex parametrization using the soil texture measured by Wösten et al. (2001) is neither able to reproduce some common features in the observed water content. For instance, the soil water contents in the shallow layers do not decrease as fast as observed during early April. Furthermore, the first layer always gains water after precipitation events in summer, which is not what is observed nor by the KNMI, neither by SMAP (figure 4.13). Finally, both parametrizations cause a net loss of soil water storage after one year, mainly due to the fact that the deeper levels loose too much water.

The previously mentioned disagreements between the model and the observations are mostly caused by the following imperfections in the land surface model. First, the free drainage boundary condition is undoubtedly causing too much water loss at the soil bottom. Furthermore, the way infiltration is parameterized is still imperfect, as the water content in the first layer tends to go beyond porosity after precipitation events. This artefact is a discretization residual caused by the fact that when the first soil layer reaches porosity, the maximum infiltration rate is not zero but equal to the free drainage rate:

$$I_{\max} = \rho_w \gamma_{h,\mathrm{sat},1} \tag{3.23}$$

according to equation 3.8. Consequently, the water flux between the first and second soil layer is close to the free drainage rate yet not completely, as the hydraulic conductivity at the first half layer is the mean of the hydraulic conductivities of the first and second layer (equation 2.22). Because the second layer is not saturated, the hydraulic conductivity at the half layer is smaller than the saturation hydraulic conductivity:

$$\begin{aligned} F_{hz'_{1+1/2}} &= \rho_w \left(\gamma_{h_{k+1/2}} - \lambda_{h_{k+1/2}} \frac{\theta_{k+1} - \theta_k}{D_{k+1/2}} \right) \\ &\approx \rho_w \gamma_{h_{k+1/2}} \end{aligned} \tag{3.24}$$

and:

$$\gamma_{h_{k+1/2}} < \gamma_{h,\mathrm{sat},1} \tag{3.25}$$

hence,

$$F_{hz'_{1+1/2}} < I_{\max} \tag{3.26}$$

which causes the water content in the first layer to increase beyond porosity (after the water balance in equation 2.19). One possibility to remove this artefact is too smooth the hydraulic conductivity transitions

across layers, or to use more soil layers.

Finally, the fast drying of the soil, seen in figure 4.13, after the month of April is most likely caused by local water management (e.g increase in leaving runoff) that causes the water table to drop fast (not shown), which in turn might also cause important horizontal water flows that are not present in the model. This could be implemented in the model by adding an extra term in the surface water balance (equation 3.1) which contains the prescribed irrigation or drainage flux.

3.5. Summary

In this chapter, some major modifications of the land surface model have been presented, and some necessary improvement for future research are discussed. The most important changes in the model include the implementation of the surface water balance, the parametrization of the root water extraction, the formulation of the vegetation stress function for soil water and the parametrization of the hydraulic functions. It was shown that these modifications allow for a more realistic evolution of the soil water content.

In the next chapters, only the modified land surface model will be used for both the offline and online simulations.

Additional modifications are at this time still necessary for an even more accurate description of the soil water content, such as the implementation of the Richards equation for both saturated and unsaturated flow, the implementation of an heterogeneous soil column in the model and the improvement of the numerical scheme that solves the Richards equation.

4

Observation and estimation of essential land surface variables used in DALES

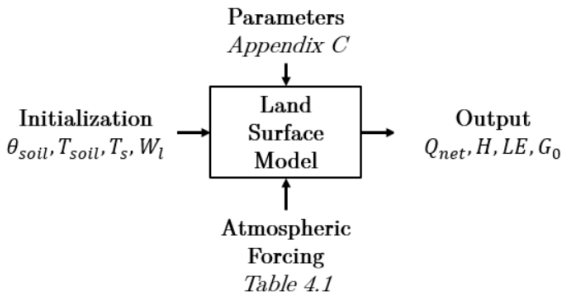

Figure 4.1: Conceptual overview of the land surface model. θ_{soil} stands for the volumetric soil water content.

Running the land surface model at a particular location requires an initialisation of the soil temperatures, the soil volumetric water contents, the surface temperature and the liquid water reservoir storage. Then, atmospheric forcing for each timestep, and numerical values for the soil and vegetation parameters are needed (figure 4.1). DALES typically uses pre-defined values for many land surface parameters, which we will call the STRD parameters. The aim of this chapter is to verify the numerical values for some of these parameters and to find better values, if necessary, at a specific validation site using in-situ observations and satellite remote sensing data. The 'new' parameters will be referred to as REF parameters

In this report, the modelling experiments are performed at the Cabauw Experimental Site for Atmospheric Research (CESAR) (Russchenberg, 2005), using observations from the year of 2015 for the offline land surface model simulations. This location and year were chosen due to the availability of both in-situ and satellite remote sensing observations. Furthermore, the year of 2015 was as interesting year for land surface modelling, as it was a relatively dry year in terms of precipitation, and normal in terms of radiative forcing compared to the 2004-2016 period (figure 4.2).

[1] see `http://www.cesar-database.nl/`

4.1. Description of external datasets

4.1.1. Field observations

The Cabauw Experimental Site for Atmospheric Research (CESAR) is located in Cabauw in the Netherlands (51°58'N 4°56'E), and is maintained by the Royal Dutch Meteorological Institute (KNMI). It provides punctual continuous observations of meteorological variables from the surface up to 200 meters height, at 10-min temporal resolution. The observations relevant for this research include the soil water contents, the soil temperatures, the downward and upward radiation components at the surface and the measurements of the surface turbulent fluxes by eddy-covariance sonic anemometers[1]. The site is well-known for atmospheric research, including land surface model validation (see Beljaars and Bosveld (1997) and Ek and Holtslag (2004)). It is a well-watered short and dense grassland with approximately constant grass height during the year. The soil is mostly made of fairly heavy clay layer mixed with organic material on top of thick layer of peat. The site may be considered to be representative of the land cover within a distance of several kilometres, although some water bodies (ditches and rivers) cause some important horizontal heterogeneity.

Two different datasets for the surface fluxes are available:

- The 10-min averaged eddy-covariance measurements (LB1 data), which are the most of the turbulent exchanges that take place close to the surface. However there are important gaps in this dataset, for instance when there is precipitation or dew deposition. Furthermore, the magnitude of the fluxes during clear and stably-stratified nights with weak winds is often underestimated (de Roode et al., 2010).
- The 10-min residuals of the observed surface

energy balance (LC1 data), which are obtained by subtracting the net absorbed radiation at the surface and the measured ground heat flux, and then by partitioning the remaining energy into sensible heat and latent heat flux using the Bowen ratio measured by the eddy-covariance sonic anemometers. The advantage of this dataset is that is it continuous and that it closes the surface energy balance.

The gap-filled LC1 data will only be used to compare the 10-day averaged surface fluxes over the course of one year. For all the other comparisons, the eddy-covariance LB1 data will be used.

The measurements from the CESAR observatory will be used as atmospheric forcing and as validation data for land surface model simulations in offline mode, described in chapter 5. In chapter 6, these data will be used to initialise and to quantify the quality of the 3D coupled LES experiments.

4.1.2. Satellite remote sensing products

The Copernicus Land Monitoring Service from the European Space Agency (ESA) gathers validated global estimates of useful surface land surface variables.

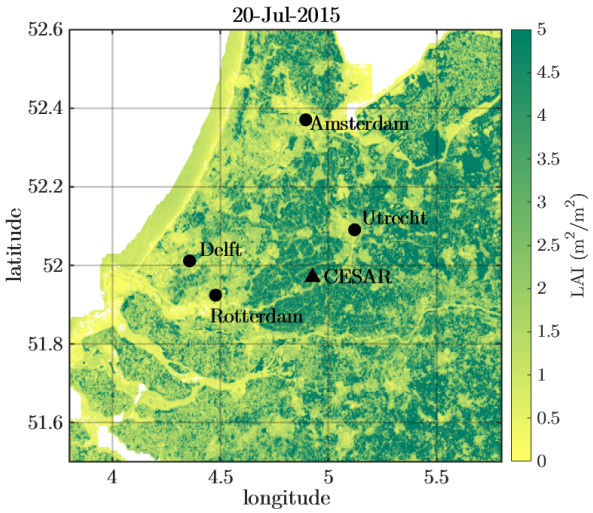

Figure 4.3: Estimated Leaf Area Index (LAI) at 300m spatial resolution using the ESA Copernicus PROBA-V GEOV3 remote sensing products around the CESAR observatory on 20/07/2015.

For instance reflectances in the visible and infrared spectral bands from the ESA PROBA-V mission are used to estimate the vegetation Leaf Area Index (LAI) with a 10-day sampling period at 300m spatial resolution. The data are freely available and accessible online[2]. The PROBA-V GEOV3 LAI satellite retrievals are used in this report, which have already been smoothed temporally and gap-filled. The spatial variability of the estimated LAI near the CESAR site in July 2015 is shown in figure 4.3. In this period, the LAI sampled at the CESAR location equals $\approx 3.5 m^2/m^2$, and seems to be the same with an area of several kilometres. The urban areas with LAI values below 1 m^2/m^2 around the cities of Delft, Utrecht and Amsterdam are clearly visible.

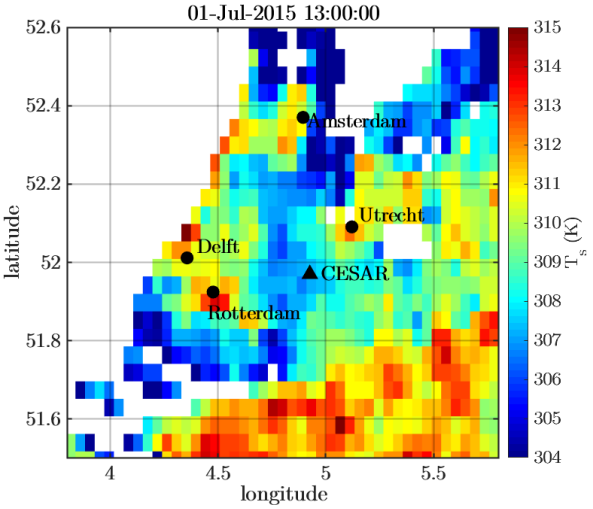

Figure 4.4: Estimated surface temperature T_S at 5km resolution using EUMETSAT Meteosat Second Generation (MSG) remote sensing products around the CESAR observatory on 01/07/2015 at 13:00 UTC.

The Meteosat Second Generation (MSG) geostationary weather satellite operated by the European Organisation for the Exploitation of Meteorological Satellites (EUMETSAT) offers continuous estimates of surface temperature at 5km resolution across Europe using multiple thermal infrared bands[3]. The spatial variability of the surface temperature on 01/07/2015 at 13:00 UTC is shown in figure 4.4. July 1st 2015 was an abnormally warm day in the Netherlands, with maximum recorded air temperatures of 34 $^\circ C$ at de Bilt, near Utrecht. However, MSG measurements show that the CESAR observatory is located in a cooler area, with surface temperatures 5 degrees cooler than the estimated surface temperatures near major cities. This dataset is accurate (overall RMSE of 3K), although the spatial resolution is rather low (5km). Furthermore, clouds cause important gaps in the time series of the estimated surface temperature. The high accuracy is demonstrated in the next section during two different days in figure 4.14.

Finally, the Soil Moisture Active Passive (SMAP) in-

[2] see `http://land.copernicus.eu/global/themes/Vegetation`
[3] see `http://land.copernicus.eu/global/themes/Energy`

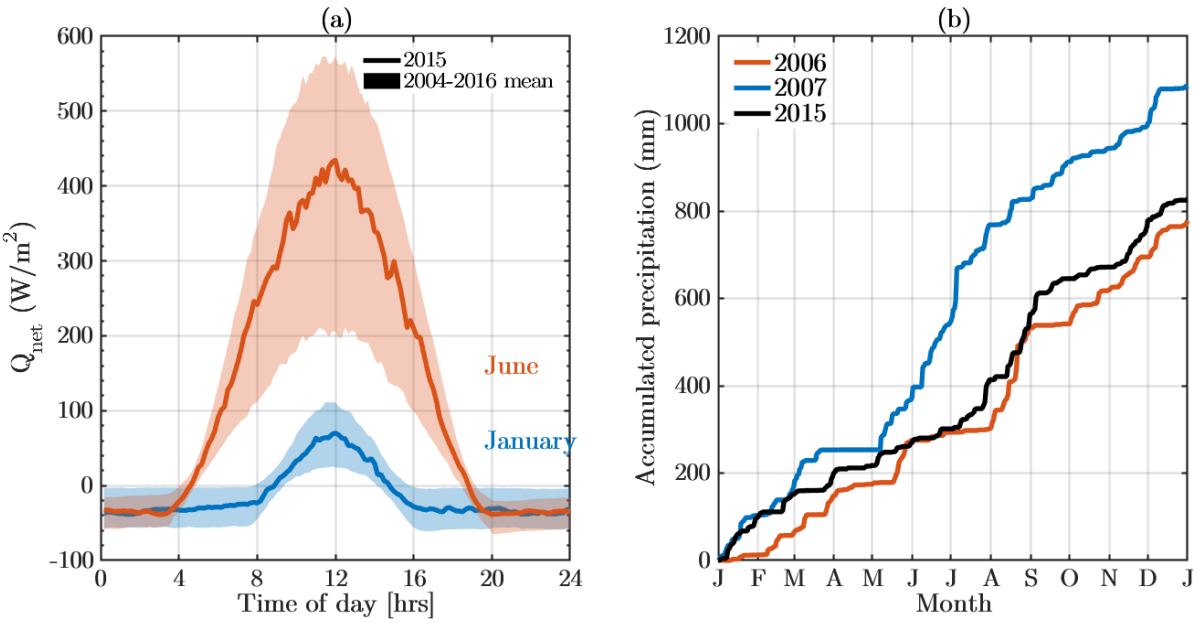

Figure 4.2: (a): Observed monthly mean surface net radiation at the CESAR site in January 2015 (blue) and in June 2015 (orange). The shaded areas represent the monthly mean and standard deviation in the 2004-2016 period (b) Observed accumulated surface precipitation a the CESAR site since January 1st in 2015 (black) compared to observations in 2006 and 2007.

strument from the American National Aeronautics and Space Administration (NASA) was launched in January 2015 and provided the first global retrievals of upper-soil moisture using both passive and active microwave remote sensing in April 2015[4]. In this report, the L3-SM-P-E products are used, which use passive radar observations and are enhanced from 36km to 9km spatial resolution. The spatial variability of the retrieved upper soil moisture on 01/07/2015 at 13:00 UTC is shown in figure 4.5. Although the resolution is rather coarse compared to other datasets (9 km), it demonstrates that the CESAR observatory lies in a region with a strong horizontal upper-soil moisture gradient, with high soil water contents near the coast and lower values further in-land.

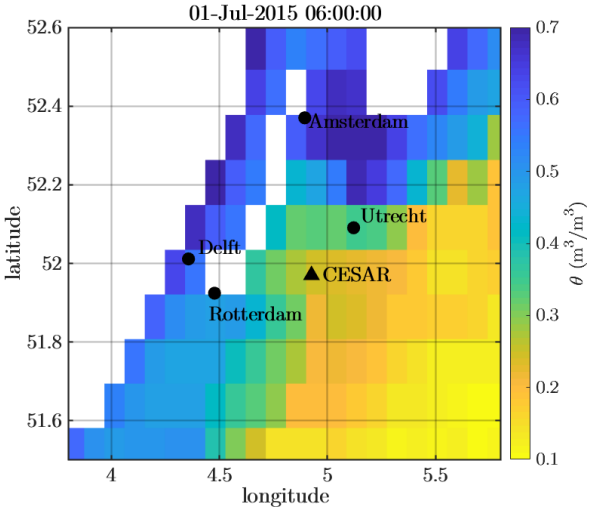

Figure 4.5: Retrieved volumetric upper-soil moisture θ at 9km resolution using NASA SMAP-passive-enhanced (SMAP-L3-SM-P-E) remote sensing products around the CESAR observatory on 01/07/2015 at 06:00 UTC.

[4]see `https://search.earthdata.nasa.gov/`

4.1.3. RACMO & other databases

The output of the land surface model is compared to the output from the Regional Atmospheric Climate Model (RACMO) used by the National Dutch Meteorological Institute (KNMI) used in forecasting mode (van Meijgaard et al., 2008). In forecasting mode, RACMO is initialised every day at 12:00 UTC and is being run for three days with ECMWF forecasts acting as lateral boundary conditions. RACMO provides hourly modelled surface turbulent fluxes, modelled soil water content and temperature and vertical profiles of thermodynamic variables up to a height of $400Pa$ ($> 30km$). The land surface model in RACMO is the TESSEL model from the ECMWF and uses the ECWMF look-up tables for the numerical values of the land surface parameters.

Land surface parameters are often taken from a specific database. In this study, two different databases have been used:

- The Ecoclimap database (Masson et al., 2003) which is specially designed for the ISBA land surface model. This database provides the yearly cycle of most land surface parameters globally, at 1km resolution. This database is mainly made using land cover maps and look-up tables relating the land cover type to the corresponding parameters. The leaf-area index in this database is constrained using 1-km resolution data from the Advanced Very High Resolution Radiometer (AVHRR) on board the National Oceanic and Atmospheric Administration (NOAA) satellites.

- The ECMWF database (ECMWF, 2017), which uses data from the Moderate Resolution Imaging Spectro-Radiometer (MODIS) for the yearly LAI and albedo, and uses look-up tables relating land cover type to the other parameters.

4.2. Input atmospheric forcing

The atmospheric forcing required by the LSM is listed in table 4.1. Each variable is taken at a 10-min sampling time from the CESAR database.

Symbol	Name
θ_{l_0}	Liquid water potential temperature (K)
q_{t_0}	Lower total specific humidity (kg/kg)
$SW_{\downarrow}$	Downward shortwave radiation (W/m^2)
$SW_{\uparrow}$	Upward shortwave radiation (W/m^2)
$LW_{\downarrow}$	Downward longwave radiation (W/m^2)
$LW_{\uparrow}$	Upward longwave radiation (W/m^2)
u_0	First-level zonal wind speed (m/s)
v_0	First-level meridional wind speed (m/s)
p_0	First-level air pressure (Pa)
p_s	Surface air pressure (Pa)
P	Surface precipitation (kg/m^2/s)

Table 4.1: List of atmospheric forcing required by the land surface model.

The seasonal variation of the net radiation absorbed by the surface and the accumulated surface precipitation is shown in figure 4.2. The monthly averaged available radiation at the surface shows an important yearly cycle with a maximum of 420 W/m^2 in June. At the same time, the measured precipitation demonstrates that June 2015 was very dry while July was very wet in terms of accumulated surface precipitation. The end of June 2015 was very similar to the same period in 2006, both being very dry, however some rain events happened in July 2015 while July 2006 remained very dry. In comparison, 2006 was the driest year in the 2004-2016 period, and 2007 the wettest.

4.3. Estimation of some land surface parameters

The temporal evolution of several key parameters required by the LSM can be directly measured at the CESAR observatory, or indirectly estimated from satellite remote sensing instruments.

For instance, PROBA-V retrievals show an important seasonal variation in the Leaf Area Index at the CESAR site, ranging from 1 m^2/m^2 in winter to 3.5 m^2/m^2 during summer. The seasonal variation is also present in the Ecoclimap database, although it does not capture the summer intra-seasonal variability observed by PROBA-V. Furthermore, there is a strong discrepancy during winter, which might be caused by both the lower quality of the LAI satellite products in winter-time due to increased cloud coverage, and by the overestimation of the grassland LAI in the Ecoclimap database for lower values of actual LAI (Masson et al., 2003). On the other hand, Duynkerke (1992) relates the LAI the geometric properties of the grass according to :

$$LAI = h_0 A_f / 2 \tag{4.1}$$

where h_0 is the grass height, taken equal to 5cm, and A_f is the surface area of the leaves per unit volume of air and taken equal to 0.58 cm^2/cm^3 after Brutsaert (1979). This leads to a LAI of 1.5. The LAI has however never been accurately measured at the CESAR site, but Beljaars and Bosveld (1997) argue that the LAI is substantially higher than 1, as the bare soil is never visible. By default, DALES uses a constant value of 2 m^2/m^2 for the LAI of short grass.

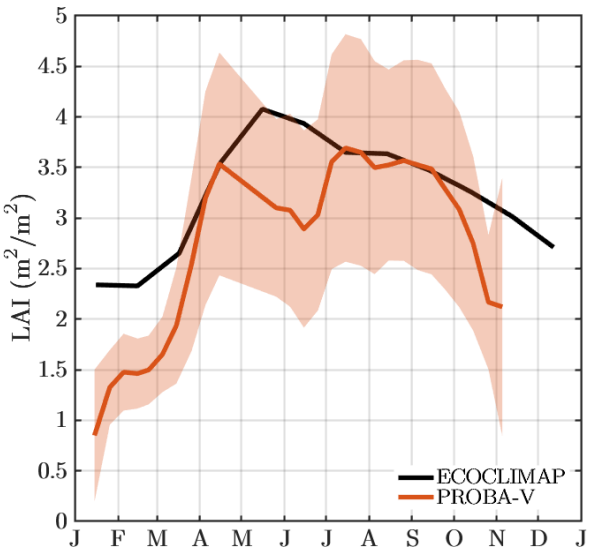

Figure 4.6: Seasonal variation of the Leaf Area Index at the CESAR site in 2015 from ESA PROBA-V satellite products (orange) and from the Ecoclimap database (black). The shaded area represents the spatial standard deviation within a 3km x 3km area centred around the CESAR observatory.

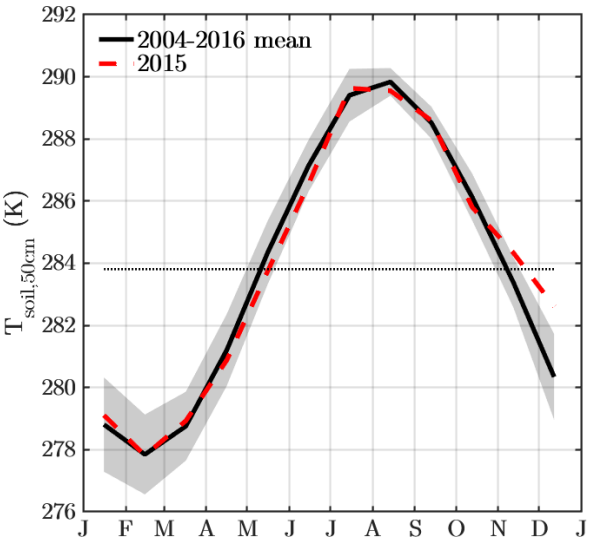

Figure 4.7: Seasonal variation of the monthly mean soil temperature at 50cm depth at the CESAR site in 2015 (red) compared to the 2004-2016 monthly mean. The shaded area represents the standard deviation within the 2004-2016 period. The horizontal line denotes the yearly mean over the 2004-2016 period.

Soil temperature measurements are only available up to 50cm depth, so the deep soil temperature $T_{soil,deep}$ below 2.89m needs to be extrapolated from more shallow soil temperature measurements. The yearly average of the soil temperature at 50cm depth in the 2004-2016 period at CESAR is taken as the prescribed soil temperature below the model soil column, and equals 283.81 K (figure 4.7).

The aerodynamic roughness lengths (introduced in equations 2.67 & 2.68) have been estimated for the CESAR site by Beljaars and Holtslag (1991), who have shown that the roughness length for momentum z_{0m} ranges from 0.01m in winter to 0.15m in summer, depending on the prevailing wind direction. Then, using measurements of the near-surface potential temperature profile, they have shown that the roughness length for heat at the CESAR site is substantially smaller than the roughness length for momentum:

$$z_{0h} = z_{0m}/(6.4 \times 10^3) \tag{4.2}$$

It is argued by Duynkerke (1992) that this ratio mostly depends on the homogeneity of the surrounding vegetation and on the LAI. In the Ecoclimap database, the roughness length for momentum of grasslands in the Ecoclimap database is related to the LAI by: $z_{0m} = 0.13 \times LAI/6\ (m)$. Most interestingly, the z_{0m} for short grass in the Ecoclimap database is very close to the seasonal estimates for the CESAR site from Beljaars and Holtslag (1991). On the other hand, ECMWF look-up tables use a constant value of 0.2m and 0.2×10^{-2}m for the roughness length for momentum and heat of short grass, respectively.

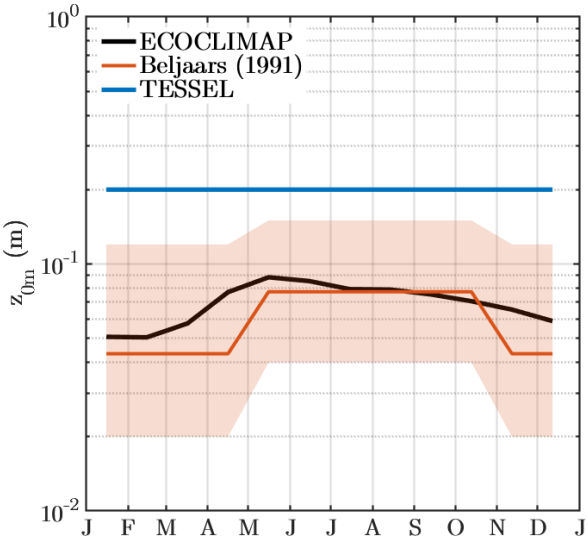

Figure 4.8: Seasonal variation of the average aerodynamic roughness length for momentum at the CESAR site estimated by Beljaars and Holtslag (1991) (orange) and from TESSEL (blue) and ECOCLIMAP (black). The shaded area represents the range of observations, depending on the wind direction.

The ratio of upward to downward shortwave radiation at the surface, or surface albedo, is a function of both vegetation greenness and solar zenith angle.

The estimated daily variation for different months is shown in figure 4.12. This estimate is obtained using $\alpha = SW_{\uparrow}/SW_{\downarrow}$ and by averaging 13 years of data from the CESAR site. The albedo strongly decreases during daytime and reaches a minimum when the sun reaches a minimum solar zenith angle. This is mostly caused by the geometry of the grass leaves, which more efficiently trap incoming radiation when solar rays penetrate deeper into the grass layer, at low solar zenith angles (Moene and van Dam, 2014, chap. 2). However, the albedo does not only depend on the solar zenith angle, as the minimum albedo at minimum zenith angle seems to decrease from May to July, but also across days (figure 4.10). The monthly decrease could be explained by the growth of the grass between May and July. And the variability between clear days in July might be caused by precipitation that affects both the growth and the colour of the grass. It must be noted that the actual (blue-sky) albedo also depends on the fraction of diffuse radiation (Beljaars and Bosveld, 1997), however this effect has not been investigated in this research.

Overall, the albedo at Cabauw ranges from 0.21 during summer at low solar zenith angles to 0.33 during winter at high solar zenith angles, which is consistent with the estimates from Duynkerke (1992). The average albedo over all seasons and solar angles equals 0.27, however special care must be taken in summertime, when a small difference in shortwave albedo may lead to very different net radiation absorbed by the surface.

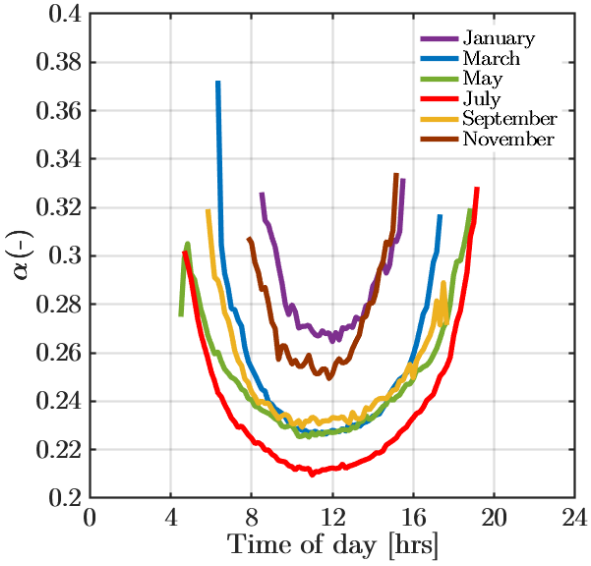

Figure 4.9: Estimated surface shortwave albedo $\alpha = SW_{\uparrow}/SW_{\downarrow}$ as function of time of day at the CESAR site using data in the 2004-2016 period. The curves have been obtained by taking the mean of the estimated α for every 10 minutes during the day, for all days within a particular month. This means that every point is a mean of approximately $31 \times 13 = 403$ observations.

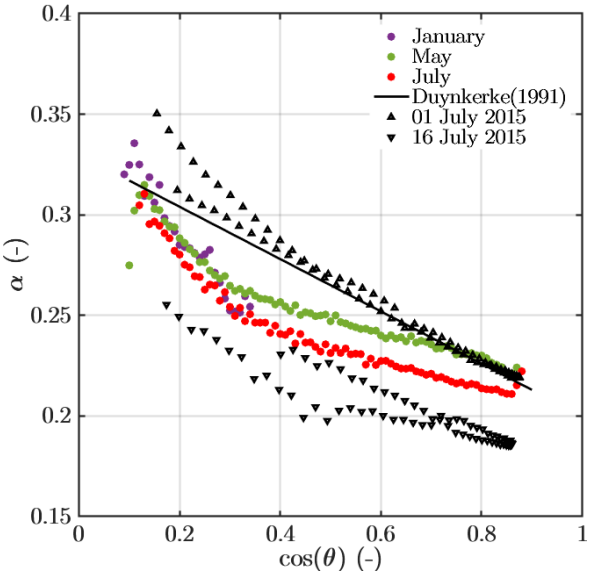

Figure 4.10: Estimated surface shortwave albedo $\alpha = SW_{\uparrow}/SW_{\downarrow}$ as function of the cosine of the solar zenith angle at the CESAR site using data in the 2004-2016 period. The curves have been obtained by taking the mean of the estimated α for all zenith angles within a particular month. The proposed relation by Duynkerke (1992) for the CESAR site is shown by the black line, and the triangles represent the estimates during two clear days in July 2015.

The skin layer thermal conductivity Λ_{skin} is a parameter that expresses the efficiency of heat transfer between the skin layer and the first soil layer. It is usually kept constant in models, using a value that depends on the vegetation type. DALES and the TESSEL model use for instance a value of 10 $W/m^2/K$ for short grass, regardless of the season or the atmospheric conditions. However, it has been shown by Verhoef and Vidale (2012) that Λ_{skin} has a strong seasonal and diurnal variability at the CESAR site, and is a strong non-linear function of atmospheric stability.

The seasonal and daily variation of Λ_{skin} is shown in figure 4.11. Based on the method used by Verhoef and Vidale (2012), Λ_{skin} was estimated using 10-min sampled observations from CESAR and the definition for the ground heat flux in equation 2.28. The ground heat flux is estimated using radiation and flux measurements and closing the SEB (equation 2.34). The skin temperature is estimated using the longwave radiation components at the surface, and taking into account the effect of longwave radiation reflection at the surface:

$$T_s = \left(\frac{LW_{\uparrow} - (1-\epsilon) LW_{\downarrow}}{\epsilon \sigma} \right)^{\frac{1}{4}} \tag{4.3}$$

where a surface emissivity ϵ of 0.98 was assumed for short green grass. It must be noted that the emissivity strongly depends on the radiation geometry, on the wavelength and on the molecular arrangement of the material. The value of 0.98 corresponds to the geometrical- and spectral- integrated measurements

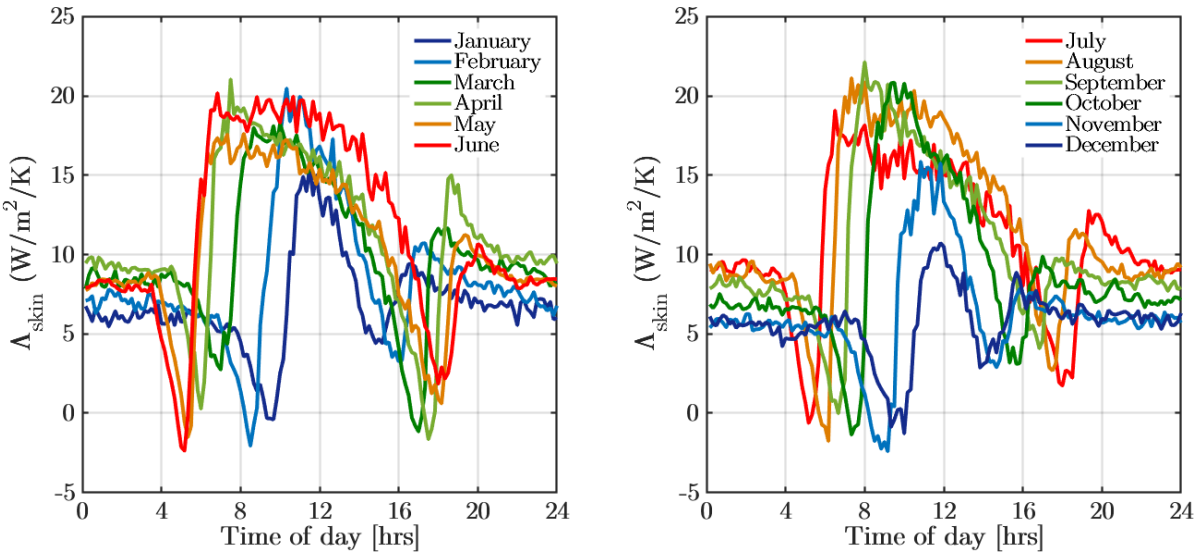

Figure 4.11: Estimated skin heat conductivity as function of the time of day at the CESAR site using data in the 2004-2016 period and $\Lambda_{skin} = G_0/(T_s - T_{soil,1})$. The curves have been obtained by taking the median of the estimated Λ_{skin} for every 10 minutes during the day, for all days within a particular month. This means that every point is a median of approximately $31 \times 13 = 403$ observations.

of the emissivity of green indiangrass leaves by Salisbury and D'Aria (1994) and Salisbury and D'Aria (1992) in the 3-5 μm and 8-14 μm bands, respectively.

Taking the median of the estimated skin conductivity values per month and time of day reveals that Λ_{skin} increases from winter to summer and from nighttime to daytime and can reach 20 $W/m^2/K$ during daytime in summer. Most surprisingly is that the estimated Λ_{skin} can drop below 0 $W/m^2/K$ (countergradient flux) during day/night transitions, regardless of the season. This is not what one might expect from molecular heat diffusion, and is most likely cause by transport processes that are not represented in the LSM, such as in-canopy heat transfer. In Appendix G it is hypothesised that the negative Λ_{skin} is a consequence of taking soil temperature measurements at a certain depth below the actual surface, which is not in direct thermal contact with the radiative skin layer.

The soil texture at the CESAR site has been rather well documented (see Jager et al. (1976) and Beljaars and Bosveld (1997)). It consists of at least three different superimposed horizontal layers: two layers of fairly heavy clay mixed with organic material (top 60cm) on top of a thick layer of peat (below 60cm). These soil types are closest to the "Very-Fine" and "Organic" soil textures used in the ECMWF - HTESSEL model. The medium soil texture used in TESSEL is inadequate for the CESAR site, as it underestimates the amount of water that can be stored in the fine-clay soils at the CESAR site.

The root fraction, defined as the fraction of root mass in a soil layer (introduced in equation 2.33), has not been documented for the CESAR site, but the dominant vegetation species is known: *Lolium perenne* (or Perennial Ryegrass) (Beljaars and Bosveld, 1997). In-situ measurements of the root distribution for this particular grass species by Brown et al. (2010) indicate that the maximum root depth of this grass species barely exceeds 80cm, with 40% of the roots mass located in the 0-8 cm soil layer. On the other hand, ECMWF parametrizations use root distributions estimated by Zeng (2001), which are based on global in-situ data compiled by Jackson et al. (1996) and Canadell et al. (1996). For short grasslands, the maximum rooting depth is set to 1.5m, with 96% of roots mass in the 0-1m soil layer. The root fractions per soil layer then also depend on the discretization of the soil column (table 2.3). The different possible root fractions for the CESAR site using the 4-layer ECMWF discretization are given in table 4.2.

Method	R_1	R_2	R_3	R_4
Zeng (2001)	0.35	0.38	0.23	0.04
Jackson et al. (1996)	0.33	0.47	0.20	0.00
Brown et al. (2010)	0.40	0.30	0.30	0.00

Table 4.2: Estimated root fractions in the 4 soil layers for the CESAR site using the layer thicknesses in ECMWF configuration (table 2.3) and using three different methods.

Finally, the minimum stomatal resistance for vegetation $r_{s,veg_{min}}$ is indirectly estimated per land cover using in-situ measurements of surface fluxes and meteorological variables. Different experiments and field observations lead to different numerical values, which are then tabulated according to land cover in

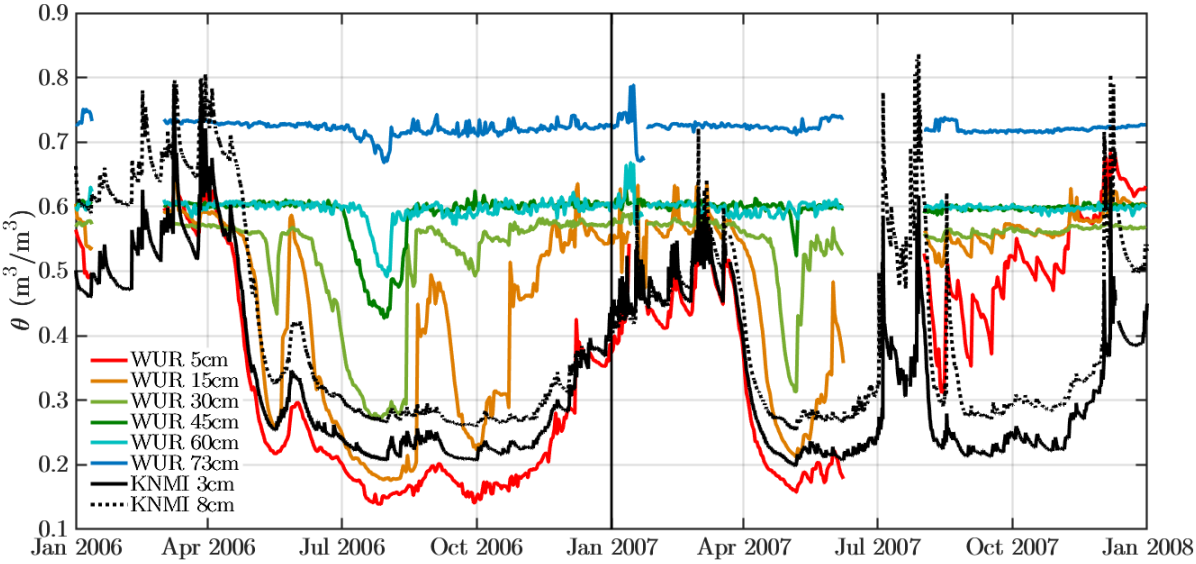

Figure 4.12: Observed volumetric soil water content at the CESAR site in 2006 and 2007 at different depths from both WUR and KNMI measurements. The mean of 4 different WUR sensors is shown.

specific databases. In the ECMWF TESSEL model, $r_{s,\mathrm{veg}_{\mathrm{min}}}$ for the "short grass" class is set to 110 s/m, while in the Ecoclimap database, the value for grasslands is taken equal to 40 s/m.

4.4. Comparison of validation data

The performance of the LSM is evaluated by comparing the output listed in table 4.3 to in-situ measurements from the CESAR observatory or satellite remote sensing estimates.

Symbol	Name
θ	Volumetric soil moisture (m^3/m^3)
T_{soil}	Soil temperature (K)
T_s	Surface temperature (K)
H	Surface sensible heat flux (W/m^2)
LE	Surface latent heat flux (W/m^2)

Table 4.3: List of land surface model validation data.

Measurements of the volumetric water content at CESAR during 2006 and 2007 are shown in figure 4.12. The dataset from Wageningen University (WUR) consists of measurements at four different locations, hence it gives a reasonable estimate of the seasonal soil moisture variability at the CESAR observatory. This dataset unfortunately only ranges between 2003 and 2010, while single location measurements from the KNMI are available continuously.

The different soil moisture measurements demonstrate that the soil at the CESAR site is saturated most of the time below 45cm, with one exception during July 2006 when no precipitation was observed for several consecutive weeks. In the upper soil levels, volumetric water content ranges between 0.55 m^3/m^3 during winter to 0.2 m^3/m^3 during summer. The strong observed vertical variability is mainly caused by the vertical variability of the soil texture and the concentration of organic material.

There are some important differences between the KNMI and the WUR sensors, which could both be caused by different sensor calibration or by the horizontal variability (e.g. distance of the different sensors to the nearest ditch). The upper layers (0-15cm) react the fastest after rainfall events or period of droughts, which will significantly affect the water available for vegetation activity, as a high fraction of roots are present in this layer.

Most remarkably, besides the strong seasonal variation of the volumetric soil water content, is the fact that after a prolonged period without rainfall in July 2006, the first precipitation in August 2006 seems to infiltrate directly into the deeper levels below 45cm, without affecting the more shallow soil layers. This is most likely caused by cracks that may form in the soil during a prolonged period without rainfall, which then act as a fast pathway for the first precipitation. This effect is not incorporated by the diffusive approach in the model, and might cause problems during dry summer months.

In 2015, SMAP satellite remote sensing estimates of upper-soil moisture are available for comparison. These estimates are compared to the actual measurements and to the output from RACMO in figure 4.13. SMAP tends to slightly overestimate the soil water at CESAR, especially during late summer/fall.

It must be noted that the strong typical decrease in upper soil moisture during April is well captured by SMAP estimates. Finally, the volumetric water content predicted by RACMO is not consistent with the actual measurement of volumetric water contents in Cabauw. Passive remote sensing may be an interesting choice for the validation of land surface models, despite the fact that there still are some important discrepancies with the in-situ observations.

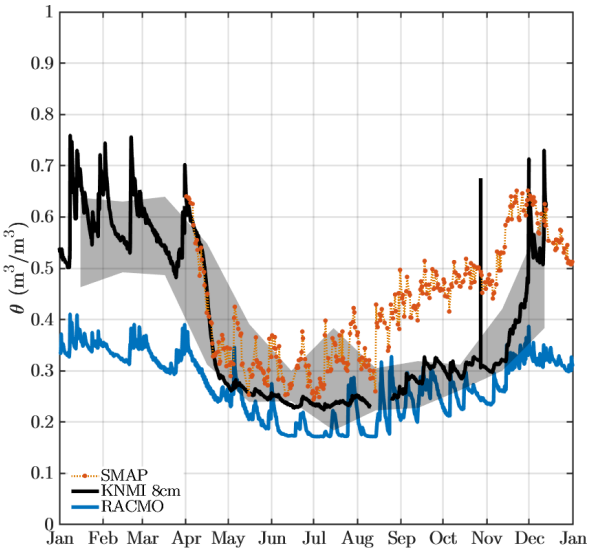

Figure 4.13: Upper-soil volumetric water content in 2015 at the CESAR site using NASA SMAP estimates (orange), KNMI measurements (black) and RACMO output (blue). The shaded area represents the mean and standard deviation of the KNMI measurements in the 2004-2016 period.

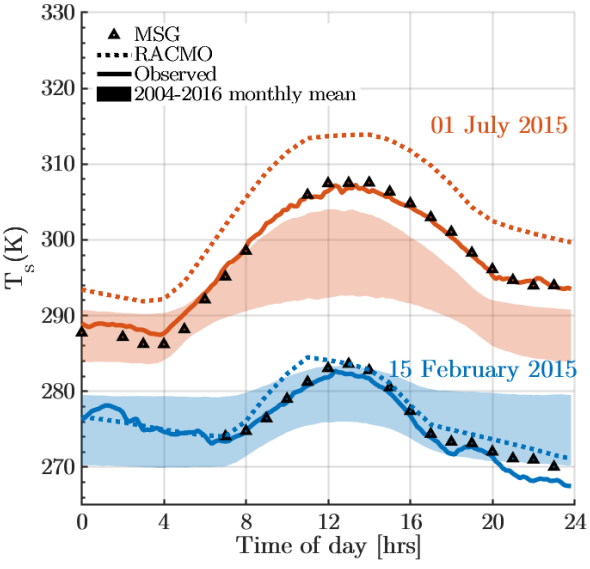

Figure 4.14: Comparison of surface temperature at the CESAR site on two particular days in 2015 between Meteosat (MSG) estimates, regional model RACMO and KNMI observations. The shaded areas denote the observed monthly variation, centred around the middle of the month, in the 2004-2016 period.

Observed and modelled surface temperatures for a winter and a summer day at the CESAR site are shown in figure 4.14. When they are available, Meteosat (MSG) surface temperature estimates agree very well with KNMI measurements. July 1st, 2015 was much warmer than usual, with observed surface temperatures much higher than the 2004-2016 monthly mean in July.

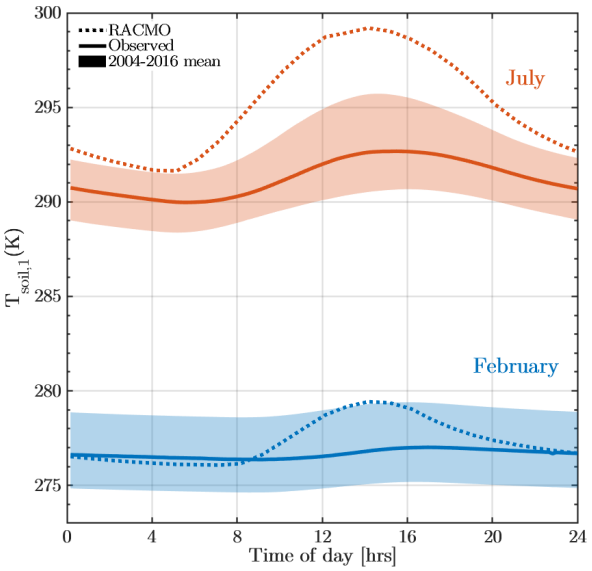

Figure 4.15: Comparison of upper-soil temperature at the CESAR observatory in February and July 2015 between regional model RACMO and KNMI observations. The shaded areas denote the observed monthly means in the 2004-2016 period.

The comparison between observed and modelled soil and surface temperatures indicate that RACMO is both overestimating the soil temperatures in the first layer (figure 4.15) and the surface temperatures (figure 4.14) in July by several degrees. The observed daily variation of the soil temperatures does not exceed 2K, which is much smaller than daily variation the soil temperature predicted by RACMO.

Finally, the surface fluxes are shown in figure 4.16. Both the surface latent heat flux and sensible heat flux show a strong seasonal and daily variability. The monthly average latent heat flux reached 300 W/m^2 at noon in July 2015, which was 75 W/m^2 more than the long-term mean. Interestingly, the sensible heat flux barely exceeded 50 W/m^2 in the same period, which was normal compared to the long-term mean. RACMO is greatly overestimating the sensible heat flux and underestimating the latent heat flux during summer.

It will be argued in chapter 6 that this overestimation of the sensible heat flux partly explains the overestimation of the surface temperature in July (figure 4.15) in RACMO. The offset of the modelled surface fluxes is a strong indication that the land surface is not well parameterized for the CESAR site within RACMO. It predicts abnormal vegetation water stress while in reality, vegetation is still able to extract water from

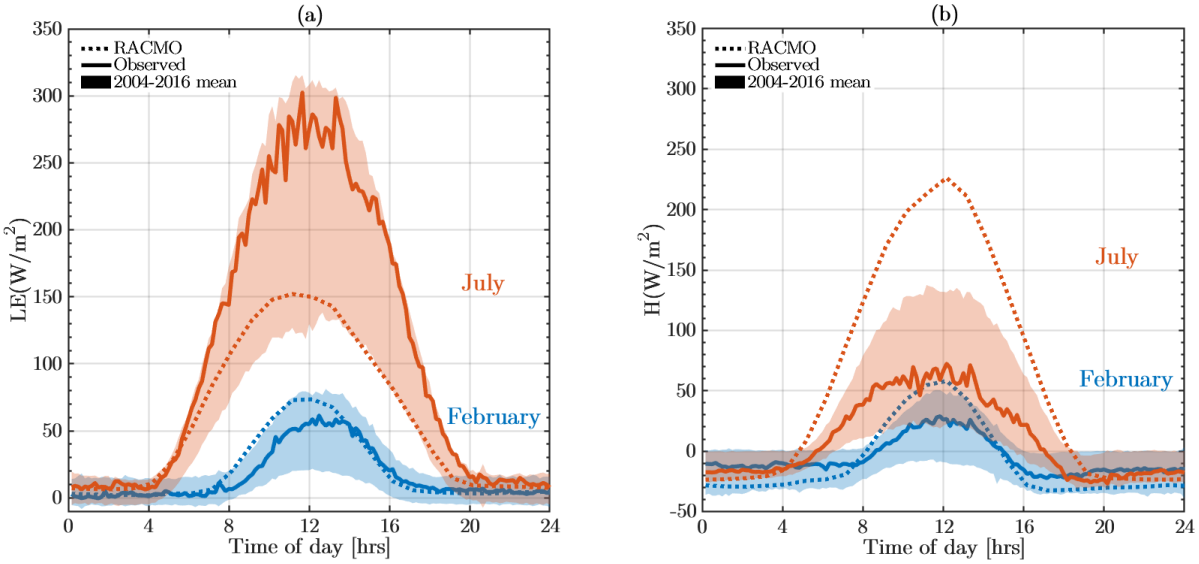

Figure 4.16: Monthly averaged daily variation of the turbulent surface fluxes at the CESAR observatory in 2015 of the (a) latent heat flux and the (b) sensible heat flux. The shaded areas denote the average in the 2004-2016 period, while the dashed lines are the output from regional model RACMO.

the soil and transpire towards the atmosphere during a prolonged warm and dry period at the CESAR site.

4.5. Summary

The analysis of the observations from the CESAR observatory and the estimation of several land surface variables from remote sensing products demonstrate the following key results:

- Satellite remote sensing in the visible- and infra-red spectral bands indicates that the estimated leaf area index greatly increases during summer and that it has a strong spatial variability around the CESAR site (figures 4.3 & 4.6).
- Satellite passive microwave remote sensing indicates that the upper-soil moisture at the CESAR site rapidly decreases during April 2015, and then slowly increases again after summer, which is consistent with the in-situ measurements (figures 4.5, 4.13 & 4.14).
- Geo-stationary satellite infrared remote sensing is able to estimate surface temperatures every hour very accurately under cloud-free conditions (figures 4.4 & 4.14). The spatial and temporal resolution of this data is able to distinguish the cooler area around CESAR and the warmer urban areas of Utrecht, Amsterdam and Rotterdam.
- The use constant roughness lengths at CESAR is not recommended. The estimated roughness length for momentum as obtained from Beljaars and Holtslag (1991) and from the Ecoclimap database at CESAR ranges from 2cm in winter to 15cm in summer, depending on the wind direction (figure 4.8).
- The estimated shortwave albedo at CESAR ranges from 0.21 during summer at low solar zenith angles to 0.33 during winter at low zenith angles (figures 4.9 & 4.10).
- The estimated skin heat conductivity ranges from 5 W/m^2/K during night in winter to 20 W/m^2/K during daytime in summer (figure 4.11).
- The ECMWF 'Fine-soil' texture is closest to the observed upper-soil texture at CESAR (figure 3.3).
- The ECMWF 'short grass' class contains much deeper roots compared to root profile measurements for the predominant grass species observed at the CESAR site (table 4.2).

5 Offline land surface simulations

In this chapter, results from the land surface model (LSM), including the modifications described in chapter 3, are presented. The modified LSM is run in offline mode, which means that it is forced with atmospheric observations from CESAR (listed in table 4.1). The components of the surface energy balance are being calculated for each time step using the equations described in chapter 2. Several reference simulations are performed using a 'good' parameter set derived in Chapter 4, then several important input parameters are varied within a realistic range in order to asses the sensitivity of the model on the input parameters. Model results are compared against the output from the regional model RACMO and against measurements from CESAR described in chapter 4 (listed in table 4.3). Each simulation is initialised on January 1st 2015 at 12:00 UTC and performed until January 1st 2016 at 00:00 UTC.

Similar offline simulations using data from CESAR have been performed before. For instance Beljaars and Holtslag (1991) investigated the effect of several important surface parameters on the accuracy of the modelled surface fluxes, and proposed experimental stability functions for the modelling of the surface transfer coefficients (see chapter 2). Secondly, van den Hurk et al. (2000) have tested a similar land surface model using standard parameters sets taken from ECMWF look-up tables, and show that their model is able to represent the yearly cycle of the 10-day averaged latent heat flux in 1987 with an accuracy of 20 W/m^2. They also found that the strongest deviations occur during summer. Finally, Ek and Holtslag (2004) performed offline simulations over the course of one day using an optimal parameter set for the CESAR site, and found that a very similar land surface model is able to model the daily variation of both turbulent surface fluxes with an accuracy similar to the measurement accuracy (~ 20 W/m^2) during a warm summer day. They also examined the effect of a different initialisation and different parametrizations and suggested several improvements in the land surface model, including a more profound formulation of the root water extraction, and more accurate parametrizations of the ground heat flux and of the soil hydraulic functions.

5.1. Reference simulations

The reference simulation "REF" is the offline simulation that uses the modified land surface model version described in chapters 2 & 3, and that uses the 'optimal' parameter set derived in section 4.3, and summarised in Appendix C.

Both the LAI and the roughness lengths z_{0m} and z_{0h} have a monthly variability; the LAI is taken from the Ecoclimap database and ranges from a minimum of 2.4 m^2/m^2 in January to a maximum of 4 m^2/m^2 in May (figure 4.6). At the same time, the roughness length for momentum z_{0m} is taken equal to 4.3 cm between November and April and taken equal to 7.7cm between May and October, which corresponds to the all-azimuth average of the seasonal roughness length estimated by Beljaars and Holtslag (1991) (figure 4.8). The skin heat conductivity Λ_{skin} is assumed to be constant and is set to 8 W/m^2/K, which corresponds to the estimated average overnight (figure 4.7). The night-time average was chosen as it is expected that the overnight ground heat flux is relatively more important for the overall surface energy balance. Roots are only present in the first three layers, and the Van Genuchten parametrization with the B11 soil texture from Wösten et al. (2001) is chosen for the soil hydraulic functions.

The STRD simulation is the offline simulation that also uses the modified land surface model but uses standard parameters from the ECMWF-TESSEL look-up tables for the 'short grass' vegetation type.

In this simulation the LAI is kept constant at a value of 2 m^2/m^2, and the roughness length for momentum and for heat are constant and equal to 2×10^{-1} and 2×10^{-3} m, respectively. The skin heat conductivity is taken equal to 10 W/m^2/K, the vegetation fraction is equal to 0.85, the deep soil temperature is equal to 283K, the roots are deeper than the roots in the REF simulation, and the Clapp & Hornberger parametrization is used with the medium USDA soil texture classification for the soil hydraulic functions.

For each run, the soil temperature profile is initialised

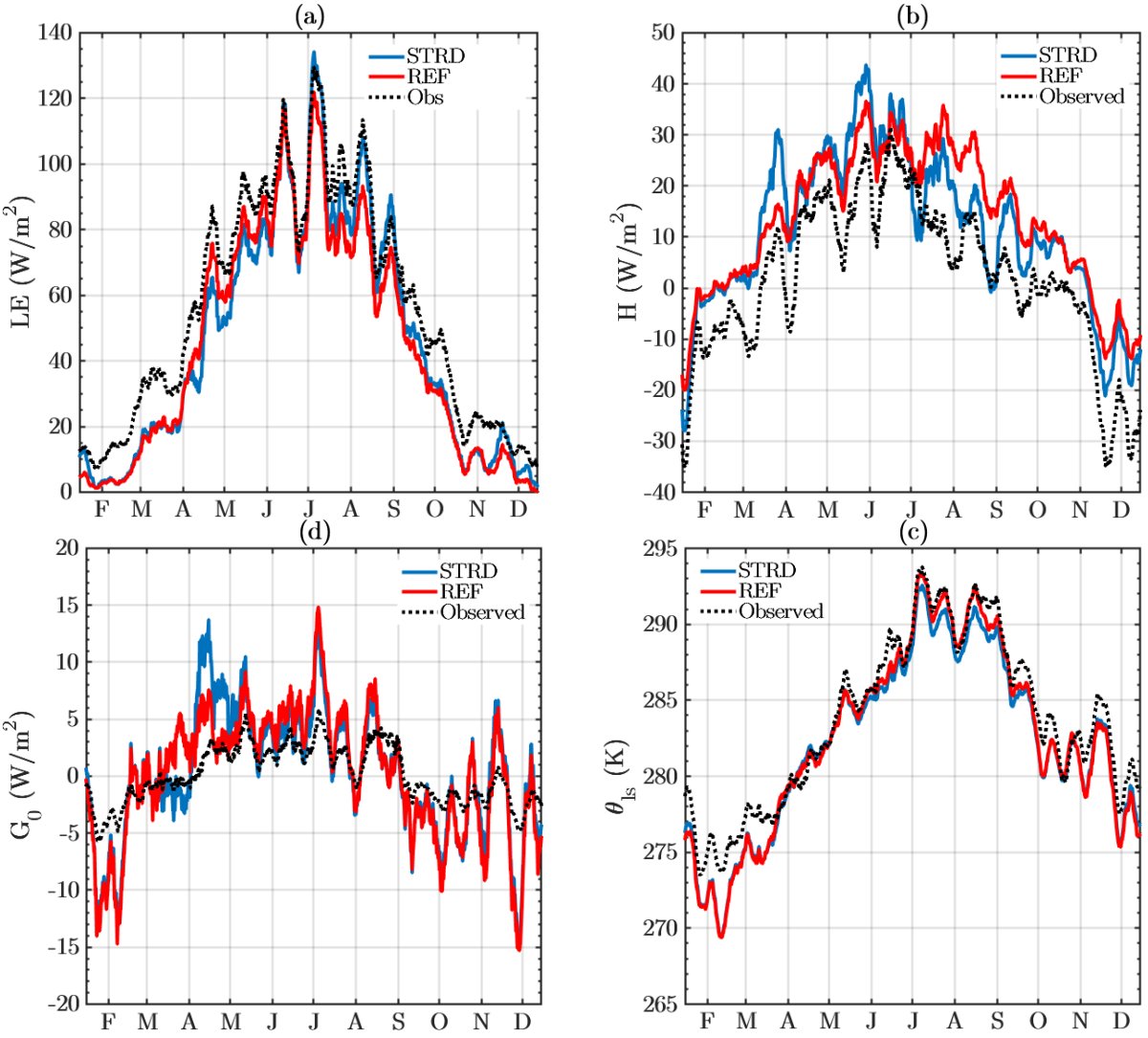

Figure 5.1: 10-day average of the modelled (a) latent heat flux, (b) sensible heat flux, (d) ground heat flux and (c) surface potential temperature during 2015 at the CESAR observatory. The gap-filled LC1 surface flux data are shown by the black lines.

using data down to 50cm in depth, and is linearly extrapolated up to the deepest layer using the constant deep soil temperature. The soil water content is initialised close to porosity over the whole soil column for both simulations.

At the same time, the added-value of the land surface model is tested by running a set of benchmark experiments that do not use a prognostic equation for the skin temperature T_s, but instead use the prescribed surface temperature derived from the observed upward longwave radiation at CESAR. In these simulations the soil transfer and surface energy balance equations are not used. The effect of environmental conditions on the vegetation transpiration is however still taken into account by using a prescribed value for the vegetation canopy resistance $r_{c,\mathrm{veg}}$ and by assuming a vegetation fraction of 100%. These simulations are referred to "RSx", where x is the prescribed value for the canopy resistance (in s/m) (see table 5.1).

Name	Value for $r_{c,\mathrm{veg}}$	Comments
RS0	0 (s/m)	r_s constant, T_s prescribed
RS50	50 (s/m)	r_s constant, T_s prescribed
RS100	100 (s/m)	r_s constant, T_s prescribed
RS150	150 (s/m)	r_s constant, T_s prescribed
STRD	diagnosed	T_s prognostic
REF	diagnosed	T_s prognostic

Table 5.1: Overview of the reference simulations.

The comparisons of the seasonal variations of the modelled surface fluxes and surface potential temperature between the REF and the STRD simulations are shown in figure 5.1. Most interestingly, the REF and STRD simulations give very similar 10-day aver-

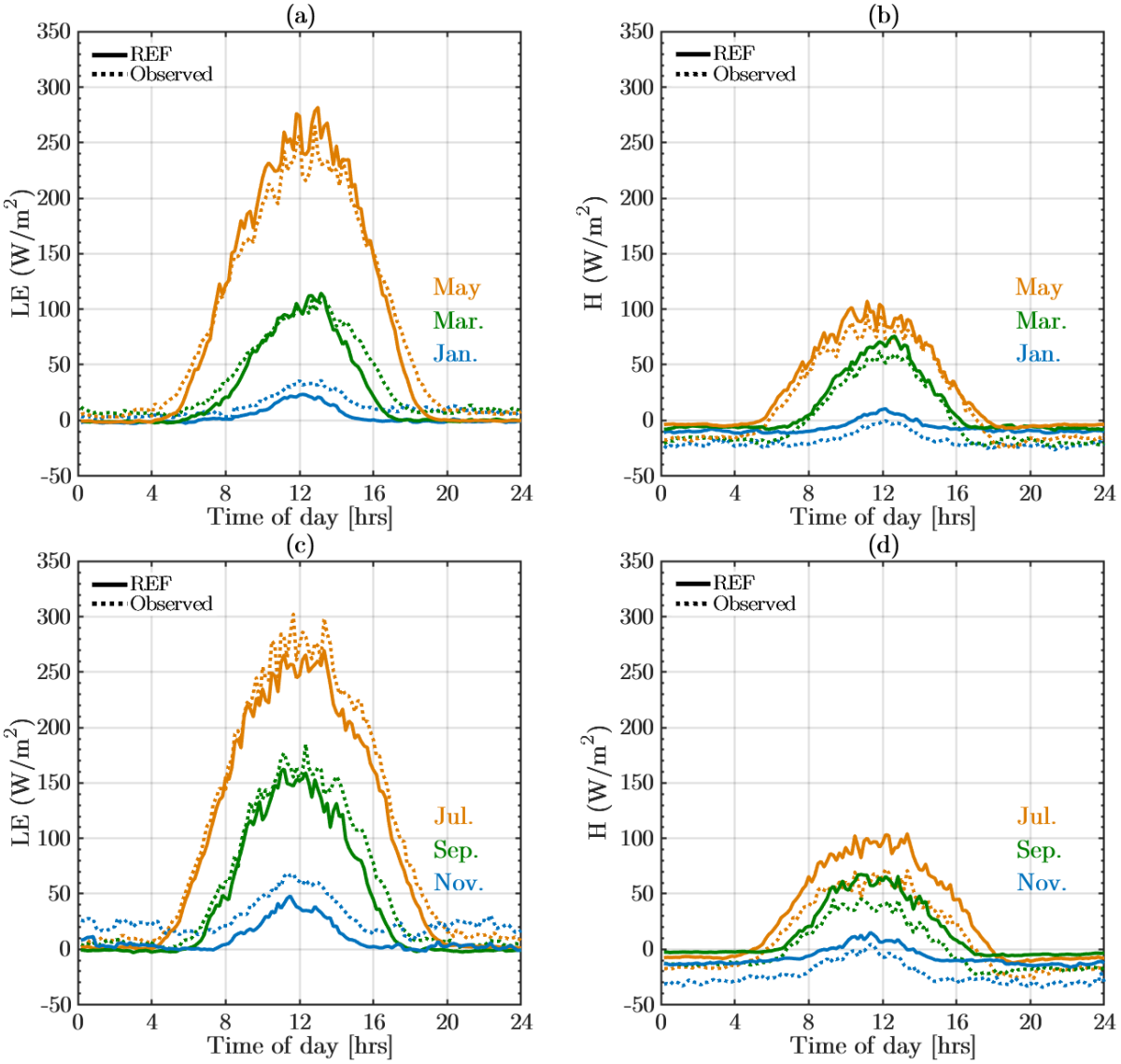

Figure 5.2: Monthly averaged daily variation of the modelled and observed (a) & (c) latent heat flux and (b) & (d) sensible heat flux for January/March/May (top panel) and July/September/November (bottom panel) in 2015 at the CESAR observatory.

age results, although they use rather different parameters. This is a good example of parameter uncertainty as different parameter sets lead to a very similar result. Both simulations underestimate the annual latent heat flux by 10 W/m^2 (RMSE of 12 W/m^2) and overestimate the annual sensible heat flux by 10 W/m^2 (RMSE of 11 W/m^2). Furthermore, the annual ground heat flux is modelled with an accuracy of 0.1 W/m^2, but with a RMSE of 3.5 W/m^2 (not shown). Finally, the skin temperature underestimated by 1K, with a yearly RMSE of 1.5K.

To understand why the two simulations give very similar results is not straightforward. It will be shown in the next sections that the annual variations of the modelled vegetation water stress depends on both the soil texture and on the root profiles. The REF simulation uses more shallow roots and a soil that loses more water than in the STRD simulation. This causes more water stress, hence decreases the latent heat flux in the REF simulation. However, the STRD simulation uses a constant value of the LAI of 2m^2/m^2, and a cooler deep soil temperature, which increases the canopy resistance as well as decrease the shallow soil temperature, respectively. These two effects tend to increase the amount of transpiration in the REF simulation, compared to the STRD simulation. Hence the modelled evaporation is the combination of at least three parameter effects (root water stress, LAI and soil temperature), which actually tend to compensate each other.

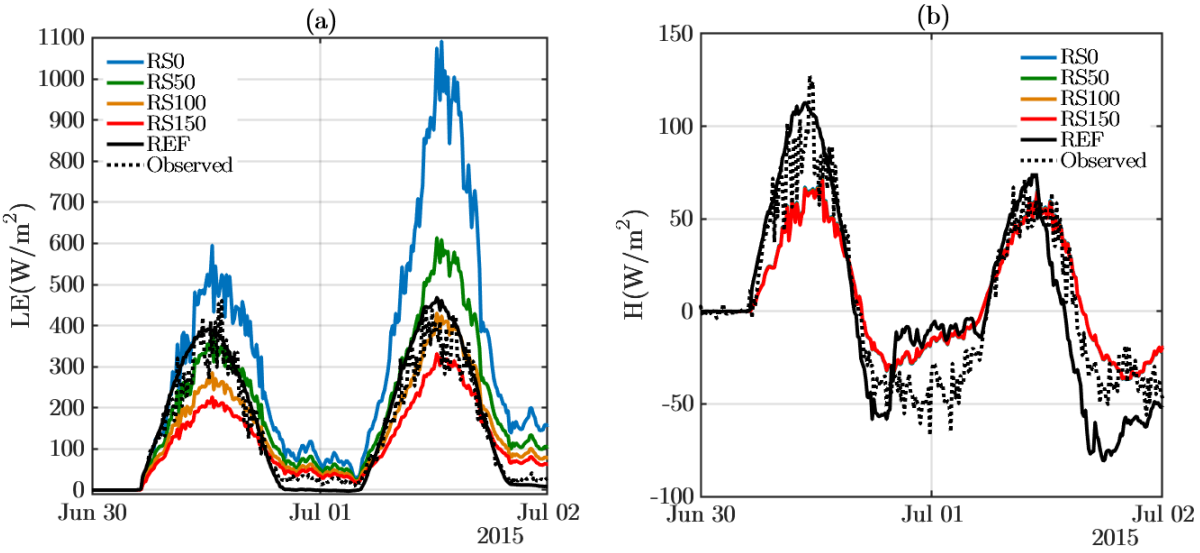

Figure 5.3: Observed and modelled (a) latent heat flux and (b) sensible heat flux between 30/06/2015 and 02/07/2015 for different reference simulations.

The bottom-line is that both parameter sets predict the annual variations of the surface fluxes with great accuracy. In the next parts, the REF simulation will be examined in more detail.

A more detailed description of the surface fluxes predicted by the REF simulation is shown in figure 5.2. In figure 5.1 it has been shown that the annual variations of the latent heat flux are underestimated by 10 W/m^2, and the annual variations of the sensible heat flux are overestimated by 10 W/m^2 (figure 5.1). Figure 5.1 indicates that this offset is larger in the second half of the year (bottom panels), when the latent heat flux is underestimated by 15 W/m^2, compared to the 5 W/m^2 offset during the first half of the year (top panels).

The significant deviation of the modelled surface fluxes from the observations starting from July 2015 is most likely caused by the evolution of the soil water content, that creates vegetation water stress that lasts until the end of the year. An increase in root water stress in turn increases the surface canopy resistance, hence decreases the surface latent heat flux for a given forcing. The surface energy balance is then obtained by overestimating the sensible heat flux.

We notice that the magnitude of the modelled surface sensible heat flux is underestimated during night-time by $\sim$ 20 W/m^2. This is an indication that there is most likely a problem with the parametrization of the aerodynamic resistance or of the ground heat flux during night-time.

It must be noted that the quality of the surface fluxes in the REF simulation is much higher compared to those modelled by RACMO (figure 4.16), especially during July where REF predicts the latent heat flux with a root-mean-square error (RMSE) of 16 W/m^2 compared to the 70 W/m^2 RMSE of RACMO in the same period. This is most likely caused by an overestimation of the soil water stress of the vegetation during summer in RACMO. It is important to mention that RACMO calculates the surface fluxes in a fully coupled mode with the atmosphere, which means that these strong deviations can also be caused by problems in other parts of the model (for instance large scale circulation patterns).

Finally, the results of the RSx "constant surface resistance" simulations for two consecutive days in July are shown in figure 5.3. The use of the prescribed skin temperature and a constant surface canopy resistance can give similar results as the land surface model, provided that the correct numerical value for this resistance is used. This value is in practice difficult to estimate, as it strongly changes on short time-scales (minutes-days), and thus not really is a constant. For instance on June 30th, a value of 50 s/m seems well suited, while on July 1st a value of 100 s/m gives better surface fluxes. In any case, the wet surface approach ($r_{c,\mathrm{veg}}$ = 0 s/m) is not suited as it greatly overestimates the latent heat flux during daytime. Environmental factors affecting vegetation transpiration (e.g root water stress, cloud coverage) can change from one day to another, which makes this simple approach not adapted for extended simulations. Besides, the surface temperature is usually not known in advance, hence using a land surface model with a prognostic equation for the skin tem-

perature is necessary for prediction purposes.

Nevertheless, we insist that prescribing the skin temperature indeed does a slightly better job at modelling the surface sensible heat flux during night-time, compared to the REF simulation. Interestingly however, none of these "bench-mark" simulations give good predictions of the surface fluxes during the night between June 30th and July 1st. In fact the magnitude of the sensible heat is underestimated by 30 W/m^2 in all reference simulations during this night. The only possible explanation for this underestimation is the inaccurate parametrization of the aerodynamic resistance during stable conditions in the surface model (described in subsection 2.3.1), if we assume that the observed surface temperatures, near surface temperatures and sensible heat fluxes are accurate during this night (equation 2.39).

5.2. Sensitivity experiments

Using the REF simulation as a reference, the sensitivity of the model on several parameters is quantified by running the simulation with the same forcing but by changing these parameters within a realistic range, based on the results from chapter 4. The list of these sensitivity simulations is shown in table 5.2.

Name	Parameter	Value
LAI_1	LAI	1 m^2/m^2
LAI_2	LAI	2 m^2/m^2
LAI_3	LAI	3 m^2/m^2
LAI_4	LAI	4 m^2/m^2
LAI_5	LAI	5 m^2/m^2
z0m_1	z_{0m}	1×10^{-2} m
z0m_5	z_{0m}	5×10^{-2} m
z0m_10	z_{0m}	10×10^{-2} m
z0m_20	z_{0m}	20×10^{-2} m
Λ_5	Λ_{skin}	5 W/m^2/K
Λ_8	Λ_{skin}	8 W/m^2/K
Λ_10	Λ_{skin}	10 W/m^2/K
Λ_15	Λ_{skin}	15 W/m^2/K
Λ_20	Λ_{skin}	20 W/m^2/K
RSmin_40	$r_{s,\text{veg}_{\text{min}}}$	40 s/m
RSmin_100	$r_{s,\text{veg}_{\text{min}}}$	100 s/m
RSmin_110	$r_{s,\text{veg}_{\text{min}}}$	110 s/m
Cveg_80	c_{veg}	0.8
Cveg_100	c_{veg}	1

Table 5.2: Overview of LSM sensitivity experiments on individual vegetation parameters.

5.2.1. Leaf area index

Unlike the REF simulation, the first simulations called LAI_x use a constant value, x, for the leaf area index. In the model, the surface resistance of the vegetation is inversely propositional to the LAI (equation 2.48). This aims to model the up-scaling of the single-leaf stomatal resistance to the whole canopy resistance. As a result, any increase in the LAI is expected to decrease the surface vegetation resistance, and hence to increase the latent heat flux (equation 2.43), as long as the atmospheric forcing and the aerodynamic resistance remain the same.

The resulting turbulent surface fluxes values are shown in figure 5.4. Increasing the LAI from 1 m^2/m^2 to 5 m^2/m^2 enhances the maximum mean latent heat flux in July from 200 W/m^2 to 280 W/m^2, at the expense of a reduction in the maximum sensible heat flux from 150 W/m^2 to 80 W/m^2. A similar pattern is visible in winter (e.g. in February), although the absolute values for the surface fluxes are much smaller during this time of year. Furthermore, simulations using a LAI between 3 m^2/m^2 and 5 m^2/m^2 seem to perform equally well, with only a 10 W/m^2 difference in maximum modelled latent heat flux in summer. It may thus be concluded that the LAI parameter has a strong influence on daytime surface fluxes during summer, although a typical error of 1 m^2/m^2 of the LAI does not greatly affect the result.

5.2.2. Roughness lengths

Observations analysed by Beljaars and Holtslag (1991) indicate a variation of the surface roughness length for momentum between 1cm and 20cm, depending on the season and wind directions. Here we will explore the effect of using different roughness lengths, which in turn modify the surface fluxes, as larger values tend to increase the estimated drag coefficients and enhance the surface fluxes. The roughness length for heat is then prescribed accordingly using equation 4.2.

Increasing the roughness lengths hardly affects the monthly mean daily variation of the latent heat flux (maximum difference of 10 W/m^2), but slightly increases the sensible heat flux by 20 W/m^2 during daytime and by $\approx$ 5 W/m^2 during night-time in summer (not shown). Figures 5.5 and 5.6 show how the daily variations of the latent and sensible heat fluxes are affected by using different values for the roughness lengths. These two days were selected because of the strong deviations between RACMO predictions and observations at CESAR. During the night with very weak wind speeds (below 1 m/s) of June 30th, the sensible heat flux is zero, regardless of the roughness length. On the other hand, during the nights of July 1st and 2nd (when wind speeds exceed 3 m/s), increasing the roughness length from 1cm to 20cm increases the downward sensible heat flux by more

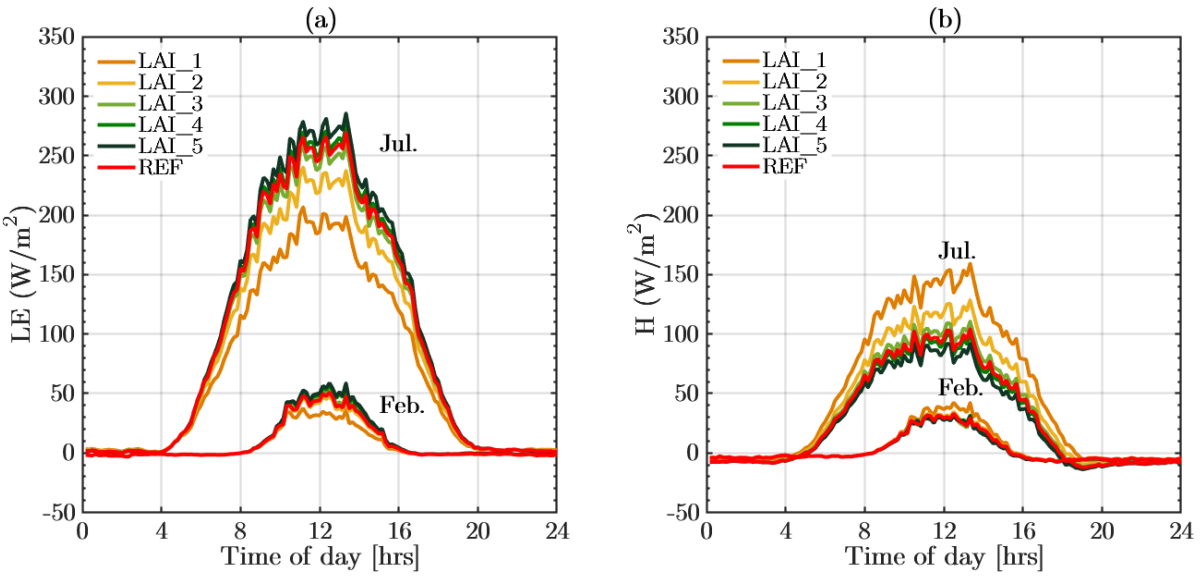

Figure 5.4: Monthly mean of modelled (a) latent heat flux and (b) sensible heat flux at the CESAR observatory in 2015 for different Leaf Area Index (LAI) values.

than 50 W/m^2 (figure 5.5).

Finally, the influence of the roughness length on the day-to-day variations of the surface fluxes is quite limited, as a maximum difference of less than 20 W/m^2 in sensible heat flux is observed among all simulations. This effect only becomes visible during night-time with sustained wind speeds as radiative forcing is most important during daytime, and weak winds strongly suppress the turbulent mixing during stable conditions (see figure 2.10).

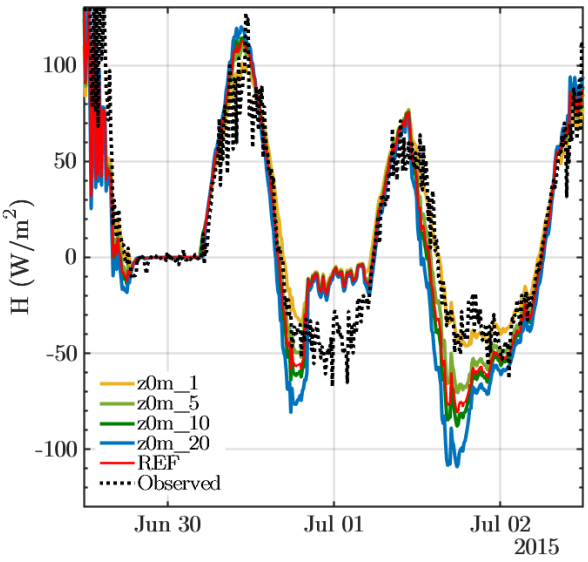

Figure 5.5: Observed and modelled surface sensible heat flux between 30/06/2015 and 02/07/2015 at the CESAR observatory using different values for the roughness lengths.

We will now investigate the effect of the roughness length on the modelled latent heat flux. During daytime, an increased roughness length slightly increases the maximum amount of latent heat flux (maximum of 10 W/m^2 increase in July, not shown). This is not the case overnight, due to the fact that an increased (downward) sensible heat flux reduces the amount of cooling of the surface, which prevents the surface to become saturated with water vapour. An example is shown in figure 5.6. During the night between July 3rd and 4th, a roughness length for momentum of 20 cm causes a very small (upward) latent heat flux whereas smaller roughness values cause (downward) dew deposition. This happens because a smaller downward sensible heat flux allows the surface to become saturated. This effect may be crucial for diurnal cycle simulations, as it strongly affects the amount of water transported between the surface and the atmosphere.

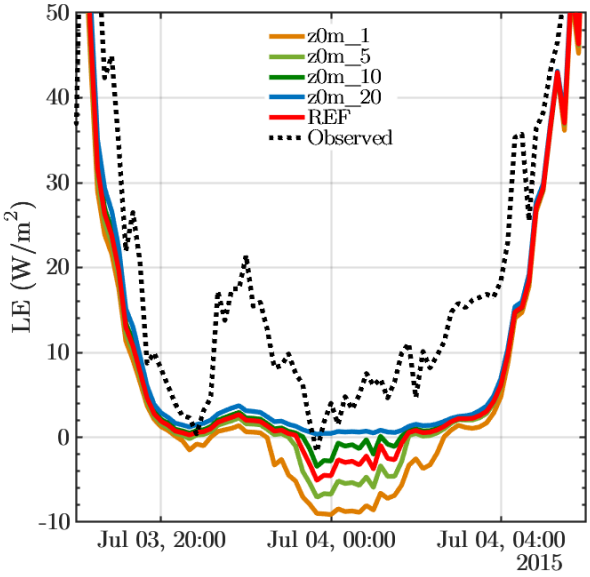

Figure 5.6: Observed and modelled surface latent heat flux during the night between 03/07/2015 and 04/07/2015 at the CESAR observatory using different roughness lengths.

The sudden increase in latent heat flux around 21:00 UTC is quite remarkable. This is also the time when measured visibility close to the surface decreases, which implies that liquid water is present in the atmosphere (mist/fog) which brings additional complications concerning the observed latent heat flux. The effect of liquid water in the first atmospheric level was, however, not taken into account in the forcing, which explains the mismatch between the model and the observations.

5.2.3. Skin heat conductivity

In the following experiments, the skin heat conductivity is taken as a constant and is varied between 5 W/m^2/K and 20 W/m^2/K. This corresponds to values between the estimated minimum during night-time winter and the estimated maximum during daytime summer, respectively (see figure 4.11). The results indicate that the skin heat conductivity greatly controls the daily evolution of the skin temperature, with higher values causing a smaller daily variation of the skin temperature (figure 5.7). This effect is most important during overnight, when the ground heat flux has relatively more importance in the surface energy balance.

It must be noted that the model extremely well represents the skin temperature during daytime in summer, independent of the exact value for the skin heat conductivity. This is caused by the fact that the skin temperature during daytime in summer is mainly controlled by the radiation and surface turbulent fluxes, hence the ground heat flux only represents a small fraction of the total surface energy balance. However, the skin temperature is poorly represented on a winter's night, and not a single tested value for the skin heat conductivity is able to correctly represent it's night-time evolution. Given the fact that the turbulent fluxes are small and rather well captured by the model, this mismatch is either caused by an incorrect treatment of the ground heat flux (in equation 2.28), or caused by the incorrect modelling of vertical turbulent transport overnight.

Although the deviation between observed and modelled skin temperature is rather large during daytime, it's effect on the turbulent heat fluxes remains limited as their modelled magnitudes are small.

The sensitivity of the modelled skin temperature on the skin heat conductivity for two consecutive days in summer is shown in figure 5.8. One might deduce from previous estimates, based on the method of Verhoef and Vidale (2012), (figure 5.7) that a value for Λ_{skin} ranging between 8 and 10 W/m^2/K is best suited for representing the monthly average daily evolution of the skin temperature in July. However, results represented in figure 5.8 reveal that the "best" value for Λ_{skin} actually changes from one day to another. For instance, 8 W/m^2/K seems preferable for the night between 29/06 and 30/06, while 20 W/m^2/K seems better for the night between 30/06 and 01/07, even tough a similar radiative cooling is observed ($\sim$ -40 W/m^2) during these two consecutive nights.

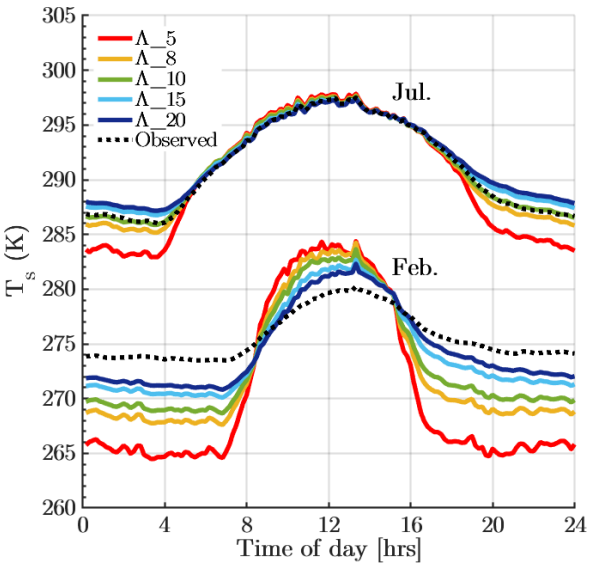

Figure 5.7: Monthly averaged daily evolution of the modelled and observed skin temperature at the CESAR observatory in 2015 using different values for the skin heat conductivity.

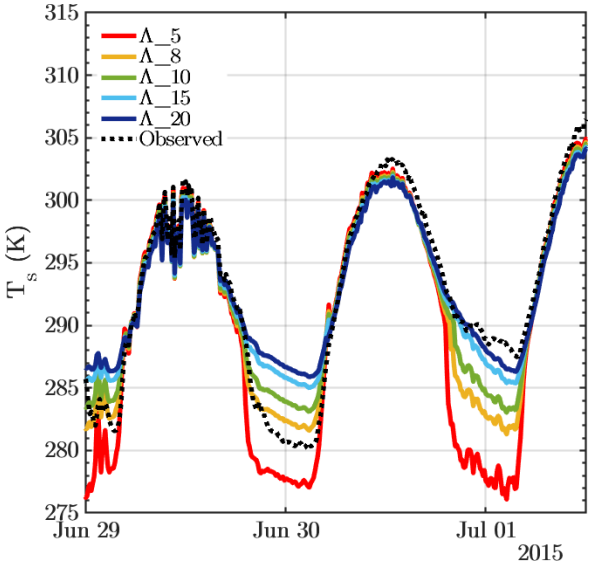

Figure 5.8: Observed and modelled skin temperature in at the CESAR observatory between 29/06/2015 and 01/07/2015 using different skin heat conductivity values.

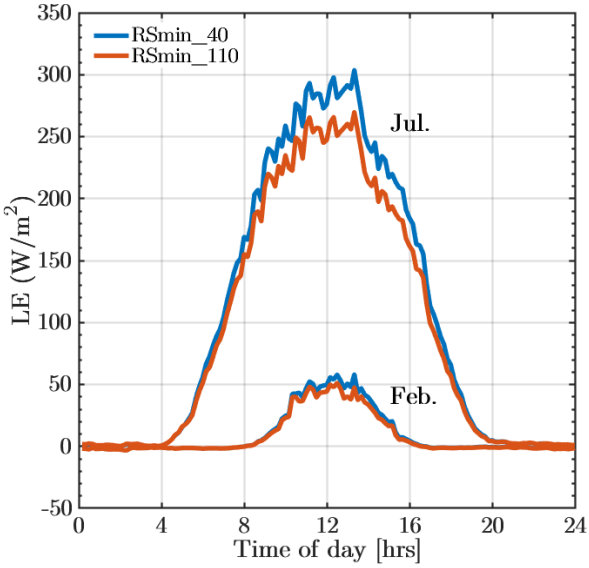

Figure 5.9: Monthly averaged daily evolution of the modelled surface latent heat flux at the CESAR observatory in 2015 using two different values for the minimum stomatal resistance of the vegetation.

The underlying reason for the different 'best' apparent conductivity values is the way turbulent transport is modelled during stable conditions. The first night is a night with very weak winds (< 1 m/s), which causes the modelled aerodynamic resistance to reach very high values (> 10^5 s/m), hence prevents the development of any turbulent flux. This is consistent with observations that suggest a very weak sensible heat flux (figure 5.5). However on the second night, both sustained winds (≈ 3 m/s) and a larger sensible heat flux are observed (figure 5.5), which reduce the observed surface cooling (figure 5.8). The model, however, still produces an important aerodynamic resistance (> 10^3 s/m) during the second night, which causes a strong dampening of the sensible heat flux. This ultimately means that only an overestimation of the ground heat flux, by means of an increased skin conductivity, is able to correctly model the cooling rate of the surface (figure 5.8).

To conclude, the skin heat conductivity Λ_{skin} is a very important parameter for heat transport overnight. However, an inaccurate description of the intensity of turbulence during stable conditions modifies it's apparently "best" value in order to comply with the observed surface cooling.

5.2.4. Minimum stomatal resistance of the vegetation

The effect of a decreased vegetation minimal stomatal resistance of the vegetation on the monthly averaged latent heat flux is displayed in figure 5.9. Using the value of 40 s/m, which is the value for short grass in the Ecoclimap database, instead of 110 s/m for $r_{s,\mathrm{veg}_{\mathrm{min}}}$ increases the latent heat flux, hence has the same effect on the latent heat flux as an increase of the LAI. This is what one might expected by looking at equations 2.48 and 2.49. Special care must thus be taken when changing the values of the LAI and the minimum surface resistance simultaneously, as different parameter sets can lead to the same result.

5.2.5. Vegetation fraction

The minimum bare soil resistance $r_{s,\mathrm{soil}_{\mathrm{min}}}$ (= 50 s/m) is smaller than the minimal vegetation surface resistance $r_{s,\mathrm{veg}}$ (= 110 s/m). So one might expect the latent heat flux to increase with decreasing fraction of vegetation. This effect is however not visible when only reducing the fractional vegetation cover c_{veg} to 80 % (not shown).

In fact, dry bare soil should be assigned a lower thermal emissivity than wet soil and vegetation (Mira et al., 2007). This which would then translate to higher skin temperatures for the same amount of emitted radiation (equation 2.37), hence increased turbulent fluxes. This has, however, never been tested as the parametrization of the surface emissivity has not yet been implemented in the model.

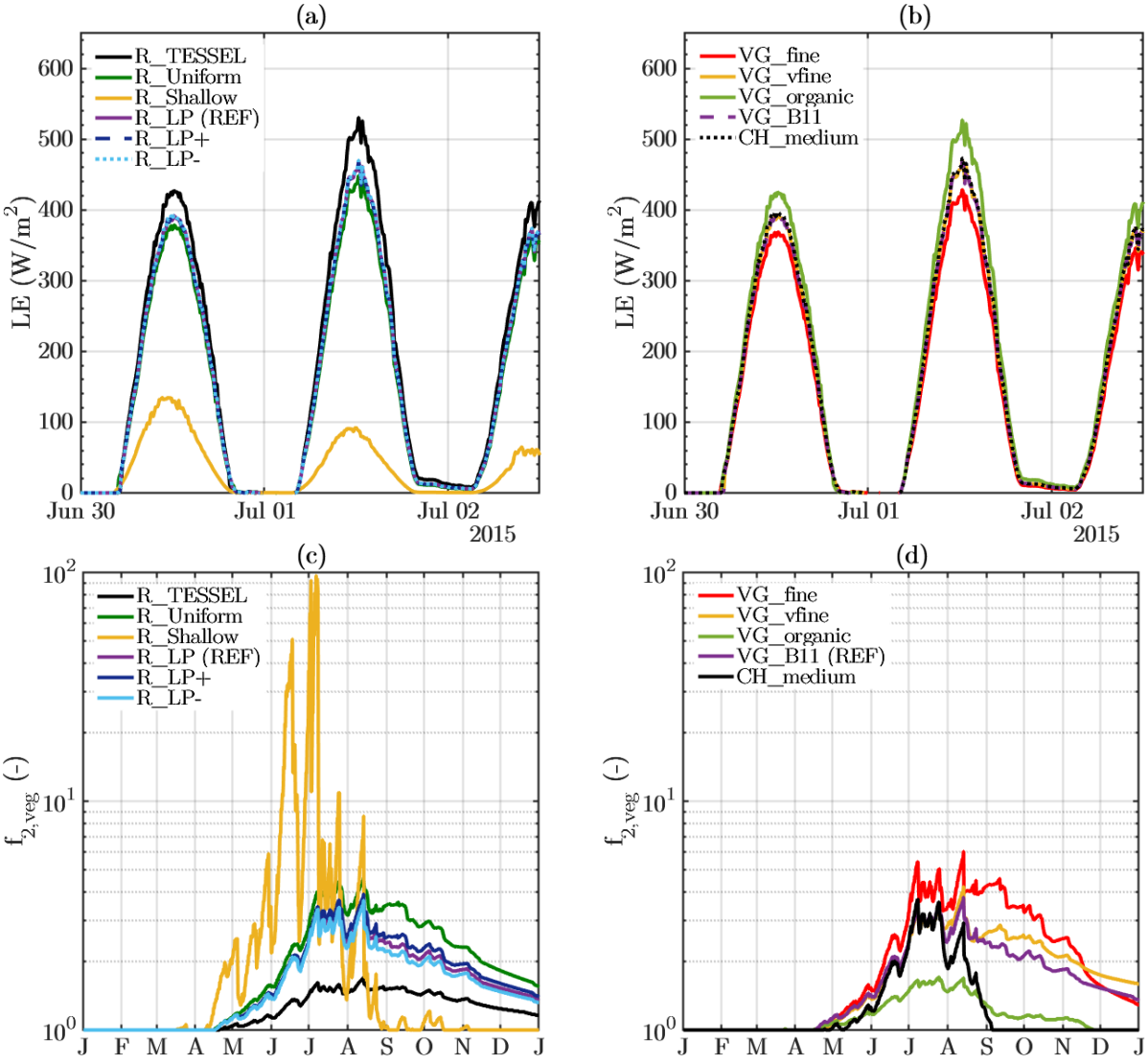

Figure 5.10: (a) & (c) Modelled surface latent heat flux at the CESAR observatory between 30/06/2015 and 02/07/2015 and (b) & (d) modelled vegetation water stress function at the CESAR observatory in 2015 using different root profiles (left panel) and different soil textures (right panel).

5.2.6. Root profiles and soil textures

The root profiles and the soil textures strongly affect the modelled water balance in the soil by means of the parametrization of the root water extraction (equation 3.15), and by means of the parametrization of the unsaturated soil hydraulic functions in the Richards equation for soil water transport (equation 2.19). The importance of these parameters is assessed by comparing the output for six different root profiles (tabulated in table 5.3) and five different soil textures (tabulated in 5.4), thereby keeping every other parameter constant using the values from the REF simulation.

Name	R1	R2	R3	R4
R_TESSEL	0.35	0.38	0.23	0.04
R_Uniform	0.10	0.30	0.40	0.00
R_Shallow	0.70	0.30	0.00	0.00
R_LP	0.40	0.30	0.30	0.00
R_LP+	0.30	0.35	0.35	0.00
R_LP-	0.50	0.25	0.25	0.00

Table 5.3: Overview of LSM sensitivity experiments with varying root profiles.

Name	Parametrization	Soil texture
CH_medium	C & H	USDA Medium
VG_fine	van Genuchten	ECMWF Fine
VG_vfine	van Genuchten	ECMWF V-fine
VG_organic	van Genuchten	ECMWF Organic
VG_B11	van Genuchten	Wösten B11

Table 5.4: Overview of LSM sensitivity experiments with varying soil textures. C & H stands for the Clapp and Hornberger parametrization.

The resulting modelled latent heat fluxes in early July and the predicted yearly variations of the water stress of the vegetation are displayed in figure 5.10. The difference between the different modelled surface fluxes only becomes distinguishable after mid-April, when the first vegetation water stress appears in the model. Each simulation models some vegetation soil water stress (panels (c) & (d)), but the amount of stress strongly differs across simulations.

The shallow root profile, which only contains roots in the first two layers (top 28cm), causes the most important soil water stress while the root profile used by the ECMWF, that contains roots in every soil layer, causes the least stress (panel (c)). The modelled stress reduces the amount of vegetation transpiration, and is most visible during the first days of July (panel (a)) when both available energy and stress reach a maximum.

In the model, the vegetation stress is written as a weighted sum of normalised soil water factors and layer thicknesses (equation 3.16), which means that the presence of even a small fraction of roots in deeper layers greatly reduces the vegetation stress, as long as the soil remains far from the permanent wilting point.

This being said, the resulting fluxes do indicate that only using roots in the first two layers is definitely inadequate, as it leads to greatly underestimated latent heat fluxes in summer (panel (a)). The use of the "best" root profile for the grass species present at the CESAR observatory produces the same latent heat flux as using an uniform root profile up to a depth of 70cm (simulation R_Uniform). In general, minor changes in the root profile lead to only minor changes in the vegetation stress function for soil water.

The soil texture has a notable influence on the amount of vegetation stress. A fine soil texture causes the largest stress while the organic soil causes the smallest stress. This is partly caused by the fact that the organic soil holds more water available for vegetation activity (defined as $\theta_{\mathrm{fc}} - \theta_{\mathrm{wp}}$). The ECMWF very-fine texture, the B-11 soil texture observed in the top 16cm of the soil at CESAR and the Clapp and Hornberger Medium class used in TESSEL cause a slightly different water stress (panel (d)), but the overall importance on summer evaporation remains negligible (panel (b)).

The deviation in the maximum latent heat flux caused by using a different soil texture is of the same order as using a slightly modified root profile, both roughly equal ~ 100 W/m^2 on July 1st 2015 (panels (a)) and (b)). The deviation in monthly averaged vegetation transpiration reaches a maximum of ~ 50 W/m^2 in July for all the considered root profiles and soil textures.

Remarkably, the vegetation stress persists until the end of all simulations except in the CH_medium run, regardless of the root profile or the soil texture. This is not what we might have expected at the CESAR site, where ditches continuously irrigate the soil during the year.

The reason for this persistent water stress in the model is the lower boundary condition for soil water transfer: in this model, free drainage is assumed (equation 3.11). This causes an important downwards water flux at the deepest soil level, especially in the start of the simulation (figure 5.12). This means that it is necessary to reconsider the free drainage boundary condition in order to be able to correctly model the change in water storage in the soil column (figure 5.11).

In the following part we investigate the soil water balance more closely. The soil water storage for different soil textures in time (figure 5.11), is calculated as :

$$S = \sum_{k=1}^{k_{\max}} \rho_w \theta_k D_k \quad \text{(mm)} \tag{5.1}$$

where ρ_w = 998 kg/m^3 is the density of water, θ_k is the volumetric soil water content in the kth layer and D_k is the thickness of the kth layer.

At the CESAR observatory, the soil typically starts losing water in April, but eventually completely replenishes after summer, even if the summer was very dry and warm like in 2006 (figure 5.11). In the model however, the rapid loss of soil water causes water stress, which tends to underestimate the latent heat flux after summer (figure 5.2 (c)) and overestimates the sensible heat flux (figure 5.2 (d)).

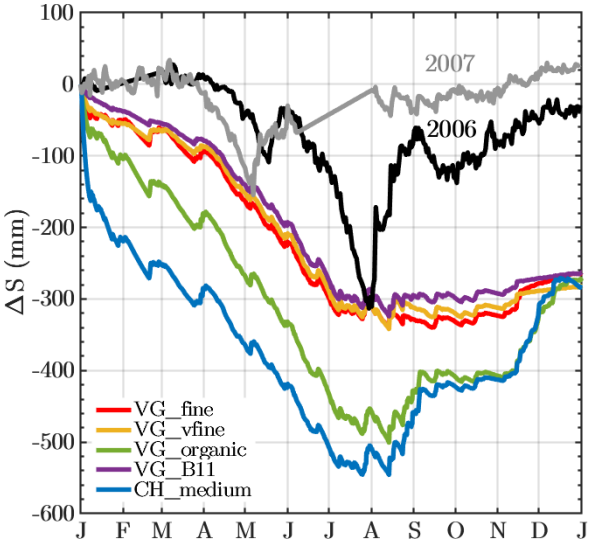

Figure 5.11: Modelled change of soil water storage at the CESAR observatory in 2015 (in mm of liquid water equivalent) using different soil textures. The sensor averages of the WUR measurements during the dry and wet years of 2006 and 2007 are shown in comparison.

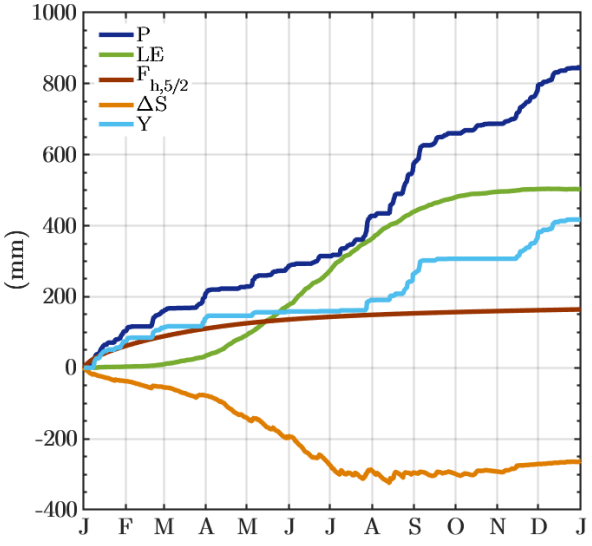

Figure 5.12: Modelled cumulative components of the soil/surface water balance at CESAR in 2015 for the REF simulation. P is the observed accumulated surface precipitation, LE is the predicted accumulated evapotranspiration, $F_{h,5/2}$ is the predicted accumulated downward water flux at the soil bottom, ΔS is the modelled change in soil water storage and Y is the accumulated the surface runoff.

The modelled water balance is shown in figure 5.12. Over the whole soil column, the water balance at each time step is written:

$$P = LE + F_{h,5/2} + Y + \Delta S \quad (\mathrm{kg/m^2/s}) \tag{5.2}$$

where P is the observed (input) surface precipitation, LE the (upwards) evapotranspiration, $F_{h,5/2}$ is the (downward) bottom soil water flux, Y is the surface runoff and ΔS is the relative change in soil water storage.

In the REF simulation, the accumulated evapotranspiration in the year of 2015 is equal to 500mm and accounts for approximately 60% of the 850mm yearly accumulated precipitation. The surface runoff accounts for a total of 400mm and the deep soil water drainage for 150mm (figure 5.12). The water balance is then fulfilled by the soil water reservoir, that loses 260mm of water over the whole year (figure 5.12). Comparison with measurements indicates that the yearly contribution of evapotranspirationto the water balance is well represented, but that the loss of water at the soil bottom is greatly overestimated (figure 5.11), due to the wrong representation of the lower boundary condition of the soil water transfer equation (free drainage) .

5.3. Summary

In this chapter, offline simulations of the land surface model using atmospheric forcing from the CESAR meteorological site, and applying different realistic parameter sets, have revealed the following features:

- The land surface model is able to model the yearly, monthly and daily variations of the turbulent surface fluxes with an accuracy of 10 $\mathrm{W/m^2}$ (figure 5.2).
- Using a seasonal variation of the LAI gives better monthly surface fluxes than using a fixed yearly value (figure 5.4).
- The roughness lengths for heat and momentum hardly affect the monthly variations of the surface turbulent fluxes, but strongly affect the night-time modelled surface fluxes (figure 5.5). This sensitivity on the roughness length has strong implications on the rate of cooling of the surface overnight (figure 5.6).
- The skin heat conductivity strongly affects the daily evolution of the skin temperature, especially the rate of warming/cooling during day-night transitions (figure 5.7).
- When the modelled sensible heat fluxes are underestimated overnight, the apparent optimal value for the skin conductivity in terms of surface cooling increases (figure 5.8).

- Reducing the value of the minimal vegetation stomatal resistance of increasing the LAI both increase the latent heat flux (figure 5.9).
- Reducing the fraction of vegetation by 20% barely affects the surface fluxes.
- The quality of the surface fluxes during dry summer days strongly depends on the presence or not of roots in the different soil layers. It is however not greatly affected by the numerical values of roots fractions (figure 5.10, panels (a) & (c)).
- The soil texture and parametrization strongly affects soil water transfer (figure 5.11), but the overall effect on soil water stress and surface evapotranspiration remains limited (maximum difference of 100 W/m^2 in July) (figure 5.5 panels (b) & (d)).
- The land surface model causes too much water stress after summer due to the overestimation of the lower boundary water flux, which is set to free drainage (figures 5.11 & 5.12).
- The modelled water balance is closed, and the yearly cumulative evapotranspiration was found to be equal to 500 mm in 2015, which accounts for ≈ 60% of the observed accumulated precipitation during this year at CESAR (figure 5.12).

5.4. Suggestions

This chapter summarised the performance of the land surface model, and investigated the sensitivity of the modelled turbulent fluxes on the input parameters. It has been shown that the modified land surface model in DALES is able to reproduce the monthly variations of the surface fluxes with an accuracy of 10 W/m^2. However, several aspects in the land surface model need further improvement to enable extended simulations (yearly cycle), or to perform daily-cycle simulations with high temporal resolution.

First, the lower boundary condition for soil moisture transport, assuming free drainage, is not adapted for the CESAR site, which clearly causes too much soil water loss. This will cause too much soil water stress (i.e underestimation of the vegetation transpiration) for simulations that extend in time, especially in summer. This anomaly could be repaired by assimilating soil moisture measurements. However the strong observed horizontal heterogeneity in soil textures, physical processes that are not accounted for in the model (such as horizontal soil water flow, fast precipitation channelling in dry soils, irrigation), and the important uncertainty in soil moisture measurements make soil moisture assimilation a challenging task.

Secondly, the drag coefficients overnight are most likely underestimated, which leads to a strong underestimation of the magnitude of the surface fluxes. This has important consequence for diurnal cycle simulations, as it strongly affects the rate of surface cooling. This effect could be compensated for by adapting the value of the skin heat conductivity, which greatly controls the heat transfer from the soil to the surface during night-time.

Finally, many land surface parameters such as the LAI, the roughness lengths and the shortwave albedo, still need to be adjusted as function of time in the model. For simulations that extend over more than a couple of weeks, a time-dependent land surface parameter file is necessary. For prediction purposes, these parameters can only be taken from a climatology database (e.g. ecoclimap), as the LAI, the grass height and the albedo are generally not known in advance.

6 Coupled simulations

The previous sections have demonstrated that the use of land surface parameters obtained from observations in a modified version of the TESSEL land surface model provides a very accurate representation of the turbulent surface fluxes under a given atmospheric forcing at CESAR. The aim of this final chapter is to test the land surface model in a fully coupled turbulence/radiation/surface approach and to illustrate some important atmospheric feedback processes between the land surface and the atmospheric boundary layer.

This chapter contains three sections which together describe in detail the fully-coupled simulation results for day-time stratocumulus development (section 1), for the growth of a convective boundary layer during a very warm day in July (section 2) and finally for radiative fog formation, growth and dissipation (section 3).

Unless stated otherwise, the initial soil temperature of each simulation is taken from KNMI measurements at the CESAR observatory up to 50cm depth, then linearly extrapolated to the prescribed temperature below the soil model column. The volumetric soil water content is initialised at field capacity and the surface temperature is initialised using measured upward radiation and assuming a surface emissivity of 0.98. The prescribed surface pressure is given by KNMI observations, and the profiles of large-scale geostrophic winds, large-scale subsidence and large-scale changes due to horizontal advection of temperature and humidity are prescribed every 10-min using RACMO. Finally, the vertical profiles of temperature and humidity above the model domain and required by the radiation scheme are given by RACMO and averaged over the whole simulation time window. Standard ozone and trace gas profiles are used for the radiation absorption calculations above the model domain.

6.1. Stratocumulus case

6.1.1. Case description

The present study of sratocumulus development was observed at CESAR on February 18th, 2011. Both Lidar and ceilometer backscatter measurements indicate a cloud base ranging between 400m and 600m, while the Nubiscope cloud scanning instrument measures a 100% cloud coverage during the whole day. At the same time, a strong thermal inversion was present at a height of 1000m, with large-scale subsidence at the end of the day (figure E.1). These four indicators allow us to conclude that a stratocumulus layer is present according to the method developed by Schuurbiers (2014).

Heuff (2016) simulated this case with DALES assuming a saturated ground surface, and found that increasing the surface evaporation or decreasing the cloud droplet concentration both increase the vertically integrated liquid water content, also called liquid water path (LWP), of the stratocumulus layer. On the one hand, increased evaporation at the ground surface acts as an enhanced source of moisture, which tends to increase the stratocumulus LWP. On the other hand, a smaller cloud droplet concentration number (CDCN) causes the formation of fewer but larger liquid water droplets, which tend to precipitate faster (Lohmann and Feichter, 2005). This will act as a sink term in the cloud LWP budget.

Note that the CDCN and the surface evaporation are not independent, as the amount of net available radiation at the surface is strongly dependent on the amount of solar radiation backscattered at the cloud top, which is in turn strongly related to the size and amount of cloud droplets. The aim of the following experiments is to assess whether the effect of downward radiation on evaporation is important, by examining the sensitivity of the LWP on different values of CDC using a coupled land surface model.

The experiments are summarised in table 6.1. The REF simulations use the surface parameters derived in chapter 4 and are listed in Appendix C. The STRD experiment uses the standard surface parameters from the TESSEL 'short grass' vegetation type, while the RS_0 experiment uses a vegetation stomatal resistance of 0 s/m, i.e calculates the Penman potential evaporation. Finally the sensitivity experiments are identical to the REF experiment but use a different value for the cloud droplet concentration number.

The initial profiles and large-scale forcings are shown in figure E.1. The initial profiles of liquid water potential temperature and total specific humidity are

Name	Surface model	CDCN (cm^3/cm^3)	Comments
REF	Interactive	100	REF parameters (App. C)
STRD	Interactive	100	Standard parameters (App. C)
RS_0	Penman evaporation ($r_s = 0$)	100	-
NC_50	Interactive	50	REF parameters
NC_75	Interactive	75	REF parameters
NC_150	Interactive	150	REF parameters
NC_200	Interactive	200	REF parameters
NC_1000	Interactive	1000	REF parameters

Table 6.1: List of DALES stratocumulus simulations.

derived from tower observations at CESAR up to the inversion height. It is assumed that the horizontally mean values of these two variables are vertically well mixed up to the inversion layer. The inversion layer height is calculated by matching the LWP, which is directly imposed by the vertical profiles of θ_l and q_t with the measured LWP by the HATPRO radiometer. Next, in the absence of observations, RACMO is used to derive the vertical profiles above the inversion layer. The initial wind vector profile is taken from RACMO.

The grid is composed of 128x128x200 grid points that extend over an area of 6400x6400x2000 meters. The horizontal advection of liquid water potential temperature ranges between -0.2 and 0.2 K/hour, while the horizontal advection of specific humidity ranges between 0 and 0.1 g/kg/hour. An important subsidence of $\approx$ 1 cm/s is present between 16:00 UTC and 21:00 UTC at a height of 1500m (figure E.1).

6.1.2. Results of the reference simulations

The different components of the surface radiation and of the surface energy balance, predicted by the REF simulation, are shown in figure 6.1. The modelled net radiation at the surface is underestimated by 15 W/m^2 during daytime (left panel), mainly because the absorbed shortwave radiation is slightly too small (right panel). The surface latent heat flux is underestimated by 5 W/m^2 whereas the sensible heat flux is overestimated by 10 W/m^2. Finally, the absolute value of the (upwards) ground heat flux is overestimated by approximately 10 W/m^2.

The overall quality of the land surface model in a fully coupled mode is the same as for the offline simulations from the previous chapter. However, the small mismatch between observed and modelled fluxes has important consequences for the predicted evolution of the soil column and atmospheric boundary layer. The modelled upper soil temperature, skin temperature and 10m mixed-layer air temperature are shown in figure 6.2. Due to the underestimation of absorbed radiation at the surface of 20 W/m^2 at the start of the simulation (figure 6.1), the modelled skin layer cools down by 1°C in order to respect the surface energy balance (figure 6.2). This will eventually cause the upper-soil temperature to cool too fast, as the ground heat flux is overestimated.

Most interestingly, observations indicate a negative (downward) sensible heat flux after 15:00 UTC, even though the estimated surface temperature is still more than 1°C warmer than the air temperature at 10m height.

Despite some mismatches between modelled and observed surface fluxes, the fully coupled model is able to accurately model the liquid water path of the stratocumulus layer (figure 6.3). For the REF simulation, the latent heat flux decreases from 15 W/m^2 at noon, when the net absorbed radiation is maximum, down to 4 W/m^2 after 16:00 UTC at sunset, when the net absorbed radiation at the surface becomes negative.

In the STRD simulation, the surface evaporation is increased by several W/m^2, but the effect on the cloud LWP is negligible. However in the RS_0 simulation, the latent heat flux is doubled which translates in a faster increase of the cloud LWP from 12:00 to 17:00 UTC. After 17:00, precipitation and subsidence become more important than the mixing of moist air at the cloud base, which tends to decrease the LWP in the same way as we have seen in the REF simulation.

6.1.3. Sensitivity to the cloud droplet concentration

The effect of the cloud droplet concentration number (CDCN), which is a fixed parameter in the model, is shown in figure 6.3. Decreasing the CDCN from 1000 cm $^{-3}$ to 50 cm $^{-3}$ causes, for the same LWP, the formation of larger droplets, which precipitate earlier than smaller droplets. This effect is clearly

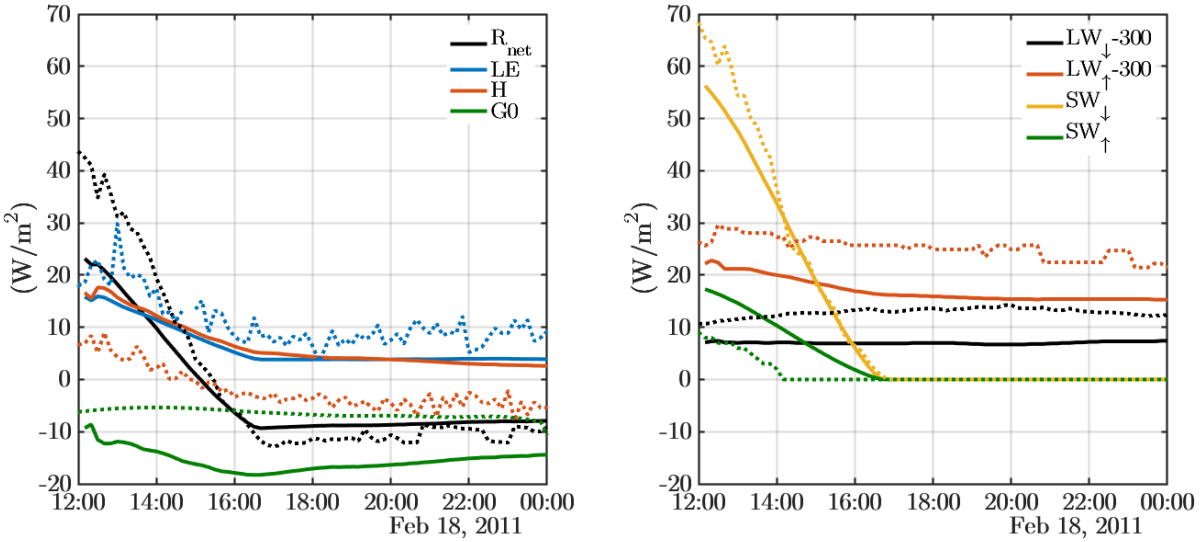

Figure 6.1: Left: Modelled (thick lines) and observed (dashed lines) components of the surface energy balance for the REF stratocumulus simulation at the CESAR observatory. Right: Modelled (thick lines) and observed (dashed lines) radiation components at the surface for the REF stratocumulus simulation at the CESAR observatory.

visible at 15:00 UTC, when the LWP in the NC_50 starts decreasing while the LWP continues to increase in other simulations. This is consistent with results from Heuff (2016), although the sensitivity of the LWP to the CDCN is much smaller due to a much smaller modelled surface latent heat flux.

Furthermore, in our simulations, the radiation and the surface fluxes are connected through the surface energy balance. This means that for higher CDCN values, the surface latent heat flux decreases due to a subsequent increase in the optical depth of the cloud layer. This is physically caused by the increase of the surface area on which the incoming solar radiation is backscattered, in the presence of more but smaller droplets.

This effect is visible from 12:00 to 16:00 UTC, as the modelled latent heat flux in the NC_1000 simulation is almost half of the modelled latent heat flux in the REF simulation. One might then expect the LWP to increase faster for smaller CDCN values, but this is not what is observed (right panel). During this day, the decrease of the CDCN has a too small effect on the latent heat flux for it to counter the effect of increased precipitation.

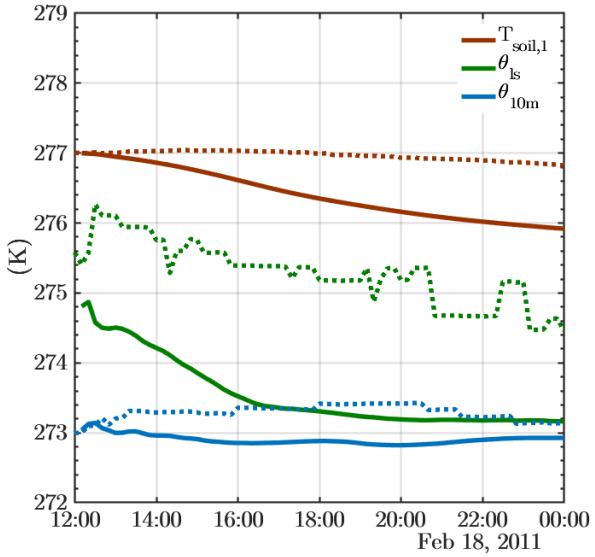

Figure 6.2: Modelled (thick lines) and observed (dashed lines) temporal evolution of the upper soil temperature, the surface liquid water potential temperature and the potential temperature at 10m height for the REF stratocumulus simulation at the CESAR site on 18/02/2011. Time is in UTC.

6.1.4. Summary and discussion

The simulations results discussed in the first section have demonstrated that the use of a coupled land surface model improves the accuracy of the model to predict the observed surface fluxes, which in turn increases the accuracy of the predicted cloud liquid water path of a stracocumulus layer on a winter day in 2011. For such a case without water stress and with hardly available net radiation at the surface, the use of the standard 'first guess' land surface parameter set gives very similar results as the use of a reference

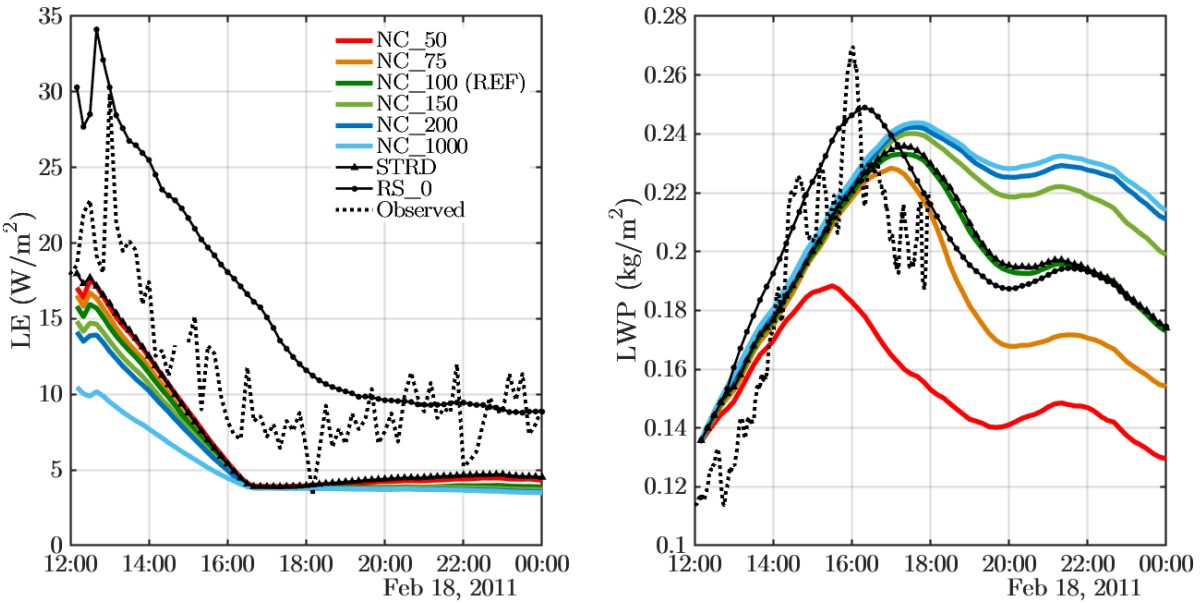

Figure 6.3: Left: Modelled (thick lines) and observed (dashed lines) surface latent heat flux. Right: Modelled (thick lines) and observed (dashed lines) cloud liquid water path (LWP) for the different simulations at the CESAR site on 18/02/2011. Time is in UTC.

'best' land surface parameter set, specially derived for the CESAR observatory and for that season.

The cloud droplet concentration number (CDCN), a fixed parameter in the microphysical parametrization of the LES model, plays an important role in determining the triggering time of precipitation and the amount of solar radiation that reaches the surface. It therefore affects the amount of surface latent heat flux and could thus compensate for the thinning of the stratocumulus by precipitation. However, fully coupled surface/radiation/LES simulations indicate that the increase in precipitation is more important than the increase in surface latent heat flux for lower values of CDCN in the liquid water path budget during this particular stratocumulus case.

6.2. Clear summer convective boundary layer case

6.2.1. Case description

The coupled Land surface / LES model is tested during the warm and convective day of July 1st, 2015. This day was chosen because the regional weather forecast model RACMO considerably underestimated the surface latent heat flux and overestimated the sensible heat flux during daytime at the CESAR site. This was partly caused by the initial soil moisture, that was actually very close to the permanent wilting point hence caused significant soil water stress in RACMO. This strong overestimation of the sensible heat flux in RACMO partly predicted the mixed-layer to become too warm and too deep, which led to a strong over-estimation of the near surface air temperatures at the CESAR site. The aim of the following simulations is to investigate the influence of different surface parametrizations, especially concerning vegetation water stress, on the development of the convective boundary layer (CBL).

The experiments are summarised in table 6.2. Every simulation is initialised at 08:00 UTC at the CESAR site, and executed until July 2nd 2015 at 00:00 UTC. The REF simulation uses the optimal land surface parameters derived in Chapter 4 for the CESAR site in July 2015, which are summarised in Appendix C. A leaf area index of 3.5 m^2/m^2 is used, based on the Ecoclimap database and on PROBA-V satellite estimates (figure 4.6). The roughness lengths for momentum and heat are set to 0.15m and 0.235×10^{-4}m respectively, which correspond to the observed maximum values during summer at the CESAR site by Beljaars and Holtslag (1991) (figure 4.8). The surface albedo is set to 0.23 (figure 4.9) and the skin heat capacity is set to 15 $W/m^2/s$ (figure 4.11). The STRD simulation uses the standard land surface parameters from the TESSEL 'short grass' vegetation type (Appendix C).

Unless stated otherwise, in table 6.2, the following setup is used for all the simulations. The initial profiles of liquid water potential temperature and total specific humidity up to 200m height are taken from tower observations at 08:00 UTC. Unfortunately, radiosonde observations were only available at 00:00

Name	Surface model	Comments
REF	Land surface model (LSM)	Reference land surface parameters
STRD	LSM	Standard land surface parameters
ISURF_2	Surface temperature prescribed	Homogeneous surface temperature, wet surface approach (r_s = 0)
ISURF_4	Surface fluxes prescribed	Homogeneous surface fluxes
RS_0	LSM	No vegetation control (r_s = 0)
ADV_off	LSM	No advection of θ_l and q_t
INI_ST_-2	LSM	ΔT_{soil} = -2K
INI_ST_+2	LSM	ΔT_{soil} = +2K
INI_SM_1	LSM	θ_{soil} = [0.320 0.320 0.320 0.320](m^3/m^3) $f_{2,veg}$ = 1000
INI_SM_2	LSM	θ_{soil} = [0.320 0.320 0.424 0.528](m^3/m^3) $f_{2,veg}$ = 2.8
INI_SM_3	LSM	θ_{soil} = [0.320 0.389 0.459 0.528](m^3/m^3) $f_{2,veg}$ = 1.9
Λ_5	LSM	Λ_{skin} = 5 W/m^2/K
Λ_10	LSM	Λ_{skin} = 10 W/m^2/K
Λ_20	LSM	Λ_{skin} = 20 W/m^2/K
C_skin_28000	LSM	C_{skin} = 28000 J/m^2/K

Table 6.2: List of clear convective boundary layer DALES experiments.

UTC, so the LES model has to be initialised first at 00:00 UTC using both tower and radiosonde data, and then executed until 08:00 UTC. This first run is stopped at this time and reinitialised below 400m using tower observations in order to avoid the increasing complexity that comes with adequately modelling the stable boundary layer evolution. Cubical interpolation is performed between the tower data at 200m and the LES output at 400m. The initial wind vector profile is taken from RACMO output. The initialisation and large scale forcing are shown in figure E.2.

The grid is composed of 128x128x200 grid points that extend over an area of 6400x6400x3000 meters. The horizontal advection of liquid water potential temperature ranges between -0.4 and 0.4 K/hour, while the horizontal advection of specific humidity ranges between -0.4 and 1.4 g/kg/hour. An important subsidence of ≈ 2 cm/s is present between 16:00 UTC and 20:00 UTC at a height of 2000m (figure E.2).

6.2.2. Reference simulation

The detailed description of the output of the REF simulation is shown in figure 6.4. The overall agreement between modelled and observed surface fluxes can be said to be satisfactory. The net absorbed radiation by the surface (overestimated by approximately 50 W/m^2), is redistributed through the surface latent heat flux LE (overestimated by 50 W/m^2), the surface sensible heat flux H (accurate within 10 W/m^2) and the ground heat flux G_0 (overestimated by more than 50 W/m^2). The surface sensible heat flux warms the air near the surface, which cause these warm air parcels to rise until the inversion layer by entrainment. At 18:00 UTC, the mixed layer has grown up to 900m height (figure 6.5).

The comparison with radiosonde observations at the end of the simulation, on 02/07/2015 at 00:00 UTC, reveals that the modelled boundary layer is too cold and too wet as opposed to the REF simulation. It is also interesting to notice that the observed inversion height, remaining from the daytime convective boundary layer at the end of the simulation, is situated at approximately 1800m, while it did not exceed 900m in the REF simulation.

6.2.3. Budget analysis

A more detailed analysis of the potential temperature budget in the REF simulation may tell us what prevents the potential temperature to reach the observed values in the mixed layer in our simulations.

The time- and domain- averaged budget equation for θ_l may be obtained by integrating the budget equation 2.75 between the start and the end of the simulation in time, and between the surface and the LES domain top in the vertical direction, where the

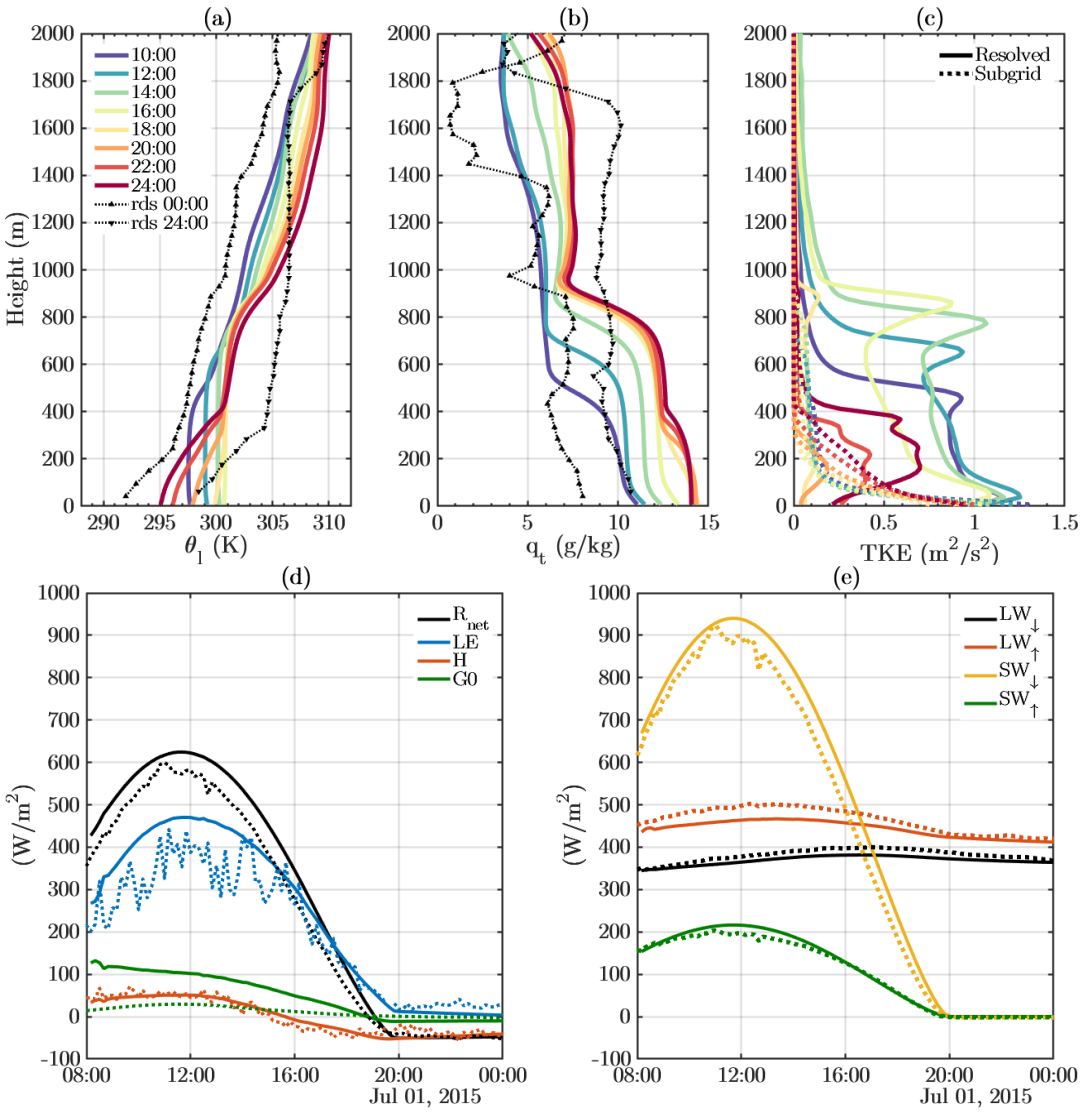

Figure 6.4: Top panels: Modelled and observed vertical profiles of (a) liquid water potential temperature, (b) total specific humidity (c) turbulent kinetic energy at the CESAR observatory on 01/07/2015. The KNMI radisosonde observations are at 00:00 UTC and taken from De Bilt. Bottom panel: Observed and modelled (d) surface energy balance and (e) surface radiation budget at the CESAR site on 01/07/2015 for the REF simulation.

turbulent flux is zero:

$$
\begin{aligned}
&\underbrace{\frac{1}{z_{\max}}\int_{t_0}^{t_{\max}}\int_{\mathrm{sfc}}^{z_{\max}}\frac{\partial\overline{\theta_l}}{\partial t}\,\mathrm{dzdt}}_{\text{(1) temperature tendency}} = \\
&\underbrace{-\frac{1}{z_{\max}}\int_{t_0}^{t_{\max}}\int_{\mathrm{sfc}}^{z_{\max}}\left(\overline{u_h}\frac{\partial\overline{\theta_l}}{\partial x_h}+\overline{w}\frac{\partial\overline{\theta_l}}{\partial z}\right)\mathrm{dzdt}}_{\text{(2) large-scale advection}} \\
&\underbrace{+\frac{1}{z_{\max}}\int_{t_0}^{t_{\max}}\overline{w'\theta_l'}_{\mathrm{sfc}}\,\mathrm{dt}}_{\text{(3) surface sensible heat flux}} \\
&\underbrace{-\frac{1}{z_{\max}}\int_{t_0}^{t_{\max}}\int_{\mathrm{sfc}}^{z_{\max}}F_{\mathrm{rad}}\,\mathrm{dzdt}}_{\text{(4) radiation}}
\end{aligned}
\tag{6.1}
$$

The change in domain-averaged θ_l (subscript (1)) can be diagnosed from both the LES result and from radiosonde observations. The large-scale advection term (subscript (2)) can only be diagnosed from RACMO, the sensible heat flux contribution (subscript (3)) can be diagnosed from both tower observations and LES results and finally the radiative tendencies (subscript (4)) can only be diagnosed using LES results. The resulting value for the REF experiment are shown in table 6.3.

Budget term (K/hour)	(1)	(2)	(3)	(4)
DALES (REF)	0.137	/	-0.003	-0.045
CESAR	0.198	/	-0.004	/
RACMO	/	0.193	/	/

Table 6.3: Estimated terms of the θ_l budget (6.1) for the REF experiment integrated from 08:00 to 24:00 UTC in time and from 0 to 3000m in height.

The modelled domain-averaged potential temperature increases 0.06 K/hour less than what is measured by the radiosonde (Table 6.3). The contribution of the surface sensible heat flux to both the observed and the modelled potential temperature is very small (<0.01 K/hour) compared to the diagnosed contribution of the large-scale advection by RACMO ($\approx 0.2K/h$). It is thus most likely that a small bias of the large-scale advection in RACMO can explain the underestimation of the potential temperature in the REF simulation. It is however still difficult to completely disentangle the contribution of the surface fluxes and the large-scale advection, as the 10-min averaged eddy-covariance measurements might underestimate the surface fluxes due to the presence of larger turbulent scales.

6.2.4. Influence of the surface model

The resulting temporal evolution of the horizontally averaged surface fluxes, inversion height and surface temperature are shown in figure 6.5. The STRD simulation, which uses 'first guess' land surface parameters taken from the ECMWF-TESSEL model (Appendix C), slightly overestimates both the surface latent heat flux and sensible heat flux by 10 W/m^2 and 20 W/m^2, respectively (top panels). It is remarkable that for this case, the STRD and REF simulations give very close results although they use very different land surface parameters (LAI, z_0, Λ_{skin}). This is mainly because there is no water stress, hence the parametrization of the soil water transfer (root fraction, soil textures) does not influence the plant transpiration. Furthermore, the increase in the roughness lengths z_0 enhances the surface fluxes, but this effect is almost completely compensated by simultaneous decrease of the leaf area index LAI and of the skin heat conductivity Λ_{skin}.

The ISURF_2 simulation uses a prescribed surface temperature from surface radiation measurements and the wet-surface approach. The surface fluxes are thus simply diagnosed using the difference in potential temperature and the stability at the lowest LES level. It was found that this approach greatly overestimates the surface fluxes, as it does not include the vegetation stomatal control and the ground heat flux. Interestingly, the RS_0 simulation gives much more accurate surface fluxes than the ISURF_2 simulation (panels (a) and (b)), but greatly decreases the skin temperature (panel (d)). This run uses the land surface model but assumes that there is no vegetation control on the latent heat flux. This approach thus also assumes a wet surface, but still accounts for a ground heat flux, and solves the surface energy balance for the skin temperature.

Understanding why the three simulations that use the interactive land surface model (REF, STRD, RS_0) underestimate the surface temperature by several degrees is not evident (panel (d) in figure 6.5). Maybe the ISURF_4 simulation provides the answer. This simulation uses prescribed surface fluxes, taken from eddy-covariance observations, and diagnoses the surface temperature from the surface fluxes and the diagnosed aerodynamic resistance at the lowest LES level.

Most interestingly, the ISURF_4 run gives a very similar surface temperature evolution as in the simulations that have a prognostic equation for the surface temperature. Assuming that the prescribed surface fluxes reflect reality, the mismatch between diagnosed and observed surface temperatures can be explained by only two different arguments (see equation 2.39): (1) an underestimation of the modelled near surface air temperature (2) the overestimation of the modelled aerodynamic resistance in the ISURF_4 simulation.

6.2.5. Sensitivity to soil initialisation

The modelled horizontally averaged vertical profiles at 16:00 UTC as well as the temporal evolution of the surface fluxes for different initial profiles of soil moisture and soil temperature are shown in figure 6.6. The initial profiles of soil moisture have been chosen such that a different water stress for vegetation is present at the start of each simulation (see table 6.2 for the exact values).

Any increase in the water stress of the vegetation causes an important decrease in the surface latent heat flux, which translates to an equally important increase of the sensible heat flux (bottom panel). The latter causes the near surface air to warm much faster, which increases the production of turbulent kinetic energy. Eventually, the mixed-layer temperature and height both increase due to entrainment, while the specific humidity decreases (top panels).

The temporal evolution of the convective boundary

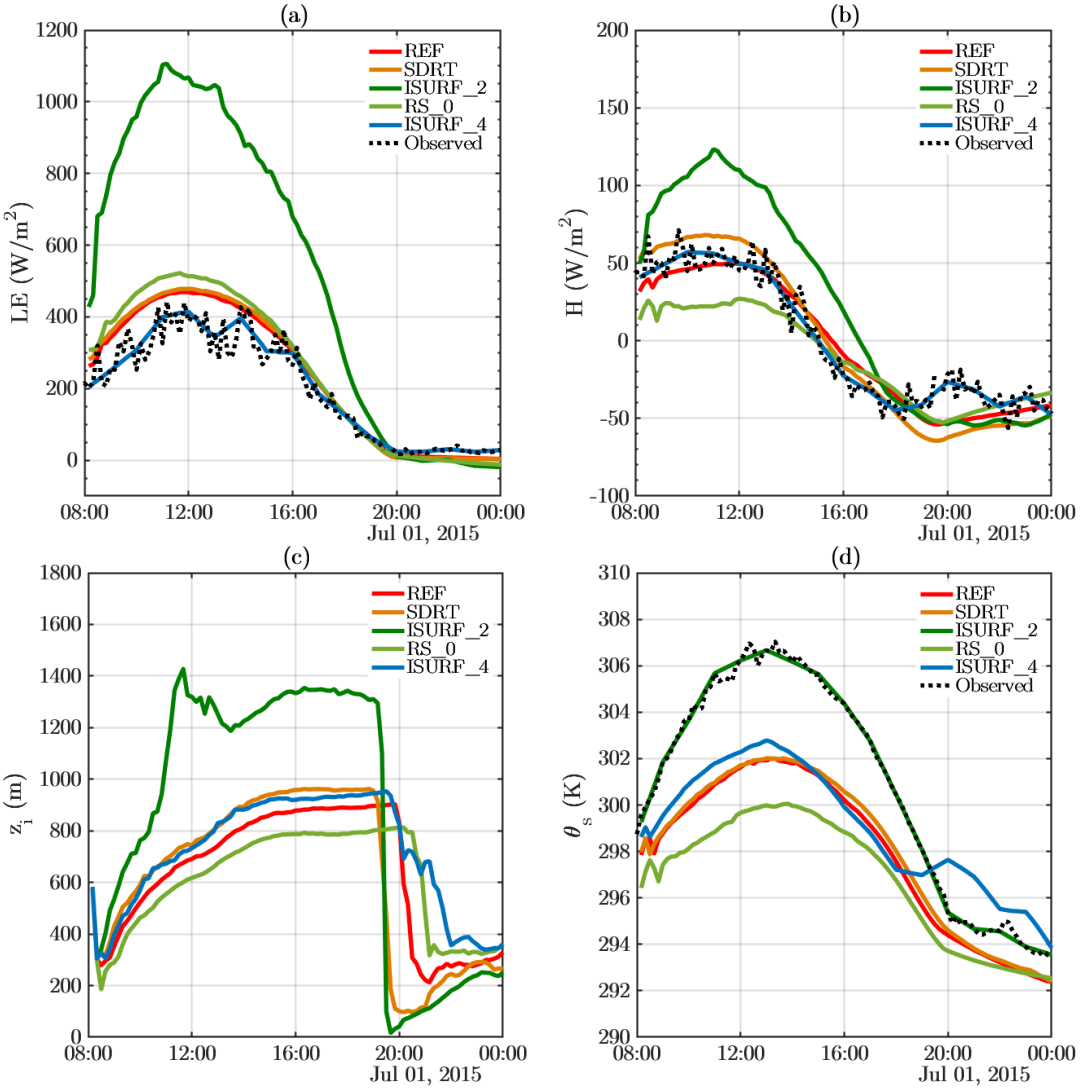

Figure 6.5: Modelled and observed (a) surface latent heat flux, (b) surface sensible heat flux (c) inversion height and (d) surface potential temperature at the CESAR site on 01/07/2015 for different surface parametrizations.

layer does not seem to be very much affected upon increasing (resp. decreasing) the initial soil temperatures. The latter mostly increases (resp. decreases) the surface latent heat flux (panel (d)).

6.2.6. Sensitivity to the skin layer heat conductivity

The modelled surface heat fluxes and difference of the near surface air temperature and soil temperature are shown in figure 6.7. Decreasing the skin heat conductivity greatly decreases the amount of heat that is transported towards the soil (panel (b)), which is predominantly compensated by an increase in the latent heat flux.

Changing the skin heat conductivity has strong implications for the thermal coupling between the soil and the atmosphere, as a smaller ground heat flux causes the upper-soil temperature to increase more slowly during daytime. Most interestingly, for a value of the skin heat conductivity as small as 5 W/m^2/K, the soil and the atmosphere become thermally uncoupled, as the soil does not warm very much (small ground heat flux) while the mixed-layer keeps growing and warming (positive sensible heat flux). This is also what is observed at the CESAR site (panel (c)).

The fact that a small value for Λ_{skin} better models the soil/atmosphere coupling is not consistent with the diagnosed value of 15 W/m^2/K in chapter 4 for summer daytime (figure 4.11). This inconsistency between different "optimal" values of Λ_{skin} for the CESAR site (15 W/m^2/K in figure 4.11 and 5 W/m^2/K in figure 6.7) can be explained by two arguments : (1) the presence of an additional term in the surface energy balance (e.g photosynthesis) that reduces the

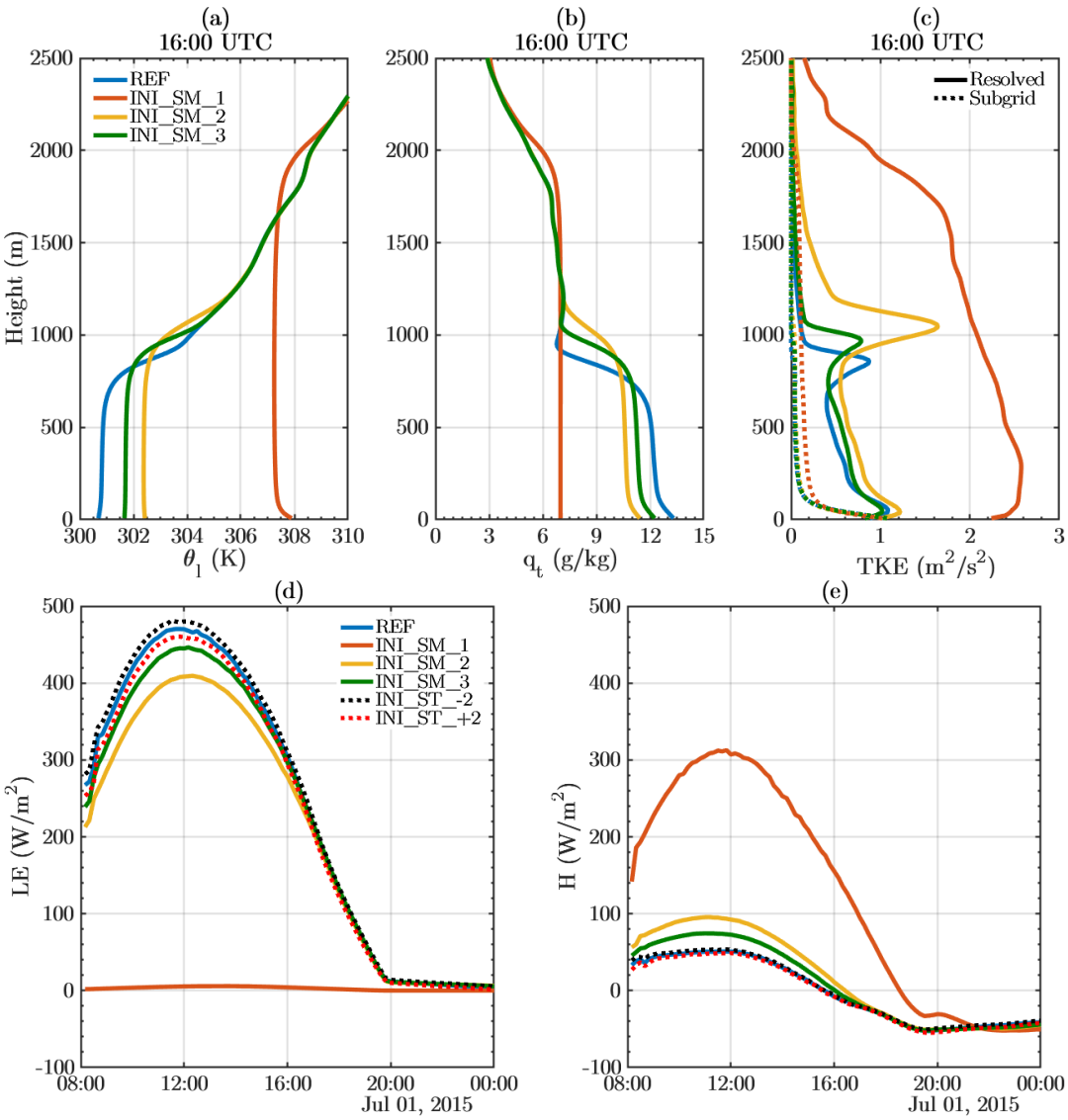

Figure 6.6: Top panels: Modelled vertical profiles of (a) liquid water potential temperature, (b) total specific humidity (c) turbulent kinetic energy at the CESAR site on 01/07/2015 at 16:00 UTC for different initial soil moisture profiles. Bottom panel: Observed (dashed lines) and modelled (thick lines) (d) surface latent heat flux and (e) surface sensible heat flux at the CESAR site on 01/07/2015 for different soil moisture and soil temperature profiles.

magnitude of the ground heat flux or (2) the dampening of the soil temperature fluctuations with depth due to thermal diffusion. The latter hypothesis is explained im more detail in Appendix G.

6.3. Radiation fog case

6.3.1. Case description

The final test of the fully coupled surface/radiation/LES model aims to model the formation, growth and dissipation of a radiation fog layer observed at the CESAR site during the night between 22/03/2011 and 23/03/2011, and summarised by Boers et al. (2013). Radiation fog (compared to advection fog, cloud base lowering fog,...) forms due to the radiative cooling of the air near the surface. Visibility observations at a height of 2m above the surface indicate that a very shallow fog layer was already present at 00:00 UTC. Both radar backscatter and visibility observations show that this fog layer started to deepen from 10m at 03:00 UTC to a maximum height of 150m at 06:00 UTC. After 08:00 UTC, the fog layer started evaporating and eventually completely disappeared at 09:00 UTC.

Previous modelling efforts for this particular case by Maronga and Bosveld (2017) suggest that the Radiation Fog development may be subdivided into three

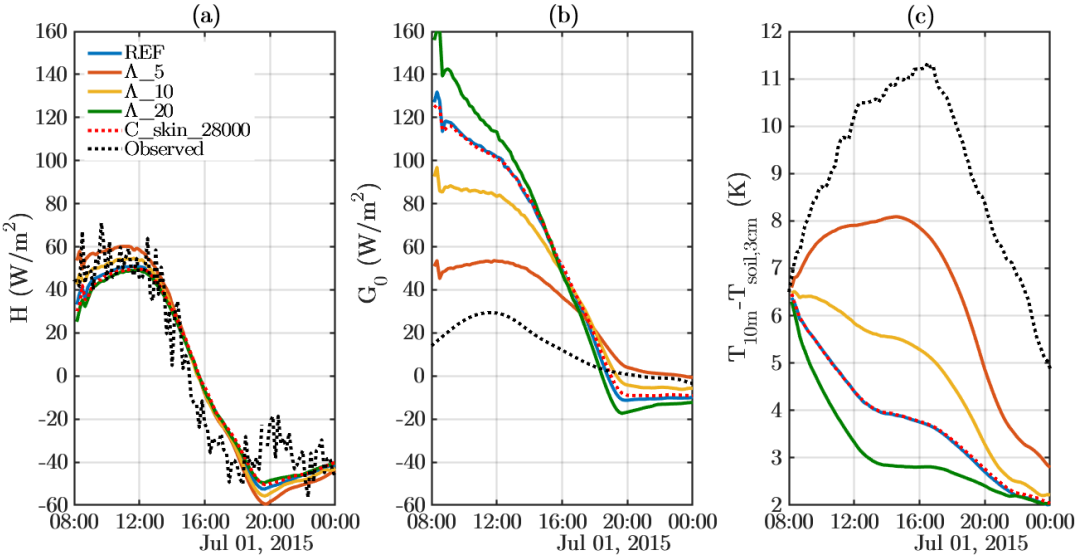

Figure 6.7: Modelled and observed (a) surface sensible heat flux, (b) ground heat flux and (c) temperature difference between the 10m atmospheric level and the 3cm soil level at the CESAR site on 01/07/2015 for different values of skin heat conductivity and skin volumetric heat capacity.

main stages:

- (1) Formation stage, when the air near the surface becomes saturated due to the isobaric longwave cooling of the surface and the net loss of heat and moisture from the air near the surface through negative (downward) turbulent fluxes.
- (2) Growth stage until mature fog maximum, mainly caused by longwave cooling at the fog top and by warming at the surface that drives convection and causes the formation of a shallow well-mixed layer.
- (3) Lifting and dissipation stage of the fog layer by the heating of the surface and of the fog layer itself by the absorption of incoming solar radiation.

Maronga and Bosveld (2017) have also shown that for this case, a spatial resolution of 4m in the three directions is sufficient for representing these main stages, hence this resolution will be used in the following experiments.

The land surface model has so far never been tested in a fully coupled mode in DALES for modelling radiation fog. The main objective of the following experiments is to assess whether this model can be used for fog simulations, and to understand what are the main challenges are for realistically modelling important fog parameters (formation time, maximum height, dissipation time). It will also be investigated whether the regional atmospheric model RACMO can be used to initialise and force DALES for such applications.

The experiments are summarised in table 6.4. Each simulation is initialised on 23/03/2011 at 00:00 UTC at the CESAR site, and executed until 12:00 UTC. The REF simulation uses the optimal land surface parameters derived in Chapter 4 for the CESAR site in March and summarised in Appendix C. A leaf area index of 2.5 m^2/m^2 is used, based on the Ecoclimap database and on PROBA-V satellite estimates (figure 4.6), and the roughness lengths for momentum and heat are set to 0.05m and 7.812×10^{-6}m respectively, which corresponds to the average observed values during winter at the CESAR site by Beljaars and Holtslag (1991) (figure 4.8). The surface albedo is set to 0.23 (figure 4.9) and the skin heat capacity is set to 7 W/m^2/s (figure 4.11).

Unless stted otherwise, the initial profiles of the liquid water potential temperature, the total specific humidity and the wind vector are taken from tower observations at 00:00 UTC, up to a height of 200m. Radiosonde observations at 00:00 UTC from the KNMI at De Bilt are used above 200m up to the maximum height of 400m . The initialisation and large scale forcing are shown in figure E.3.

6.3.2. Tower & radiosonde initialisation

The modelled slab-averaged liquid water specific humidity for the REF and ADV_on simulations is shown in figure 6.8. In the REF simulation, the fog starts to

Name	Initialisation	Comments
REF	CESAR tower & De Bilt radiosonde	REF parameters & no large-scale advection
ADV_on	CESAR tower & De Bilt radiosonde	REF parameters & large-scale advectio from RACMO
INIT_RACMO	RACMO	REF parameters & large-scale advection from RACMO

Table 6.4: List of Radiation fog experiments

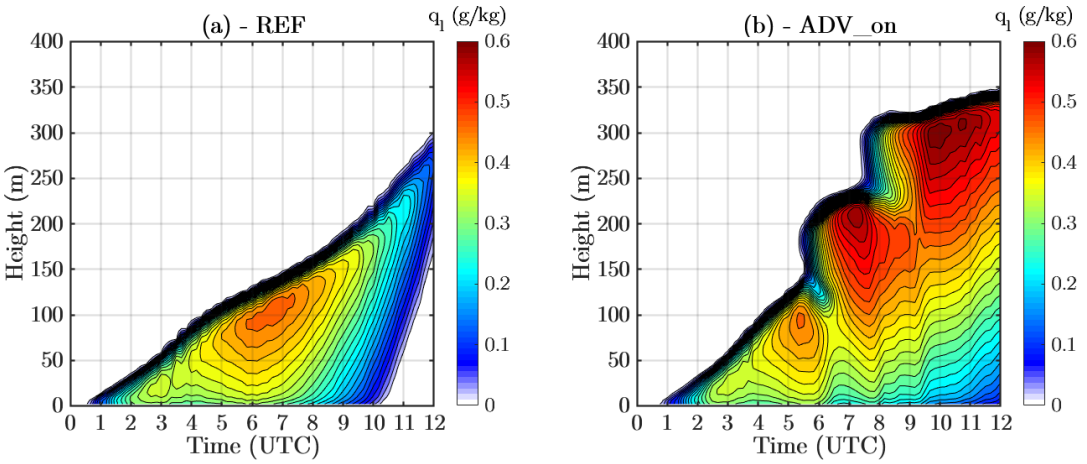

Figure 6.8: Modelled liquid water specific humidity at the CESAR site on 23/03/2011 for (a) the REF simulation and (b) the ADV_on simulation.

form at 00:30 UTC and grows up to 300m at 12:00 UTC. However for the ADV_on simulation, the fog forms slightly later, at 01:00 UTC and grows until 350m at 12:00 UTC. For the REF simulation, the maximum liquid water mixing ratio is reached between 06:00 and 07:00 UTC, while in the ADV_on simulation it reaches a maximum at 10:00 UTC. In the ADV_on simulation, second and third fog layers appear on top of the first layer at 170m at around 5:30 UTC and at 300m at 7:30 UTC.

The formation of multiple fog layers can be explained by looking at the vertical profiles of liquid water potential temperature, total specific humidity and relative humidity in figure 6.9. The large-scale advection prescribed by RACMO (figure E.3) brings both cold and humid air into the simulation, which increases the relative humidity and brings it to saturation between 05:00 and 06:00 UTC at a height of 170m, and between 07:00 and 08:00 UTC at 300m (panel (f)). In reality, the fog did not grow this high, which is a strong indication that the large-scale advection of cold air (of ≈ -0.3K/hour, see figure E.3) is overestimated in RACMO. This is verified by the radiosonde observations and the tower observations at 200m (6.11), that show hardly any any cooling between 00:00 to 12:00 UTC.

The modelled fog layers in the REF and ADV_on experiments are well-mixed in liquid water potential temperature and specific humidity, and exhibit a thermal inversion at the fog top that separates the colder air in the fog layer from the warm air on top of it. Comparison with both tower and radiosonde observations reveals that the fog layers persist for quite long, which keeps the temperatures at 279K at 12:00 UTC, while both the radiosonde measurements (figure 6.9 and tower measurements (figure 6.11) indicate mixed-layer temperatures of more than 281K at 12:00 UTC.

The components of the surface energy balance and surface radiation for the REF simulation are shown in figure 6.10. At 02:00 UTC, the fog layer is 40m thick and becomes opaque for longwave radiation (panel (a)), hence it starts emitting more than 300 W/m^2 of longwave radiation in both directions, while it receives less than 270 W/m^2 from the atmosphere above (panel (a) & (b)). This results in a significant radiative loss, which cools the air at the fog top, hence decreases it's buoyancy and drives top-down convection that is visible in the vertical profile of the slab averaged turbulent kinetic energy (panel (c)). The turbulent kinetic energy shows a peak at the inversion height, and only increases from the bottom during the modelled dissipation stage, after 10:00 UTC. The modelled and observed downward longwave radiation reveals that the modelled fog layer actually becomes opaque too early, at around 02:00, while surface observations show a maximum downwelling

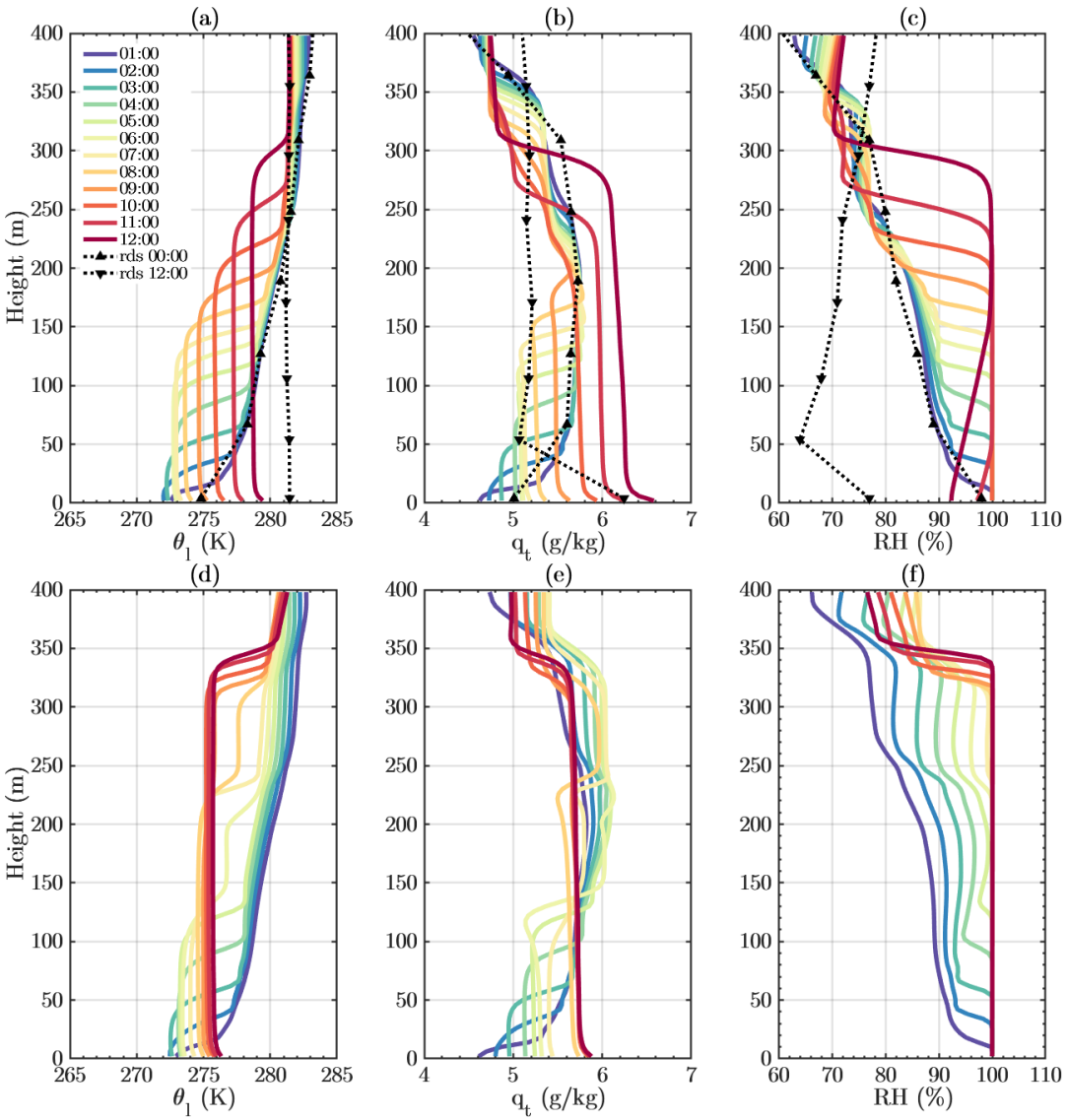

Figure 6.9: Modelled vertical profiles of (a) & (d) liquid water potential temperature, (b) & (e) total specific humidity and (c) & (f) relative humidity at the CESAR site on 23/03/2011. Top panels (a) & (b) & (c) are results from the REF simulation, and bottom panels (d) & (e) & (f) are results from the ADV_on simulation. Radiosonde observations from De Bilt on 00:00 and 12:00 UTC are shown on the top panels.

longwave radiation only at 03:30 (panel (e)). This is a direct consequence of the modelled fog layer that is already too thick at 02:00 compared to visibility and radar backscatter measurements. Yet the upward longwave radiation is accurate within 10 W/m^2, which means that the net radiation loss by the surface is actually underestimated in the first hours of the simulation (panel (d)), so the longwave radiation components do not explain why the fog forms too early.

A possible explanation for later fog formation in the REF simulation compared to the observations is the presence of low-level warm or dry air advection, already suggested by RACMO (figure E.3, but that is not present in the REF simulation. A different possibility is either the overestimation of the downward turbulent surface fluxes, possibly due to a too coarse spatial resolution and too high roughness lengths, or a too cold and wet initialisation, which was found by Maronga and Bosveld (2017). It is most likely that these two effects are both present in our LES results, but they have not been investigated, as they are outside the scope of this study.

As the fog layer keeps growing, the surface net absorbed longwave radiation hardly changes and even becomes slightly positive, which translates in small positive surface sensible and latent heat fluxes, that warm up and moisten the fog layer from below and enhance convection. At sunrise (around 06:00 UTC), the fog layer has grown up to 130m, which is con-

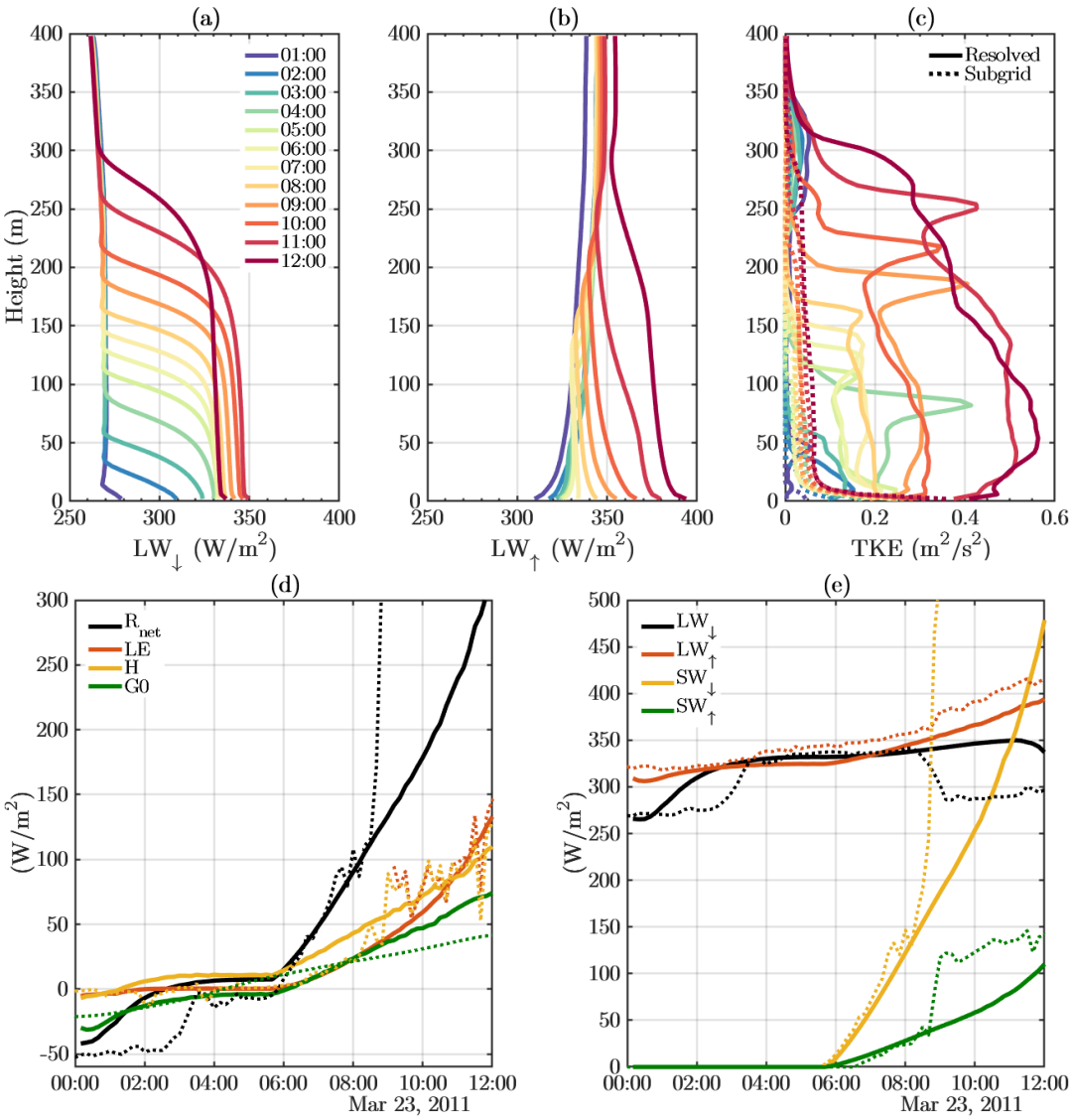

Figure 6.10: Top panels: Modelled vertical profiles of (a) downwelling longwave radiation, (b) upwelling longwave radiation, (c) turbulent kinetic energy at the CESAR site on 23/03/2011 for the REF simulation. Bottom panels: Temporal evolution of the modelled (thick lines) and observed (dashed lines) (d) surface energy balance and (e) surface at the CESAR site on 23/03/2011 for the REF simulation.

sistent with radar backscatter measurements from Boers et al. (2013). Furthermore, the amount of incoming shortwave radiation at the surface is modelled with great accuracy until 08:00 UTC (panel (e)). However after 08:00, the modelled fog layer persists for too long and even grows up to 200m, which explains the underestimation of the available radiation at the surface (figure 6.10, panel (d)). Most interestingly, the comparison of the REF simulation results with the tower measurements (figure 6.11) reveals that the potential temperature and specific humidity tendencies are similar during the fog dissipation stage, but delayed by almost 2 hours in the REF simulation compared to the tower observations.

6.3.3. RACMO initialisation

The fog layer modelled by the INIT_RACMO simulation, which only uses information from large-scale model RACMO for the initialisation, is shown in figure 6.12.

The modelled fog layer appears slightly later than in the REF simulation, at 01:30 UTC and grows up to a height of 300m height at 12:00 UTC. Just like in the REF and ADV_on simulations, the dissipation after sunrise is strongly underestimated, which causes the fog layer to grow too much until the end of the simulation.

Vertical profiles for the RACMO_init simulation can be found in figure 6.13. The well-mixed fog layer grows slightly higher and colder than in the REF sim-

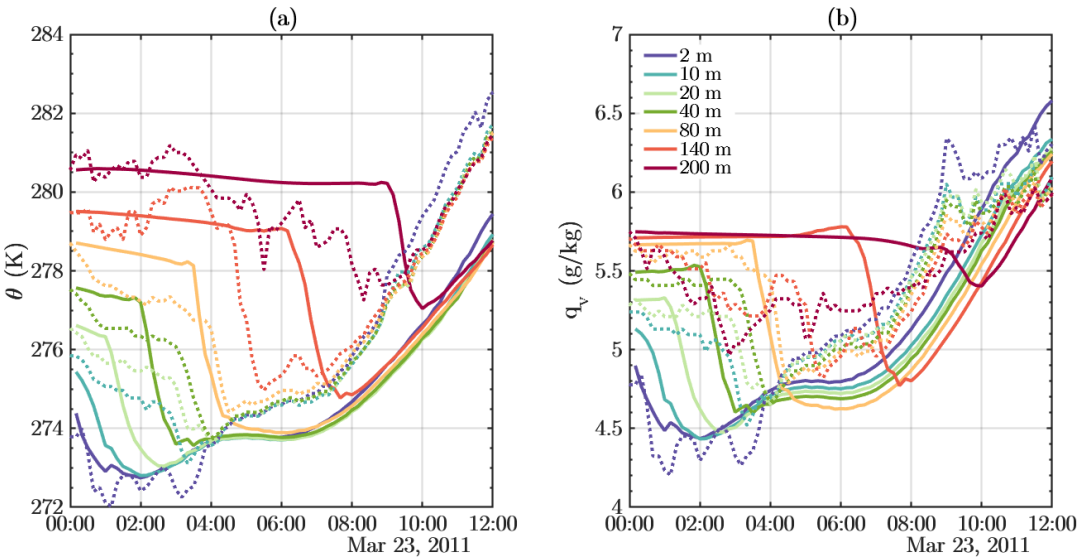

Figure 6.11: Modelled (thick lines) and observed (dashed lines) (a) potential temperature and (b) water vapour specific humidity at different heights, at the CESAR site, for the REF simulation during the fog event on 23/03/2011.

ulation (figure 6.9). Although large-scale horizontal advection of potential temperature and total specific humidity is prescribed in this simulation, there is no formation of secondary fog layers. This is due to the fact that the initial potential temperature profiles are very similar but the initial total specific humidity is drier in the INIT_RACMO simulation (panel (b)).

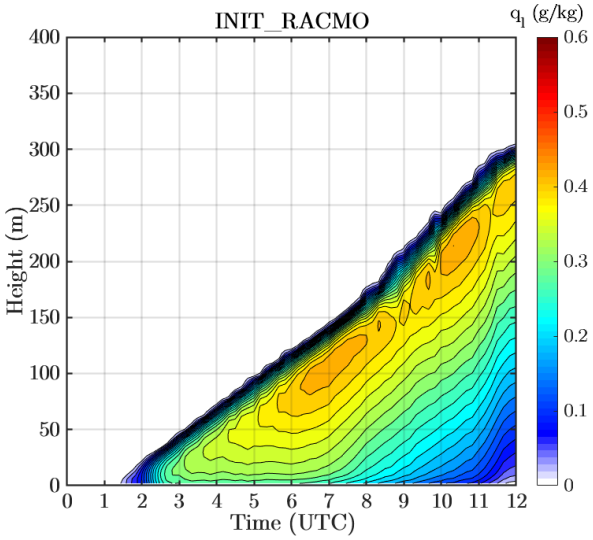

Figure 6.12: Modelled liquid water specific humidity at the CESAR site on 23/03/2011 for the INIT_RACMO simulation.

The differences between DALES results and RACMO results are very similar to the differences of the REF simulation with radiosonde observations. The modelled fog in the INIT_RACMO simulation becomes too thick, which means that the mixed layer is too cold at the end of the simulation. It must be noted that RACMO predicts the formation of a fog layer of approximately 110m thickness between 22/03/2011 at 19:00 UTC and 23/03/2011 at 10:00 UTC (not shown). The fog layer disappeared after 10:00 UTC in RACMO, hence the RACMO temperatures at the end of the simulation are warmer and much closer to the observations then our LES results.

6.4. Summary and discussion

In this chapter, the land surface model was tested for three very different situations that fully coupled the radiation, the microphysics and the atmospheric LES models. These experiments allowed the calculated surface fluxes and surface temperature to be routed back to the atmosphere and the ground.

It was found that the land surface model is able to accurately model the surface turbulent fluxes of temperature (sensible heat) and moisture (latent heat), and that for many cases, the use of a 'good' land surface parameter set, specifically derived for the CESAR site gives slightly better results than the use of a 'first guess' parameter set taken from the ECMWF look-up table for the short grass class.

The inclusion of an interactive land surface into the evolution of the atmosphere facilitates the study of the sensitivity of stratocomulus development on microphysical properties that affect both radiation and precipitation.
Furthermore, it was found that an increased water stress increases the growth rate of the convective boundary layer. This partly explains partly why erroneous surface parametrizations can produce strong biases in near-surface air temperature forecasts during dry summer periods.

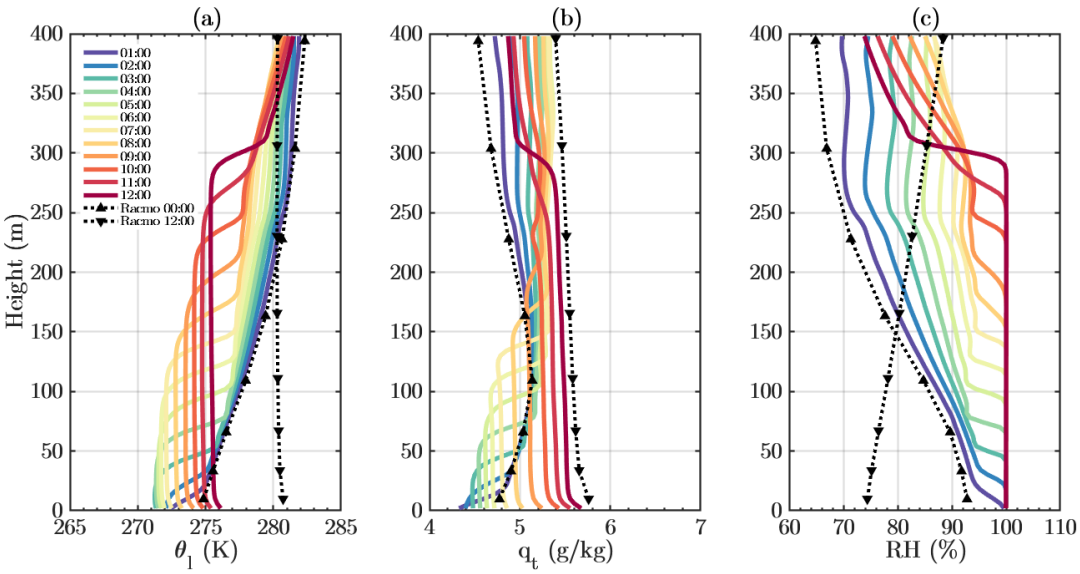

Figure 6.13: Modelled vertical profiles of (a) liquid water potential temperature, (b) total specific humidity and (c) relative humidity at the CESAR site on 23/03/2011 for the INIT_RACMO simulation. Output from the RACMO model in forecasting mode is represented by the back lines.

Finally, the coupled model was found to be able to model the main stages of radiation fog, although the fog layer appears to be too persistent in DALES.

Fully coupled LES-land surface simulations offer great opportunities in the modelling of the atmospheric boundary layer. They do not greatly increase computation time but offer the possibility to allow the land surface to freely evolve in time. Furthermore, a lot of literature and new remote sensing observations are available concerning the values of the land surface parameters, and their influence on the calculated surface fluxes. This directly reduces the model uncertainty related to the land surface parameters, which is one of the main challenges that come with using land surface models.
However, for forecasting purposes, it was found that the effect of large-scale advection is also critical, hence more research is needed to provide an accurate large-scale forcing to the LSM-LES model. For instance, the large-scale motion taken from regional or global models, could be validated against measurements from multiple observatories close to each other.
Finally, the land surface model in DALES still needs to be improved, both concerning the soil water transfer, which is in fact rather complex at the CESAR site, and concerning the assumption of a single skin layer that aims to represent the coupling between the subsurface (soil) and the atmosphere. It appears questionable whether this approach is well suited to model heat transfer in a vegetation canopy, especially during warm and clear summer days.

7

Final conclusion and suggestions

In order to calculate the surface fluxes over land, the turbulence-resolving Dutch Atmospheric Large-Eddy Simulation (DALES) model uses a land surface model (LSM) that is very similar to the H-TESSEL land surface model from the European Centre for Medium-Range Weather Forecasts (ECMWF, 2017). It is slightly simpler, as it does not include any snow, ice or inland-water (lake) parametrization, and each grid-box can only contain vegetation, liquid water on top of the vegetation or bare soil. Furthermore, the soil is homogeneous in DALES, and the horizontal surface water runoff is not routed to the adjacent grid boxes, but permanently leaves the model domain.

The surface energy balance determines the partitioning of the net radiation absorbed by the surface into surface turbulent fluxes of temperature (sensible heat), moisture (latent heat) towards the atmosphere, and into the heat flux towards the soil. The redistribution of the absorbed radiation strongly depends on the state of the soil (soil water and temperature), of the vegetation (vegetation density, height, vegetation stress) and of the atmosphere (stability, wind speed). The land surface models calculates the soil temperature and the soil moisture at each time-step by numerically solving the vertical diffusion equations of heat and water across a homogeneous soil column dicretised in four layers. The model uses a prescribed temperature and a prescribed water flux at the soil bottom.

The land surface model in DALES was modified in order to allow for physically realistic yearly offline simulations. Some major modifications include the routing of precipitation towards the soil through vegetation interception, surface runoff and infiltration. The parametrization of the root-water extraction and the vegetation stress was changed from the ECMWF-TESSEL version to the SURFEX- ISBA-DIF version (Le Moigne et al., 2009). Finally, the possibility to use the van Genuchten parametrization for the soil hydraulic functions was added.

The modification of the land surface model than enabled us to answer the following research questions:

- *How well does the LSM in DALES model the surface fluxes at the CESAR observatory?*

The yearly offline validation of the DALES-land surface model at the Cabauw Experimental Site for Atmospheric Research (CESAR) during 2015 revealed that DALES is capable of modelling the surface latent heat and sensible heat fluxes with an overall accuracy of 10 W/m^2. The accuracy declines to more than 20 W/m^2 for runs that extend for more than 6 months in time, mainly due to the overestimation of soil water loss and the subsequent overestimation of vegetation water stress.

- *What are the important land surface parameters, and how accurate are their default values?*

Offline sensitivity experiments of the land surface model reveal that the Leaf Area Index (LAI) and the minimal vegetation canopy resistance ($r_{s,\mathrm{veg_{min}}}$) both act as scaling parameters on the surface fluxes, hence making them especially critical when the net absorbed radiation at the surface is important, e.g during day-time summer. The roughness lengths for heat and momentum do not greatly affect the monthly variations of the surface fluxes, but are particularly critical for modelling the turbulent fluxes during night-time. The skin layer heat conductivity has a very important influence on the surface temperature during night-time. Finally the vertical root profiles are only important when the soil water content drops below field capacity, which was found to happen only during short periods in summer, and only in the first 50cm of the soil column, at the CESAR observatory.

- *How do coupled LES-land surface results compare to observations at the CESAR observatory?*

The land surface model in DALES is able to model the diurnal evolution and the magnitude of the surface fluxes with great accuracy (10 W/m^2), in an online mod . This translates, for the stratocumulus case, in a more accurate description of the cloud liquid water path (within 0.02 kg/m^2). However, a small mismatch in the radiation components is still present, which propagates in the surface flux calculations.

For the clear convective boundary layer case, the latent heat flux is overestimated by 50 W/m^2 ($\approx$ 15% of the observed total), but the radiation components and the sensible heat flux are modelled with very high accuracy. The growth of the boundary layer was found to be strongly dependent on the magnitude of the sensible heat flux, which is highly controlled by the amount of soil moisture. Although the modelled sensible heat flux was found to be very accurate, the warming and the growth of the mixed-layer were still found to be substantially underestimated, compared to observations.

Finally, for the radiation fog case, it was found that DALES with the coupled LSM is able to model important features for the representation of radiation fog, such as formation time, lifting of the fog layer and dissipation. The modelled fog layer was found to be strongly sensitive to the initial profiles and to the large-scale forcing.

Final word

DALES demonstrates a very high accuracy in modelling the land surface, the atmospheric radiation transfer, the turbulent mixing and the microphysical cloud processes, simultaneously. However, for an operational use of DALES as a weather forecast model, some important modifications are still necessary:

Firstly, offline simulations have revealed that the lower boundary conditions for soil water transfer is not well suited, as the amount of water leaving the model at the bottom is greatly overestimated. At the CESAR observatory, complex water-table interactions and artificial surface management take place, which means that the surface water balance and soil water transfer equations need to be revised.

Secondly, additional parametrizations of snow, frozen ground, in-land water bodies and urban areas is required in order to be able to use DALES for extended areas. It is also worth mentioning that the single skin layer approach was found to not be well suited for representing the coupling between the soil and the atmosphere, especially during summer and during day-night transitions.

Finally, our LES simulations compared to observations from the CESAR observatory suggest that the 'true' boundary layer evolution in time is also strongly affected by large-scale advection that is not resolved by the smaller domain in DALES. The 'best' option at this time is to use the regional model RACMO (or other regional models, such as the KNMI operational model *Harmonie* (Bengtsson et al., 2017)) to provide the large-scale forcing to DALES. However, we found that the large-scale horizontal advection from RACMO is not always consistent with the observed tendencies at the CESAR observatory. Hence additional validation of larger scale motion in the regional models is necessary. Atmospheric modelling is truly a multidisciplinary and multiscale puzzle, and efforts in accurately modelling small-scale physical processes (in this case, the land surface) only constitute a modest, but necessary, part of the progress in this field.

A Surface energy balance solver

The calculation of the surface fluxes requires solving the surface energy balance for the skin temperature at the next timestep, which is unknown. Solving the SEB for the skin temperature is not straightforward due to the non-linear dependence of the upwelling longwave radiation and saturation specific humidity on temperature. In this model these non-linear relationships are linearized in time with respect to the skin temperature.

The surface energy balance (SEB) at the next time index $t+1$ is written:

$$Q_{net}^{t+1} - H^{t+1} - LE^{t+1} - G_0^{t+1} = 0 \tag{A.1}$$

where the net available radiation at the surface is defined as:

$$Q_{net}^{t+1} = SW_{\downarrow}^{t+1} - SW_{\uparrow}^{t+1} + LW_{\downarrow}^{t+1} - LW_{\uparrow}^{t+1} \tag{A.2}$$

Each component of the SEB may be rewritten using the skin temperature T_s or the skin potential temperature θ_s:

$$\begin{aligned} LW_{\uparrow}^{t+1} &= \epsilon\sigma\left(T_s^{t+1}\right)^4 \\ H^{t+1} &= f_H\left(\theta_s^{t+1} - \theta_0\right) \\ LE^{t+1} &= f_{LE}\left(q_{\text{sat}}(T_s^{t+1}) - q_0\right) \\ G_0^{t+1} &= \Lambda_{\text{skin}}\left(T_s^{t+1} - T_{\text{soil},1}\right) \end{aligned} \tag{A.3}$$

where:

$$\begin{aligned} f_{LE} = (1-c_{\text{veg}})\frac{\rho_a L_v}{r_{aq}+r_{s,\text{soil}}} + \\ (1-c_{\text{liq}})c_{\text{veg}}\frac{\rho_a L_v}{r_{aq}+r_{c,\text{veg}}} + \\ c_{\text{veg}}c_{\text{liq}}\frac{\rho_a L_v}{r_{aq}} \\ f_H = \frac{\rho_a C_p}{r_{ah}} \end{aligned} \tag{A.4}$$

The dependence of the net radiation on the surface temperature is removed:

$$Q_{net}^{t+1\,*} \equiv Q_{net}^{t+1} + LW_{\uparrow}^{t} \tag{A.5}$$

The linearization of the upwelling longwave radiation yields:

$$\begin{aligned} LW_{\uparrow}^{t+1} &= \epsilon\sigma {T_s^{t+1}}^4 \\ &\approx \epsilon\sigma {T_s^t}^4 + 4\epsilon\sigma {T_s^t}^3\left(T_s^{t+1} - T_s^t\right) \end{aligned} \tag{A.6}$$

And the linearization of the saturation specific humidity yields:

$$q_{sat}(T_s^{t+1}) \approx q_{sat}(T_s^t) + \left(\frac{\partial q_{sat}}{\partial T}\right)_{T_s^t}\left(T_s^{t+1} - T_s^t\right) \tag{A.7}$$

The potential temperature at the surface is defined as:

$$\theta_s \equiv \left(\frac{p_0}{p_s}\right)^{\frac{Rd}{Cp}} T_s \equiv \Pi T_s \tag{A.8}$$

where $p_0 = 10^5$ Pa, p_s is the atmospheric pressure at the surface and Π is the exner function defined as:

$$\Pi \equiv \left(\frac{p_0}{p_s}\right)^{\frac{Rd}{Cp}} \tag{A.9}$$

It is assumed that the near-surface temperature and potential temperature differences are similar:

$$\theta_s - \theta_0 \approx T_s - T_0 \tag{A.10}$$

This means that the sensible heat flux can be rewritten using the skin temperature:

$$H^{t+1} \approx f_H\left(T_s^{t+1} - T_0\right) \tag{A.11}$$

Combining all the expressions in the SEB gives the following expression:

$$\begin{aligned} Q_{net}^{t+1\,*} - \epsilon\sigma {T_s^t}^4 - 4\epsilon\sigma {T_s^t}^3\left(T_s^{t+1} - T_s^t\right) \\ - f_H\left(T_s^{t+1} - T_0\right) \\ - f_{LE}\left(q_{sat}(T_s^t) + \left(\frac{\partial q_{sat}}{\partial T}\right)_{T_s^t}\left(T_s^{t+1} - T_s^t\right) - q_0\right) \\ - \Lambda_{\text{skin}}\left(T_s^{t+1} - T_{\text{soil},1}\right) = 0 \end{aligned} \tag{A.12}$$

This may be rewritten in a simple form:

$$T_s^{t+1} = \frac{A}{B} \tag{A.13}$$

where:

$$\begin{aligned} A = Q_{net}^{t+1\,*} - \epsilon\sigma {T_s^t}^4 + 4\epsilon\sigma {T_s^t}^4 + f_H T_0 \\ + f_{LE}\left(\left(\frac{\partial q_{sat}}{\partial T}\right)_{T_s^t} T_s^t - q_{sat}(T_s^t) + q_0\right) \\ + \Lambda_{\text{skin}} T_{\text{soil},1} \end{aligned} \tag{A.14}$$

$$B = 4\epsilon\sigma {T_s^t}^3 + f_H + f_{LE}\left(\frac{\partial q_{sat}}{\partial T}\right)_{T_s^t} + \Lambda_{\text{skin}}$$

The saturation water vapour pressure can be expressed using an approximate form of the Clausius-Clapeyron formula (Stull, 1988, chap. 7):

$$e_{sat} = 610.78 \exp\left(17.2694\left(\frac{T-273.16}{T-35.86}\right)\right) \tag{A.15}$$

First order differentiation with respect to temperature yields:

$$\frac{\partial e_{sat}}{\partial T} = e_{sat}\left(\frac{17.2694}{T-35.86} - 17.2694\left(\frac{T-273.16}{(T-35.86)^2}\right)\right) \tag{A.16}$$

The specific humidity is then approximated as:

$$q_{sat} = 0.622\frac{e_{sat}}{p} \tag{A.17}$$

where p is the atmospheric pressure. The first derivative of the specific humidity with respect to temperature is approximated as:

$$\frac{\partial q_{sat}}{\partial T} = 0.622\frac{\partial e_{sat}}{\partial T}\frac{1}{p} \tag{A.18}$$

B

List of changes

The following changes have been implemented in DALES:

- Coupled precipitation from the microphysics module (*modmicrophysics.f90*) to the land surface module (*modsurface.f90*)
- Added infiltration of rainfall and surface runoff.
- Changed lower boundary condition for soil moisture transport (free drainage)
- Constrained soil hydraulic conductivity and diffusivity to a range of fixed realistic values.
- Constrained soil thermal conductivity to a range of fixed realistic values.
- Removed dew deposition on bare soil (which acted as a source of water in the first soil layer when evaporative flux is oriented downwards).
- Changed vegetation stress function $f_{2,\mathrm{veg}}$ from TESSEL version (ECMWF, 2017) to ISBA version (Le Moigne et al., 2009).
- Changed vegetation root water extraction from TESSEL version to ISBA version.
- Changed surface emissivity from 1 to 0.98 in the surface energy balance solver.
- Coupled surface temperature from the surface module (*modsurface.f90*) to the RRTMG radiation module (*modradrrtmg.f90*) for upwelling longwave radiation calculation at the surface.
- Added possibility to use van Genuchten (1980) parameterization for soil hydraulic functions (switch in namoptions).
- Added possibility to use different land types for albedo calculation as function of solar zenith angle in the RRTMG radiation module (in *modradrrtmg.f90*), based on Briegleb (1992).

The following modules in the source code have seen modifications:

- *modsurface.f90*
- *modsurfdata.f90*
- *modmicrodata.f90*
- *modradrrtmg.f90*
- *modraddata.f90*

C

List of parameters in the land surface model

Symbol	Parameter	**REF** (STRD) values for CESAR	Report section	Comments
Soil				
$\lambda_{T,\text{dry}}$	Dry thermal conductivity	**0.19** W/m/K	(2.1)	Increases with soil dry density
$\lambda_{T,\text{s}}$	Solids thermal conductivity	**3.44** W/m/K	(2.1)	Increases with quartz content
$\lambda_{T,\text{water}}$	Water thermal conductivity	**0.57** W/m/K	(2.1)	-
$(\rho C)_{\text{dry}}$	Volumetric dry heat capacity	$\mathbf{2.19 \times 10^6}$ J/m^3/K	(2.1)	-
$(\rho C)_{\text{water}}$	Volumetric water heat capacity	$\mathbf{4.20 \times 10^6}$ J/m^3/K	(2.1)	-
Ψ_{sat}	Clapp and Horberger pore pressure at saturation	**-0.338** m	(2.1)	USDA medium-texture soil
b	Clapp and Horberger parameter	**6.04**	(2.1)	USDA medium-texture soil
$\gamma_{h_{\text{sat}}}$	Hydraulic conductivity at saturation	$\mathbf{0.52 \times 10^{-6}}$ (0.57×10^{-6}) m/s	(2.1) & (3.4)	B11 texture from Wösten et al. (2001)
θ_{sat}	Porosity	**0.590**(0.472) m^3/m^3	(2.1) & (3.4)	B11 texture from Wösten et al. (2001)
θ_{fc}	Volumetric water content at field capacity	**0.528**(0.323) m^3/m^3	(2.2) & (3.4)	B11 texture from Wösten et al. (2001)
θ_{wp}	Volumetric water content at wilting point	**0.320**(0.171) m^3/m^3	(2.2) & (3.4)	B11 texture from Wösten et al. (2001)
θ_{r}	Residual volumetric water content	**0.010** m^3/m^3	(3.4)	B11 texture from Wösten et al. (2001)
α_{υ}	Van Genuchten pressure-head parameter	**1.95** m^{-1}	(3.4)	B11 texture from Wösten et al. (2001)
l	Van Genuchten pore connectivity parameter	**-5.90**	(3.4)	B11 texture from Wösten et al. (2001)
n	Van Genuchten pore-size distribution parameter	**1.11**	(3.4)	B11 texture from Wösten et al. (2001)
$T_{\text{soil,deep}}$	Deep soil temperature	**283.81** (283) K	(2.1) % (4.3)	13-year mean 50cm temperature
Vegetation				
LAI	Leaf Area Index	**(2 - 4)** (2) m^2/m^2	(2.2) & (4.3)	Maximum in late summer
z_{0m}	Roughness length for momentum	($\mathbf{1 \times 10^{-2} - 15 \times 10^{-2}}$) (0.2) m	(2.3) & (4.3)	Season and wind direction dependent
z_{0h}	Roughness length for heat	$\mathbf{z_{0m}}$/($\mathbf{6.4 \times 10^3}$) (0.002 m)	(2.3) & (4.3)	Best fit for CESAR observations
α	Surface shortwave albedo	**(0.21 - 0.33)**	(2.2) & (4.3)	Function of solar zenith angle
ϵ	Surface emissivity	**0.98**	(2.2) & (4.3)	Typical value for dry green grass
R_k	Root fraction in the k$^{\text{th}}$ layer	**0.4, 0.3, 0.3, 0.0** (0.35, 0.38, 0.23, 0.04)	(2.2) & (4.3)	Measurements for *Lollium Perenne*
Λ_{skin}	Skin heat conductivity	**(5 - 20)** (10) W/m^2/K	(2.2) & (4.3)	Non-linear function of stability
c_{veg}	Fractional vegetation cover	**1.0**	(2.2) & (4.3)	-
$r_{s,\text{veg}_{\text{min}}}$	Minimum vegetation stomatal resistance	**110** s/m	(2.2) & (4.3)	-
$r_{s,\text{soil}_{\text{min}}}$	Minimum bare soil surface resistance	**50** s/m	(2.2) & (4.3)	-
g_D	Parameter for atmospheric water vapour deficit	**0** Pa^{-1}	(2.2)	-
C_{skin}	Skin heat capacity	**0** J/m^2/K	/	Not used
Discretization				
k_{max}	Amount of soil layers	**4**	(2.1)	ECMWF configuration
D_k	Thickness of k$^{\text{th}}$ layer	**0.07, 0.21, 0.72, 1.89** m	(2.1)	ECMWF configuration

Table C.1: Typical values (or range of values) for parameters used in the land surface model for the CESAR site. REF parameters are taken from ECMWF (2017).

D DALES Namoptions files

D.1. Sratocumulus case - 18/02/2011 - REF simulation

```
!/bin/bash
RUN
iexpnr = 030
lwarmstart = .false.
runtime = 43200
trestart = 7200
dtmax = 5
ladaptive = .true.
irandom = 43
randthl = 0.1
randqt = 2.5e-5
nsv = 2
/

DOMAIN
itot = 128
jtot = 128
kmax = 200

xsize = 6400.
ysize = 6400.

xlat = 52.
xlon = 5.
xday = 49.
xtime = 12.
/

PHYSICS
z0 = 0.04
ps = 101609.00
thls = 275.5792
lmoist = .true.
lcoriol = .true.
ltimedep = .true.
iradiation = 4.
timerad = 10
sw0 = 600.
/

DYNAMICS
llsadv = .false.
lqlnr = .true.
cu = -2.
cv = -4.
iadv_mom = 5
iadv_tke = 5
iadv_thl = 5
iadv_qt = 5
iadv_sv = 5
/

NAMSURFACE
isurf = 1
l_vg = .true.
z0mav = 4e-2
z0hav = 6.25e-6
Cskinav = 0
lambdaskinav = 10
rootfav = 0.40 0.30 0.30 0.00
albedoav = 0.27
Qnetav = 5
cvegav = 1
Wlav = 0
rsminav = 100
rssoilminav = 50
LAIav = 2
gDav = 0
tsoildeepav = 284.00
tsoilav = 277.0060 277.9071 278.7807 281.3903
phiwav = 0.5280 0.5280 0.5280 0.5280
gammasat = 0.52e-6
nvg = 1.10
Lvg = -5.90
alphavg = 1.95
phir = 0.01
phi = 0.590
phiwp = 0.320
phifc = 0.528
/

NAMMICROPHYSICS
imicro = 2
l_sb = .false.
l_rain = .true.
l_sedc = .true.
l_mur_cst = .false.
mur_cst = 0
Nc_0 = 100e6
sig_g = 1.2
/

NAMRADIATION
lCnstAlbedo = .false.
usero3 = .false.
co2factor = 1.
/

SUBGRID
ldelta = .false.
cm = 0.12
cn = 0.76
ch1 = 1.
ch2 = 2.
ce1 = 0.19
ce2 = 0.51
/

NAMRADSTAT
dtav = 60
timeav = 600.
lstat = .true.
/

NAMBUDGET
lbudget = .true.
dtav = 60.
timeav = 600.
/

    NAMCHECKSIM
tcheck = 6
/

NAMSAMPLING
dtav = 60
timeav = 600.
lsampcl = .false.
lsampco = .false.
lsampup = .false.
lsampbuup = .false.
lsampcldup = .false.
/

NAMTIMESTAT
ltimestat = .true.
dtav = 600
/

NAMCROSSSECTION
lcross = .false.
```

```
dtav = 600
/

NAMGENSTAT
lstat = .true.
dtav = 60
timeav = 600
/

NAMFIELDDUMP
lfielddump = .true.
dtav = 3600
/

NAMLSMCROSSSECTION
lcross = .true.
dtav = 3600
crossheight = 1
/

NAMSTATTEND
dtav = 60
ltend = .true.
timeav = 600.
/

NAMLSMSTAT
lstat = .true.
dtav = 60
timeav = 600.
/

NAMBULKMICROSTAT
lmicrostat = .true.
dtav = 60
timeav = 600.
/
```

D.2. Clear convective boundary layer case - 01/07/2015 - REF simulation

```
!/bin/bash
RUN
iexpnr = 019
lwarmstart = .false.
runtime = 57600
trestart = 7200
dtmax = 10
ladaptive = .true.
irandom = 43
randthl = 0.1
randqt = 2.5e-5
nsv = 2
/

DOMAIN
itot = 128
jtot = 128
kmax = 200

xsize = 6400.
ysize = 6400.

xlat = 52.
xlon = 5.
xday = 182.
xtime = 8.
/

PHYSICS
z0 = 0.15
ps = 101750.00
thls = 298.7476
lmoist = .true.
lcoriol = .true.
ltimedep = .true.
iradiation = 4.
timerad = 60
sw0 = 1368.
/

DYNAMICS
llsadv = .false.
lqlnr = .true.
cu = -2.
cv = -4.
iadv_mom = 5
iadv_tke = 5
iadv_thl = 5
iadv_qt = 5
iadv_sv = 5
/

NAMSURFACE
isurf = 1
l_vg = .true.
z0mav = 0.15
z0hav = 0.235e-4
Cskinav = 0
lambdaskinav = 15
rootfav = 0.40 0.30 0.30 0.00
albedoav = 0.23
Qnetav = 5
cvegav = 1
Wlav = 0
rsminav = 110
rssoilminav = 50
LAIav = 3.5
gDav = 0
tsoildeepav = 284
tsoilav = 290.5514 290.1910
288.2651 286.1326
phiwav = 0.528 0.528 0.528 0.528
gammasat = 0.52e-6
nvg = 1.11
Lvg = -5.90
alphavg = 1.95
phir = 0.01
phi = 0.590
phiwp = 0.320
phifc = 0.528
/

NAMMICROPHYSICS
imicro = 2
l_sb = .true.
l_rain = .true.
l_sedc = .true.
l_mur_cst = .false.
mur_cst = 0
Nc_0 = 100e6
sig_g = 1.2
/

NAMRADIATION
lCnstAlbedo = .true.
usero3 = .false.
co2factor = 1.
/

SUBGRID
ldelta = .false.
cm = 0.12
cn = 0.76
ch1 = 1.
ch2 = 2.
ce1 = 0.19
ce2 = 0.51
/

NAMRADSTAT
dtav = 60
timeav = 600.

lstat = .true.
/

NAMBUDGET
lbudget = .true.
dtav = 60.
timeav = 600.
/

NAMCHECKSIM
```

tcheck = 6
/

NAMSAMPLING
dtav = 60
timeav = 600.
lsampcl = .false.
lsampco = .false.
lsampup = .false.
lsampbuup = .false.
lsampcldup = .false.
/

NAMTIMESTAT
ltimestat = .true.
dtav = 600
/

NAMCROSSSECTION
lcross = .false.
dtav = 600
/

NAMGENSTAT
lstat = .true.
dtav = 60
timeav = 600
/

NAMFIELDDUMP
lfielddump = .true.
dtav = 3600
/

NAMLSMCROSSSECTION
lcross = .true.
dtav = 3600
crossheight = 1
/

NAMSTATTEND
dtav = 60
ltend = .true.
timeav = 600.
/

NAMLSMSTAT
lstat = .true.
dtav = 60
timeav = 600.
/

NAMBULKMICROSTAT
lmicrostat = .true.
dtav = 60
timeav = 600.
/

D.3. Radiation fog case - 23/03/2011 - REF simulation

!/bin/bash
RUN
iexpnr = 014
lwarmstart = .false.
runtime = 43200
trestart = 7200
dtmax = 5
ladaptive = .true.
irandom = 43
randthl = 0.1
randqt = 2.5e-5
nsv = 2
/

DOMAIN
itot = 64
jtot = 64
kmax = 100

xsize = 256.
ysize = 256.

xlat = 52.
xlon = 5.
xday = 82.
xtime = 0.
/

PHYSICS
z0 = 0.05
ps = 103990.00
thls = 272.7412
lmoist = .true.
lcoriol = .true.
ltimedep = .true.
iradiation = 4.
timerad = 10
sw0 = 1368.
/

DYNAMICS
llsadv = .false.
lqlnr = .true.
cu = -2.
cv = -4.
iadv_mom = 5
iadv_tke = 5
iadv_thl = 5
iadv_qt = 5
iadv_sv = 5
/

NAMSURFACE
isurf = 1
l_vg = .true.
z0mav = 0.05
z0hav = 7.8125e-06
Cskinav = 0
lambdaskinav = 7
rootfav = 0.40 0.30 0.30 0.00
albedoav = 0.23
Qnetav = 5
cvegav = 1
Wlav = 0
rsminav = 110
rssoilminav = 50
LAIav = 2.5
gDav = 0
tsoildeepav = 284
tsoilav = 279.2105 279.6421 279.3839 281.6919
phiwav = 0.528 0.528 0.528 0.528
gammasat = 0.52e-6
nvg = 1.10
Lvg = -5.90
alphavg = 1.95
phir = 0.01
phi = 0.590
phiwp = 0.320
phifc = 0.528
/

NAMMICROPHYSICS
imicro = 2
l_sb = .true.
l_rain = .true.
l_sedc = .true.
l_mur_cst = .false.
mur_cst = 0
Nc_0 = 150e6
sig_g = 1.2
/

NAMRADIATION
lCnstAlbedo = .true.
usero3 = .false.
co2factor = 1.
/

SUBGRID
ldelta = .false.
cm = 0.12
cn = 0.76

```
ch1 = 1.
ch2 = 2.
ce1 = 0.19
ce2 = 0.51
/

NAMRADSTAT
dtav = 60
timeav = 600.
lstat = .true.
/

NAMBUDGET
lbudget = .true.
dtav = 60.
timeav = 600.
/

NAMCHECKSIM
tcheck = 6
/

NAMSAMPLING
dtav = 60
timeav = 600.
lsampcl = .false.
lsampco = .false.
lsampup = .false.
lsampbuup = .false.
lsampcldup = .false.
/

NAMTIMESTAT
ltimestat = .true.
dtav = 600
/

NAMCROSSSECTION
lcross = .false.
dtav = 600
/

NAMGENSTAT
lstat = .true.
dtav = 60
timeav = 600
/

NAMFIELDDUMP
lfielddump = .true.
dtav = 3600
/

NAMLSMCROSSSECTION
lcross = .true.
dtav = 3600
crossheight = 1
/

NAMSTATTEND
dtav = 60
ltend = .true.
timeav = 600.
/

NAMLSMSTAT
lstat = .true.
dtav = 60
timeav = 600.
/

NAMBULKMICROSTAT
lmicrostat = .true.
dtav = 60
timeav = 600.
/
```

E

DALES initialisation and forcing

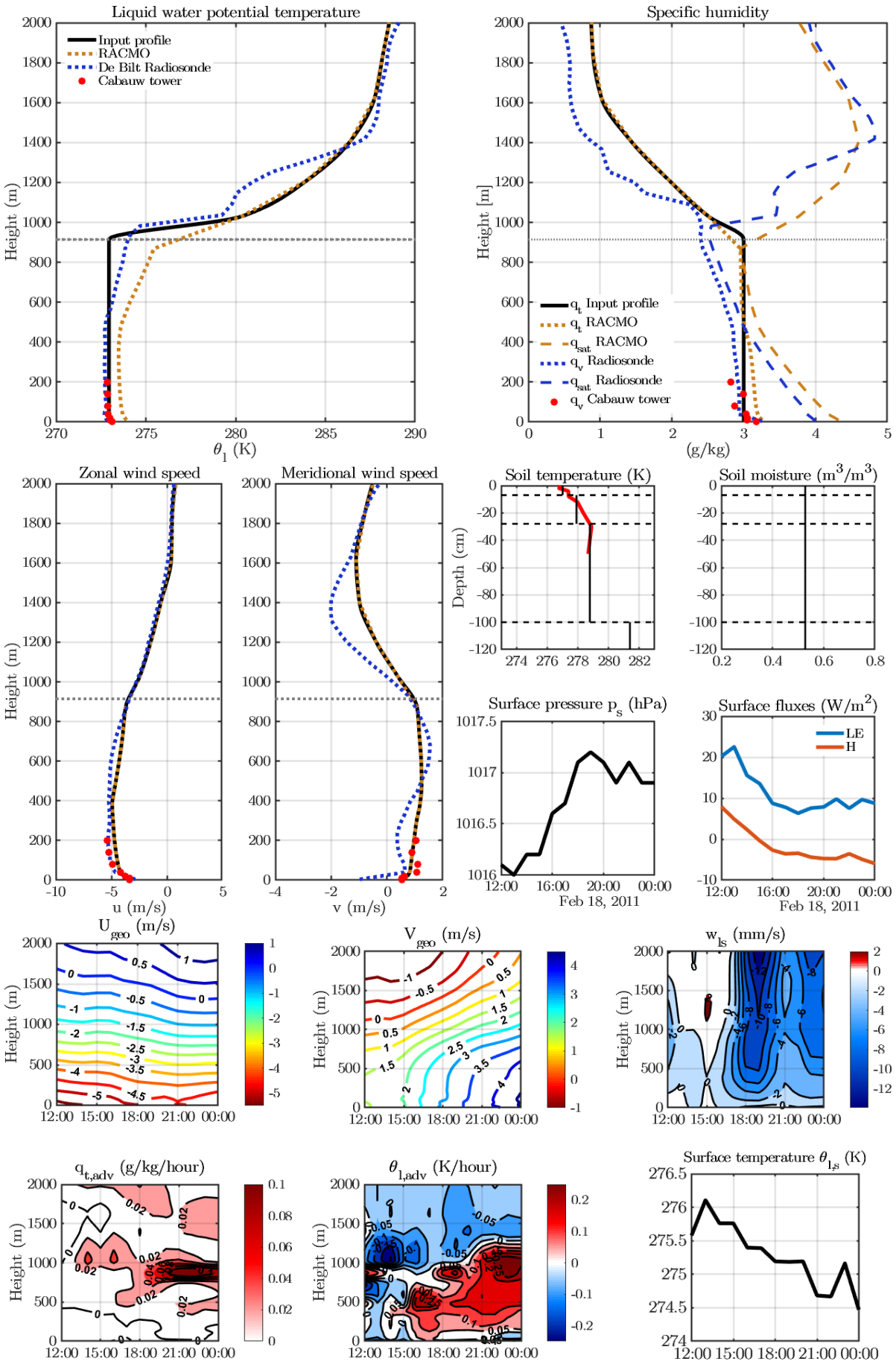

Figure E.1: Initial profiles for the sratocumulus case on 18 February 2011 at 12:00. Time is in UTC. The initial profiles of potential temperature, specific humidity and wind vectors are compared against tower measurements at Cabauw, radiosonde measurements from De Bilt and RACMO model data (top & middle-left panel). The estimated cloud top is denoted by the horizontal grey line. Initial soil temperatures and volumetric soil moisture are shown in the medium right panels. Bottom panels show the time-varying large-scale forcings taken from RACMO.

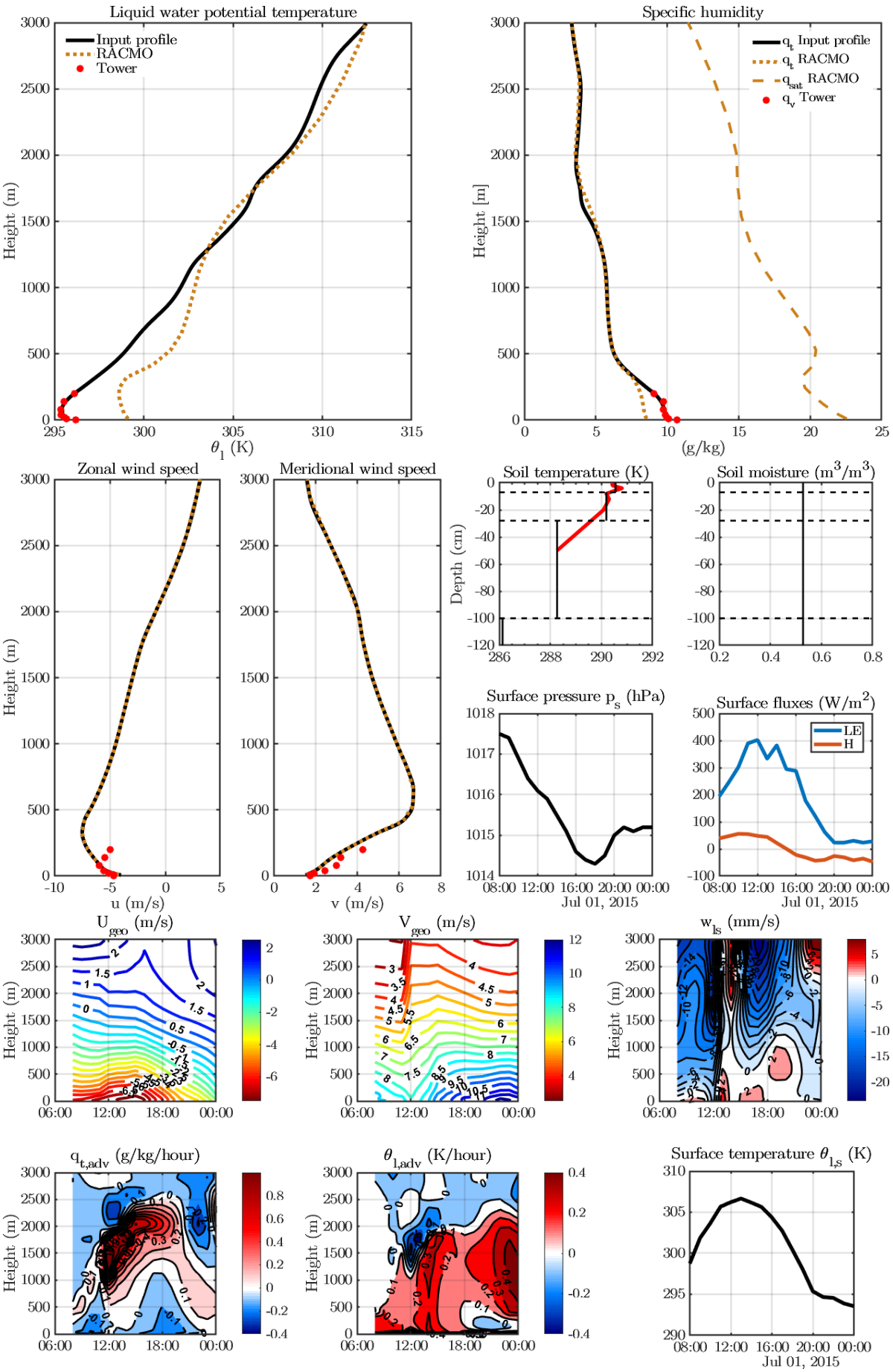

Figure E.2: Initial profiles for the convective boundary layer case on 01 July 2015 at 08:00. Time is in UTC. The initial profiles of potential temperature, specific humidity and wind vectors are compared against tower measurements at Cabauw, radiosonde measurements from De Bilt and RACMO model data (top & middle-left panel). Initial soil temperatures and volumetric soil moisture are shown in the medium right panels. Bottom panels show the time-varying large-scale forcings taken from RACMO.

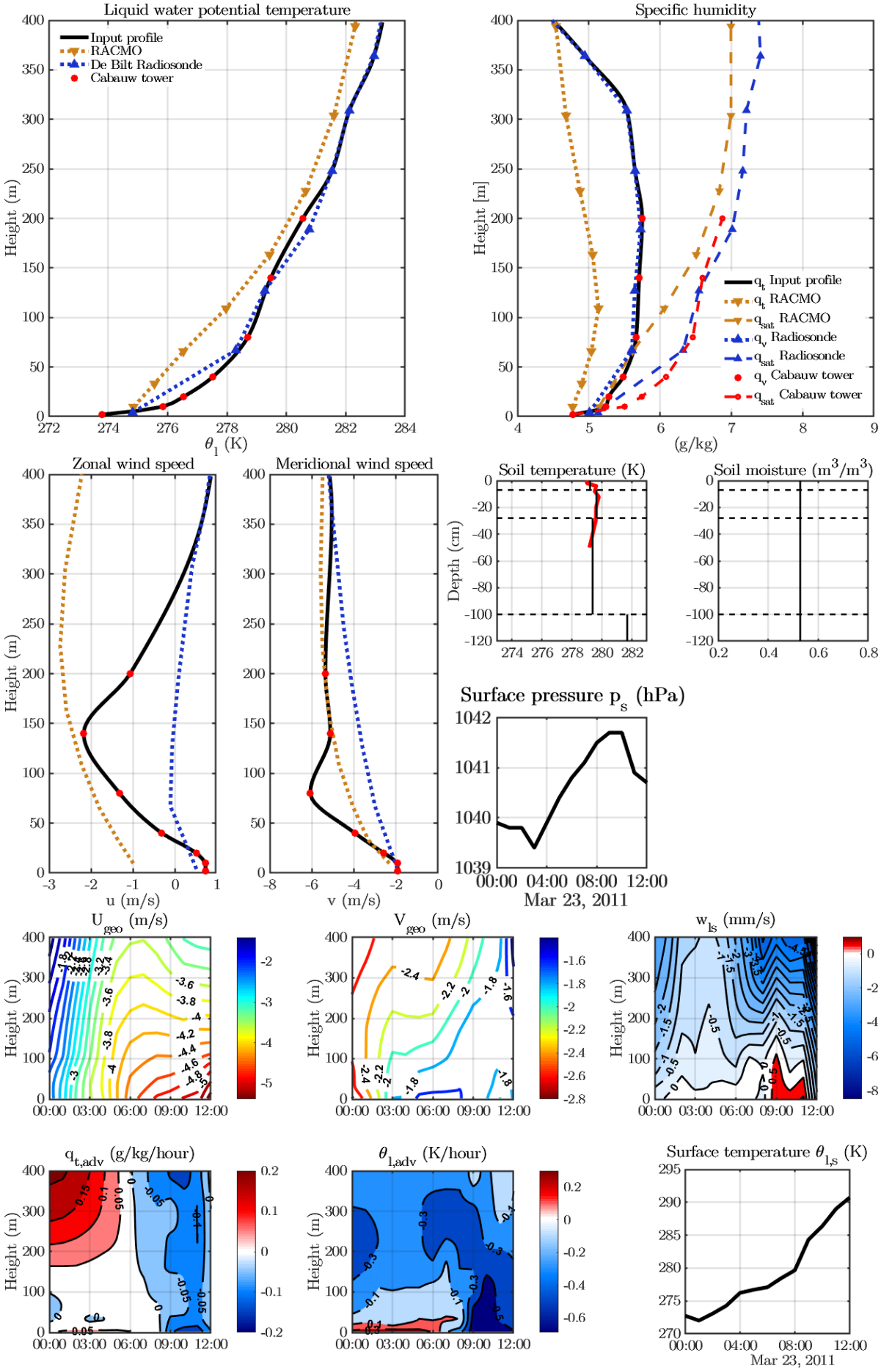

Figure E.3: Initial profiles for the radiation fog case on 23 March 2011 at 00:00. Time is in UTC. The initial profiles of potential temperature, specific humidity and wind vectors are compared against tower measurements at Cabauw, radiosonde measurements from De Bilt and RACMO model data (top & middle-left panel). Initial soil temperatures and volumetric soil moisture are shown in the medium right panels. Bottom panels show the time-varying large-scale forcings, taken from RACMO.

F

Running DALES as an offline land surface model

Introduction

This document explains how to use DALES as an offline, uncoupled, land surface model. It is important that the reader first becomes familiar with the DALES code and it's installation on the local server. For this purpose the following documents might prove very useful:

- *Introduction to DALES v3.1*
  `http://www.srderoode.nl/Students/Dales_manual.pdf`
- *Formulation and numerical studies by the Dutch Atmospheric Large-Eddy Simulation (DALES)*
  `http://www.geosci-model-dev.net/3/415/2010/gmd-3-415-2010.pdf`
- *Getting started with UNIX & DALES*
  `http://bit.ly/1kFbdUQ`
- *Overview of all namoptions in DALES*
  `https://github.com/dalesteam/dales/tree/master/utils/doc/input`

Installation of the land surface model

Before compiling the DALES source code, some modifications need to be implemented in the *program.f90* main file. The offline land surface model does not require most of the calculations implemented in DALES, such as the dynamical core or the radiation code, but only requires the land surface modules written in the *modsurface.f90* file. The main source code file (*program.f90*) hence becomes much simpler. An example is shown in figure F.1.

As you might notice, the source code requires a new **modcolumn** module. This module contains the subroutines that initialise the useful variables (*initcolumn* & *inittimestatcolumn*), then read the atmospheric forcing and the land surface parameters from the input files (*timedepcolumn*), and finally write the calculated variables in the output files (*timestatcolumn*).

Once the *program.f90* is modified and the *modcolumn.f90* is added to the source code directory, the program is ready to be compiled. First, create a new DALES build directory, move to this directory and type:

```
cmake source code directory
```

Then compile DALES:

```
make
```

After compilation, an executable program *dales4* is written in the build/src directory.

```
program DALES      !Version 4.0.0alpha

!!-----------------------------------------------------------------
!!     0.0    USE STATEMENTS FOR CORE MODULES
!!-----------------------------------------------------------------
  use modglobal,         only : rk3step,timeleft
  use modstartup,        only : startup
  use modsurface,        only : surface
  use modcolumn
!-----------------------------------------------------------------

  implicit none

!-----------------------------------------------------------------
!     1      READ NAMELISTS,INITIALISE GRID, CONSTANTS AND FIELDS
!-----------------------------------------------------------------
    call startup
!-----------------------------------------------------------
!      2     INITIALIZE STATISTICAL ROUTINES AND ADD-ONS
!-----------------------------------------------------------
  call initcolumn  ! initialize variables
  call inittimestatcolumn ! initialize output
!-----------------------------------------------------
!   3.0   MAIN TIME LOOP
!-----------------------------------------------------
    do while (timeleft>0 .or. rk3step < 3)
    call tstep_update  ! Calculate new timestep
    call timedepcolumn ! Interpolate forcing and parameters
!-----------------------------------------------------
!   3.2   THE SURFACE LAYER
!-----------------------------------------------
     call surface  ! Land surface model calculations
!-----------------------------------------------------
!   3.7  WRITE RESTARTFILES AND DO STATISTICS
!-----------------------------------------------------
    call timestatcolumn ! write output
    end do
!-----------------------------------------------------------
!    4    FINALIZE ADD ONS AND THE MAIN PROGRAM
!-----------------------------------------------------------
call exittimedepcolumn

end program DALES
```

Figure F.1: DALES main file *program.f90* adapted for offline land surface simulations

Input files

namoptions.expnr

The *namoptions* file contains the most important model parameters for DALES simulations. For offline land surface simulations, most parameters will not be used so any value can be written. However the following parameters need to be carefully defined:

- `iexpnr` : number of the experiments (e.g 031)
- `runtime` : length of the simulation, in seconds (e.g. 31492200 for a yearly run)
- `dtmax` : maximum length of timestep, in seconds (e.g 600s for 10-min forcing)
- `nsv` : number of scalar variables (must be set to **2**)
- `itot & jtot` : horizontal grid size (must be set to **2** at least)
- `kmax` : vertical grid size (e.g 4, must be compatible with the input profiles)
- `imicro` : switch for microphysics module (must be set to **2**)
- `iradiation` : switch for radiation module (must be set to **2** or **10**)
- `isurf` : switch for the surface module (must be set to **1**)

- `l_vg` : switch for van Genuchten parametization (can be .true. or .false.)

Every other parameter is taken from the input files and do not need to be given in the *namoptions* (any value can be used in order to avoid error messages).

Note: The initial profiles of soil temperature and volumetric soil moisture are given in the **modcolumn.f90** file, and must be changed manually before compiling the code.

prof.inp.expnr scalar.inp.expnr lscale.inp.expnr

The **modstartup** requires these input files, even tough they are not used by the surface model. Only the level of the first model level is important to tune as it is the level, assumed in the surface layer, where the surface fluxes are computed. Hence any initial profile can be written here, as long as the number of levels matches the k_{max} in the *namoptions* file.

forcing_atm.inp.expnr

The *forcing_atm.inp.expnr* file is a tab-delimited file with 14 columns containing on each line the atmospheric forcing at a certain time. It does not contain any headers or text, and the format is the following:

time (s)	$SW_{\downarrow}$ (W/m^2)	$SW_{\uparrow}$ (W/m^2)	$LW_{\downarrow}$ (W/m^2)	$LW_{\uparrow}$ (W/m^2)	p_s (Pa)	p_0 (Pa)	θ_{l0} (K)	θ_{ls} (K)	q_{t0} (kg/kg)	q_{l0} (kg/kg)	u_0 (m/s)	v_0 (m/s)	P (kg/m^2/s)
0.00000	137.27963	36.15360	261.42902	324.83148	103169.99512	103144.53232	273.81705	274.05181	0.00380	0.00000	2.97471	5.81309	0.00000
600.00000	215.32834	61.90338	263.03583	328.42609	103159.99756	103134.58365	274.32021	274.81446	0.00383	0.00000	2.96746	5.74935	0.00000
1200.00000	162.71878	43.26932	269.35321	327.66156	103169.99512	103144.57874	274.31261	274.64678	0.00383	0.00000	3.89114	5.35569	0.00000
1800.00000	131.48491	33.05357	275.32013	327.03540	103159.99756	103134.57404	274.22109	274.52308	0.00380	0.00000	3.44757	5.30878	0.00000
2400.00000	115.94804	28.71652	279.78485	326.74954	103150.00000	103124.58814	274.32780	274.47067	0.00380	0.00000	3.36320	5.59730	0.00000
3000.00000	103.49119	25.65424	275.49896	325.96280	103150.00000	103124.57853	274.22868	274.30530	0.00378	0.00000	3.76185	5.31306	0.00000
3600.00000	106.01967	26.11177	270.67361	325.58737	103140.00244	103114.57425	274.13715	274.23388	0.00378	0.00000	3.61961	5.63812	0.00000
4200.00000	105.32689	26.02722	271.49948	325.90753	103109.99756	103084.58682	274.25907	274.32408	0.00383	0.00000	2.58453	5.88771	0.00000
4800.00000	95.54275	23.76781	268.68491	325.29913	103100.00000	103074.58212	274.16753	274.20356	0.00381	0.00000	2.56041	5.83277	0.00000
5400.00000	101.63579	26.17769	267.34970	325.43649	103100.00000	103074.58254	274.16753	274.23250	0.00383	0.00000	2.26091	5.19973	0.00000
6000.00000	93.33424	23.50080	268.34958	325.24493	103080.00488	103054.59237	274.18273	274.20733	0.00383	0.00000	2.58307	5.41551	0.00000
6600.00000	75.86094	18.22449	271.89233	324.75409	103050.00000	103024.59405	274.20553	274.12662	0.00378	0.00000	2.34297	6.00941	0.00000
7200.00000	67.45350	16.03312	276.98444	324.63242	103019.99512	102994.59700	274.22835	274.12374	0.00381	0.00000	1.69607	6.60574	0.00000

Figure F.2: First lines of a *forcing_atm.inp.expnr* file

The model linearly interpolates the forcing between each timestep.

parameters.expnr

The *parameters.expnr* file is a tab-delimited file with 23 columns containing on each line several soil and vegetation parameters at a certain time. It does not contain any headers or text, and the format is the following:

time (s)	z_{0h} (m)	z_{0m} (m)	LAI (m^2/m^2)	$r_{s,min}$ (s/m)	$r_{s,soil,min}$ (s/m)	c_{veg} (-)	$T_{soil,deep}$ (K)	gD (Pa^{-1})	Λ_{skin} (W/m^2/s)	C_{skin} (J/m^2/K)	$R1$ (-)

$R2$ (-)	$R3$ (-)	$R4$ (-)	θ_{sat} (m^3/m^3)	θ_{fc} (m^3/m^3)	θ_{wp} (m^3/m^3)	n_{vg} (-)	L_{vg} (-)	α_{vg} (m^{-1})	θ_r (m^3/m^3)	$\gamma_{h,sat}$ (m/s)

The model linearly interpolates the parameters between each timestep. At least two lines need to be written in the file, but the lines can be be identical (except for the first column) for simulations requiring constant parameters.

Output files

tmatm.expnr

The *tmatm.expnr* is a tab-delimited file made of 13 columns with two header lines. It contains the atmospheric forcing used by the model, and can thus be used to check if the right atmospheric forcing was used by the model.

```
#  time     swd     swu     lwd     lwu      ps       pa      thl0    thls    qt0      ql0      u0      v0
#  [s]     [W/m2]  [W/m2]  [W/m2]  [W/m2]   [Pa]     [Pa]     [K]     [K]     [kg/kg]  [kg/kg] [m/s]   [m/s]
       600.00      215.33       61.90      263.04      328.43 1.032E+05 1.031E+05      274.32      279.46  0.383E-02  0.000E+00         3.0         5.7
      1200.00      162.72       43.27      269.35      327.66 1.032E+05 1.031E+05      274.31      278.04  0.383E-02  0.000E+00         3.9         5.4
      1800.00      131.48       33.05      275.32      327.04 1.032E+05 1.031E+05      274.22      277.42  0.380E-02  0.000E+00         3.4         5.3
      2400.00      115.95       28.72      279.78      326.75 1.032E+05 1.031E+05      274.33      277.00  0.380E-02  0.000E+00         3.4         5.6
      3000.00      103.49       25.65      275.50      325.96 1.032E+05 1.031E+05      274.23      276.20  0.378E-02  0.000E+00         3.8         5.3
      3600.00      106.02       26.11      270.67      325.59 1.031E+05 1.031E+05      274.14      275.98  0.378E-02  0.000E+00         3.6         5.6
```

Figure F.3: First lines of a *tmatm.expnr* file

tmpar.expnr

The *tmpar.expnr* file is a tab-delimited file made of 23 columns with one header line. It contains the soil and vegetation parameters and can thus be used to check if the right parameters were used by the model.

```
#  time     z0h     z0m   LAI  rsmin     rssoilmin  cveg tsoildeep gD lambdaskin      Cskin  R1  R2   R3  R4  phi  phifc  phiwp
    n    l   alpha    phir    gammasat
      600.00      0.000006766      0.043300000      2.000000000    110.000000000     50.000000000      1.000000000    283.810000000      0.000000000      8.000000000      0.000000000      0.400000000      0.300000000
0.300000000      0.000000000      0.590000000      0.528000000      0.320000000      1.110000000     -5.901000000      1.950000000      0.010000000      0.000000520
      1200.00      0.000006766      0.043300000      2.000000000    110.000000000     50.000000000      1.000000000    283.810000000      0.000000000      8.000000000      0.000000000      0.400000000      0.300000000
0.300000000      0.000000000      0.590000000      0.528000000      0.320000000      1.110000000     -5.901000000      1.950000000      0.010000000      0.000000520
      1800.00      0.000006766      0.043300000      2.000000000    110.000000000     50.000000000      1.000000000    283.810000000      0.000000000      8.000000000      0.000000000      0.400000000      0.300000000
0.300000000      0.000000000      0.590000000      0.528000000      0.320000000      1.110000000     -5.901000000      1.950000000      0.010000000      0.000000520
      2400.00      0.000006766      0.043300000      2.000000000    110.000000000     50.000000000      1.000000000    283.810000000      0.000000000      8.000000000      0.000000000      0.400000000      0.300000000
0.300000000      0.000000000      0.590000000      0.528000000      0.320000000      1.110000000     -5.901000000      1.950000000      0.010000000      0.000000520
      3000.00      0.000006766      0.043300000      2.000000000    110.000000000     50.000000000      1.000000000    283.810000000      0.000000000      8.000000000      0.000000000      0.400000000      0.300000000
0.300000000      0.000000000      0.590000000      0.528000000      0.320000000      1.110000000     -5.901000000      1.950000000      0.010000000      0.000000520
      3600.00      0.000006766      0.043300000      2.000000000    110.000000000     50.000000000      1.000000000    283.810000000      0.000000000      8.000000000      0.000000000      0.400000000      0.300000000
```

Figure F.4: First lines of a *tmpar.expnr* file

tmlsm.expnr

The *tmlsm.expnr* file is a tab-delimited file made of 18 columns with two header lines. It contains the output of the land surface model, such as the surface fluxes, the skin potential temperature, the surface resistances and the stress functions. The format is the following:

time	Q_{net}	LE	H	G_0	r_s	r_a	θ_{ls}	q_s	c_{liq}	W_l	$r_{s,soil}$
(s)	(W/m^2)	(W/m^2)	(W/m^2)	(W/m^2)	(s/m)	(s/m)	(K)	(kg/kg)	(-)	(m)	(s/m)

$r_{s,veg}$	f_1	$f_{2,veg}$	$f_{2,soil}$	f_3	f_4
(s/m)	(-)	(-)	(-)	(-)	(-)

```
#  time     Qnet     H    LE   G0      rs   ra tskin qskin cliq      Wl   rssoil   rsveg    f1  f2veg f2soil   f3   f4
#  [s]     [W/m2]  [W/m2]  [W/m2]  [W/m2]   [K]     [kg/kg]   [s/m]   [s/m]   [K]     [-]    [m]     [s/m]   [s/m]   [-]     [-]      [-]     [-]     [-]
      600.00     87.90     29.70     17.78     40.43    0.328E+03    0.230E+03    279.46    0.203E-01 0.00     0.123E-07    0.500E+02     0.328E+03     0.165E+01     0.100E+01     0.100E+01     0.100E+01     0.360E+01
     1200.00     61.22     20.44     12.61     28.17    0.378E+03    0.243E+03    278.04    0.190E-01 0.00     0.121E-07    0.500E+02     0.378E+03     0.191E+01     0.100E+01     0.100E+01     0.100E+01     0.360E+01
     1800.00     46.75     14.64      9.71     22.40    0.436E+03    0.291E+03    277.42    0.186E-01 0.00     0.119E-07    0.500E+02     0.436E+03     0.215E+01     0.100E+01     0.100E+01     0.100E+01     0.369E+01
     2400.00     40.29     13.00      8.87     18.42    0.457E+03    0.274E+03    277.00    0.181E-01 0.00     0.117E-07    0.500E+02     0.457E+03     0.231E+01     0.100E+01     0.100E+01     0.100E+01     0.360E+01
     3000.00     27.41      8.96      6.94     11.51    0.501E+03    0.294E+03    276.20    0.176E-01 0.00     0.116E-07    0.500E+02     0.501E+03     0.247E+01     0.100E+01     0.100E+01     0.100E+01     0.369E+01
     3600.00     25.00      8.98      6.69      9.34    0.507E+03    0.274E+03    275.98    0.173E-01 0.00     0.114E-07    0.500E+02     0.507E+03     0.243E+01     0.100E+01     0.100E+01     0.100E+01     0.379E+01
     4200.00     24.89      8.21      6.53     10.14    0.496E+03    0.306E+03    276.14    0.177E-01 0.00     0.113E-07    0.500E+02     0.496E+03     0.244E+01     0.100E+01     0.100E+01     0.100E+01     0.369E+01
     4800.00     15.19      5.40      5.18      4.61    0.540E+03    0.330E+03    275.49    0.173E-01 0.00     0.112E-07    0.500E+02     0.540E+03     0.259E+01     0.100E+01     0.100E+01     0.100E+01     0.379E+01
     5400.00     17.35      4.99      5.02      7.34    0.520E+03    0.453E+03    275.86    0.181E-01 0.00     0.111E-07    0.500E+02     0.520E+03     0.250E+01     0.100E+01     0.100E+01     0.100E+01     0.379E+01
     6000.00     12.96      4.39      4.67      3.90    0.548E+03    0.394E+03    275.47    0.175E-01 0.00     0.111E-07    0.500E+02     0.548E+03     0.263E+01     0.100E+01     0.100E+01     0.100E+01     0.379E+01
     6600.00      4.80      2.52      3.95     -1.66    0.622E+03    0.333E+03    274.82    0.167E-01 0.00     0.110E-07    0.500E+02     0.622E+03     0.299E+01     0.100E+01     0.100E+01     0.100E+01     0.379E+01
     7200.00      3.78      2.51      3.74     -2.47    0.670E+03    0.283E+03    274.75    0.165E-01 0.00     0.109E-07    0.500E+02     0.670E+03     0.322E+01     0.100E+01     0.100E+01     0.100E+01     0.379E+01
     7800.00     -3.79     -0.04      3.11     -6.86    0.697E+03    0.283E+03    274.22    0.162E-01 0.00     0.108E-07    0.500E+02     0.697E+03     0.334E+01     0.100E+01     0.100E+01     0.100E+01     0.379E+01
```

Figure F.5: First lines of a *tmlsm.expnr* file

tmsoil.expnr

The *tmsoil.expnr* file is a tab-delimited file made of 19 columns with two header lines. It contains the soil temperatures, the soil volumetric water contents and the soil thermal and hydraulic conductivities at the half levels. The format is the following:

time (s)	T_1 (K)	T_2 (K)	T_3 (K)	T_4 (K)	θ_1 (m^3/m^3)	θ_2 (m^3/m^3)	θ_3 (m^3/m^3)	θ_4 (m^3/m^3)	$\lambda_{T,1+1/2}$ (W/m/K)	$\lambda_{T,2+1/2}$ (W/m/K)	$\lambda_{t,3+1/2}$ (W/m/K)

$\lambda_{T,4+1/2}$ (W/m/K)	$\lambda_{h,1+1/2}$ (m^2/s)	$\lambda_{h,2+1/2}$ (m^2/s)	$\lambda_{h,3+1/2}$ (m/s)	$\gamma_{h,1+1/2}$ (m/s)	$\gamma_{h,2+1/2}$ (m/s)	$\gamma_{h,3+1/2}$ (m/s)

```
#  time     T1     T2   T3    T4      phiw1     phiw2  phiw3   phiw4   lambdah1      lambdah2     lambdah3     lambdah4
   lambdash1   lambdash2     lambdash3   gammash1      gammash2     gammash3
#  [s]      [K]  [K]  [K]  [K]   [m3/m3]      [m3/m3]   [m3/m3]   [m3/m3]     [W/m/K]     [W/m/K]   [W/m/K]   [W/m/K]
   [W/m/K]     [W/m/K]   [W/m/K]     [m/s]       [m/s]     [m/s]
      600.00  276.90  277.82  279.64  284.00  0.5799  0.5849  0.5899  0.5900    0.139E+01    0.139E+01    0.140E+01    0.140E+01    0.207E-06    0.424E-06    0.892E-06    0.182E-07    0.461E-07    0.130E-06
     1200.00  277.01  277.81  279.64  284.00  0.5798  0.5848  0.5898  0.5900    0.139E+01    0.139E+01    0.140E+01    0.140E+01    0.205E-06    0.422E-06    0.892E-06    0.180E-07    0.425E-07    0.115E-06
     1800.00  277.10  277.81  279.64  284.00  0.5797  0.5847  0.5898  0.5900    0.139E+01    0.139E+01    0.140E+01    0.140E+01    0.204E-06    0.420E-06    0.892E-06    0.179E-07    0.405E-07    0.106E-06
     2400.00  277.16  277.81  279.64  284.00  0.5796  0.5847  0.5897  0.5900    0.139E+01    0.139E+01    0.140E+01    0.140E+01    0.202E-06    0.418E-06    0.892E-06    0.177E-07    0.390E-07    0.100E-06
     3000.00  277.22  277.81  279.64  284.00  0.5795  0.5846  0.5897  0.5899    0.139E+01    0.139E+01    0.140E+01    0.140E+01    0.201E-06    0.416E-06    0.892E-06    0.176E-07    0.379E-07    0.955E-07
     3600.00  277.26  277.81  279.64  284.00  0.5794  0.5845  0.5896  0.5899    0.139E+01    0.139E+01    0.140E+01    0.140E+01    0.199E-06    0.414E-06    0.892E-06    0.175E-07    0.369E-07    0.918E-07
     4200.00  277.30  277.81  279.64  283.99  0.5793  0.5845  0.5896  0.5899    0.139E+01    0.139E+01    0.140E+01    0.140E+01    0.198E-06    0.413E-06    0.892E-06    0.173E-07    0.361E-07    0.887E-07
```

Figure F.6: First lines of a *tmsoil.expnr* file

tmwb.expnr

The *tmwb.expnr* file is a tab-delimited file made of 8 columns with two header lines. It contains the water mass fluxes involved in the surface water balance (precipitation, evapotranspiration, interception, throughfall, infiltration and runoff) and the water flux at the soil bottom. The format is the following:

time (s)	P ($kg/m^2/s$)	LE ($kg/m^2/s$)	P_I ($kg/m^2/s$)	T ($kg/m^2/s$)	I ($kg/m^2/s$)	Y ($kg/m^2/s$)	F_{deep} ($kg/m^2/s$)

```
#  time     P    LE     Inter     Tr     Inf     Ysfc    Fdeep
#  [s]       [kg/m2/s]    [kg/m2/s]    [kg/m2/s]    [kg/m2/s]    [kg/m2/s]    [kg/m2/s]     [kg/m2/s]
      600.00     0.00000E+00     0.70267E-05     0.00000E+00     0.00000E+00     0.00000E+00     0.00000E+00    -0.16718E-03
     1200.00     0.00000E+00     0.49855E-05     0.00000E+00     0.00000E+00     0.00000E+00     0.00000E+00    -0.15020E-03
     1800.00     0.00000E+00     0.38382E-05     0.00000E+00     0.00000E+00     0.00000E+00     0.00000E+00    -0.14033E-03
     2400.00     0.00000E+00     0.35048E-05     0.00000E+00     0.00000E+00     0.00000E+00     0.00000E+00    -0.13339E-03
     3000.00     0.00000E+00     0.27412E-05     0.00000E+00     0.00000E+00     0.00000E+00     0.00000E+00    -0.12804E-03
     3600.00     0.00000E+00     0.26459E-05     0.00000E+00     0.00000E+00     0.00000E+00     0.00000E+00    -0.12369E-03
     4200.00     0.00000E+00     0.25818E-05     0.00000E+00     0.00000E+00     0.00000E+00     0.00000E+00    -0.12004E-03
```

Figure F.7: First lines of a *tmwb.expnr* file

Job files

job.expnr

The jobscript in the *job.expnr* file contains the bash commands required for executing the DALES executable. The input files may be required in many different experiments, hence it is recommended to store all the input files in the so called "Cases" directory. Then the jobscript can be used to copy the specific input files for a given experiment. In the case many different experiments need to be executed at the same time (for instance, varying the LAI in small increments), then it might be useful to use a short scripts that call all the jobscripts The recommended structure with the job files is shown in the following figure:

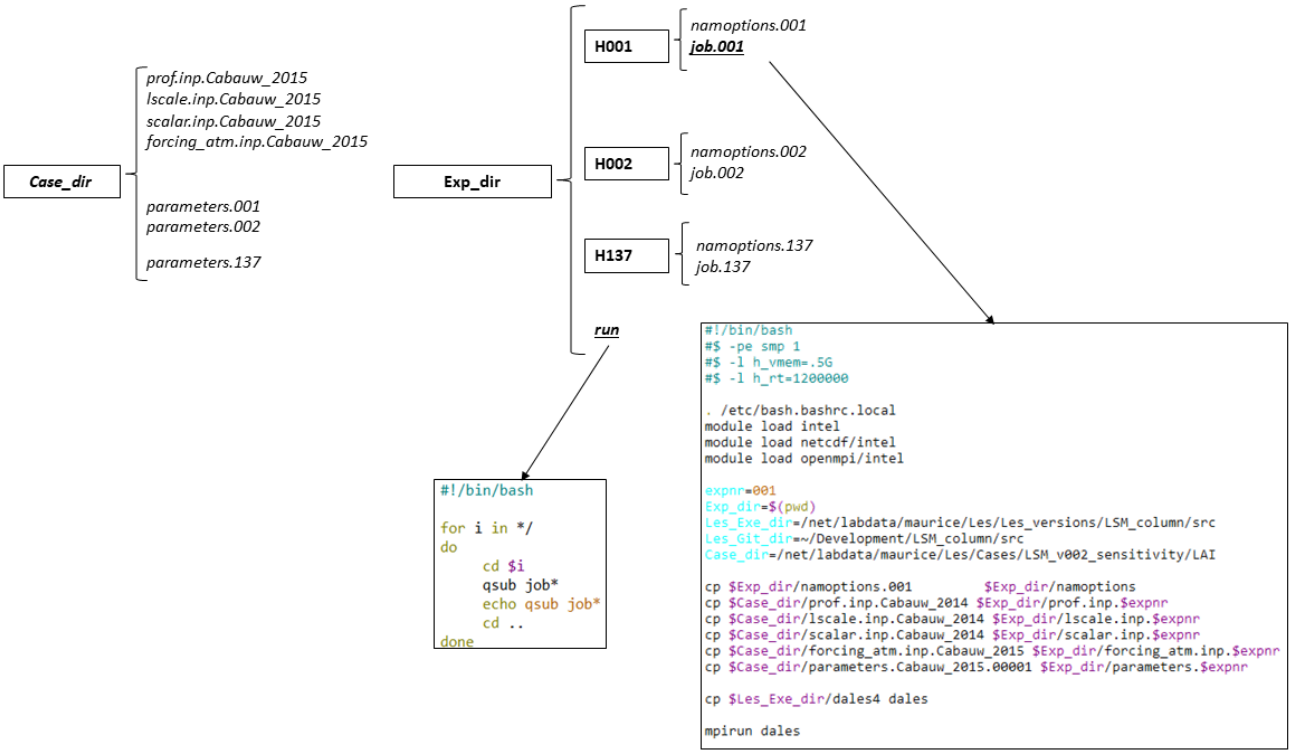

Figure F.8: Recommended server structure for many offline land surface model experiments

The master job file, *run*, needs to be made executable:

```
chmod a+rx run
```

Then execute the master job file:

```
./run
```

This will run all the jobfiles from all the experiments at the same time.

G

Parametrization of the skin thermal conductivity

In the land surface model, the soil temperature and the surface (radiative) temperature are connected through the *skin heat conductivity* parameter Λ_{skin}, expressed in W/m^2/K, and set to a constant value that typically depends on the soil cover (high vegetation, low vegetation, snow, etc...). Consequently, Λ_{skin} indirectly contains physical heat transfer processes that are not represented in the model, such as in-canopy radiative transfer, heat conduction within the grass layer and the organic layer (dead leaves, roots, plat stem tissue), etc.. (see figure G.1).

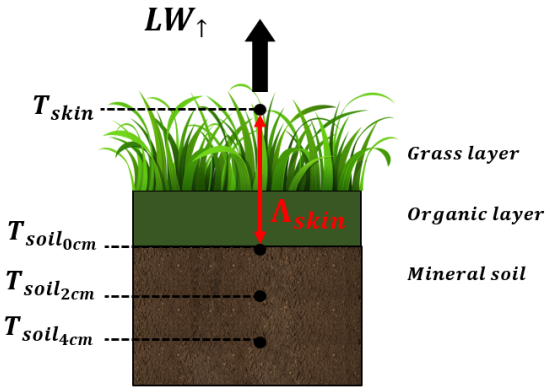

Figure G.1: Schematic representation of the soil/vegetation/atmosphere thermal coupling at the CESAR site

It was shown in this report that using different values of Λ_{skin}, ranging from 5 W/m^2/K to 20 W/m^2/K, has a strong effect on the daily cycle of the surface (skin) temperature (see figure 5.7 and 5.8). There is however, to our knowledge, not a lot of literature that discusses the physical authenticity and the numerical values of this parameter, and whether keeping it as a constant value is realistic or not. Verhoef and Vidale (2012) have shown using data from the CESAR site, that it may even become negative during day-night transitions. This is consistent with our results (see figure 4.11) using a similar approach but with a longer dataset ranging from 2004 to 2016.

The ground heat flux is typically parameterized as:

$$G_0 = \Lambda_{\text{skin}}(T_s - T_1) \tag{G.1}$$

where T_s is the surface temperature and T_1 is the temperature in the first soil layer. This means that a with a negative Λ_{skin}, there is a counter-gradient flux: 'the heat flows towards the higher temperature'. This is not what one would expect from molecular heat diffusion. The next part aims to give a possible explanation for this 'artificial' negative heat conductivity.

If we assume that the soil column is homogeneous, that horizontal heat conduction may be ignored and that there are no sources of heat within the soil itself (e.g water phase changes), then the Fourier equation of heat conduction may be written:

$$\frac{\partial T}{\partial t} = D_h \frac{\partial^2 T}{\partial z^2} \tag{G.2}$$

where z is the downwards vertical direction. The soil heat diffusivity, D_h (m^2/s) is defined as:

$$D_h \equiv \frac{\lambda_T}{(\rho C)} \tag{G.3}$$

with λ_T the soil heat conductivity (W/m/K) and (ρC) the volumetric soil heat capacity (J/m^3/K).

We assume that the temperature at the surface (z=0) is given by:

$$T(0,t) = \overline{T} + A_0 \sin(\omega t) \tag{G.4}$$

where $\omega = 2\pi/86400$(rad/s) represents the diurnal cycle oscillation, $\overline{T}$ is the daily mean temperature and A_0 is the diurnal amplitude of the surface temperature. For this case, the soil temperature at any depth is written (van Wijk, 1963):

$$T(z,t) = \overline{T} + A_z\left[\sin\left(\omega t + \phi(z)\right)\right] \tag{G.5}$$

where d is the damping depth and $\phi(z)$ is the phase shift. Substituting G.5 in the heat equation G.2 gives the following results:

$$\begin{aligned} \phi(z) &= -z/d \\ A_z &= A_0 e^{-z/d} \end{aligned} \tag{G.6}$$

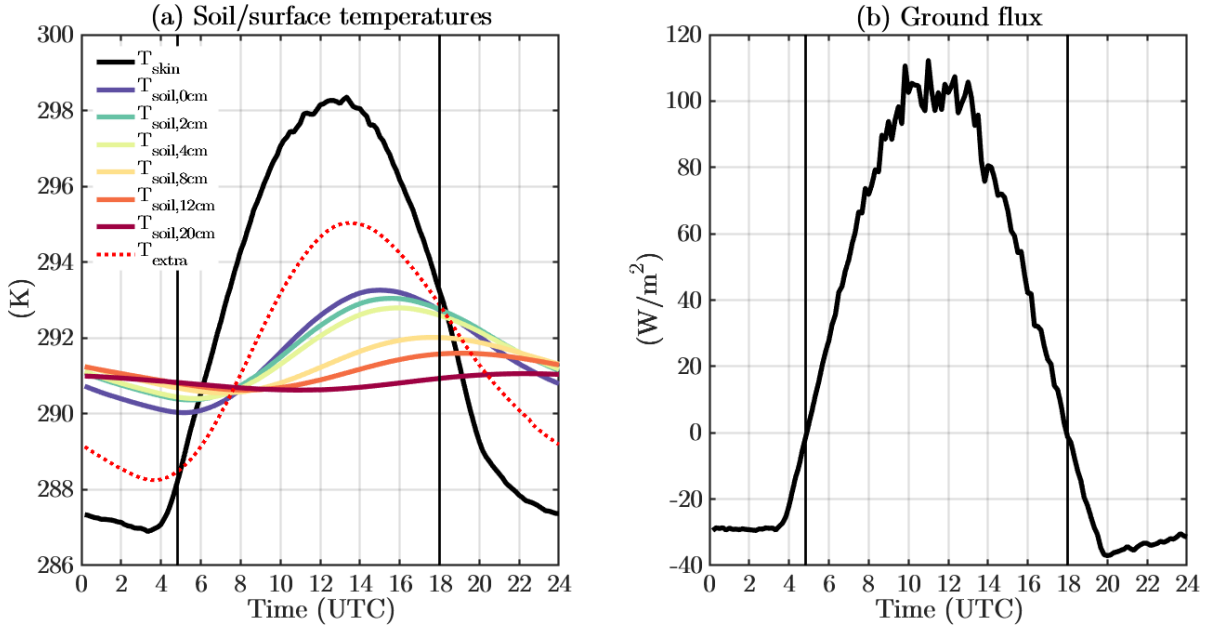

Figure G.2: Observed monthly mean of the daily variation in (a) soil and surface temperatures and (b) surface energy balance residual for the CESAR site in July, using data in the 2004-2016 period. The vertical lines represent the times when the ground flux changes sign, and the T_{extra} temperature is the $T_{soil,0cm}$ temperature advanced by 90min and amplified by a factor 2.1.

where the damping depth is a function of the heat diffusivity and forcing frequency:

$$d = (2D_h/\omega)^{1/2} \tag{G.7}$$

This means that the temperature at any depth may be written as:

$$T(z,t) = \overline{T} + \frac{A_0}{e^{z/d}}\,[\sin(\omega t - z/d)] \tag{G.8}$$

The soil heat flux (positive downwards) is defined as:

$$F_T \equiv -\lambda_T \frac{\partial T}{\partial z} \tag{G.9}$$

Using equation G.8 and,

$$\sin\alpha + \sin\beta = 2\sin\frac{1}{2}(\alpha+\beta)\cos\frac{1}{2}(\alpha-\beta) \tag{G.10}$$

the soil heat flux may be written:

$$\begin{aligned} F_T &= \frac{\lambda_T A_0}{d}\,[\sin(\omega t - z/d) + \cos(\omega t - z/d)]\,e^{-z/d} \\ &= \frac{\lambda_T A_0}{d}\,[\sin(\omega t - z/d) + \sin(\omega t - z/d + \pi/2)]\,e^{-z/d} \\ &= 2\frac{\lambda_T A_0}{d}\,[\sin(\omega t - z/d + \pi/4) + \cos(-\pi/4)]\,e^{-z/d} \\ &= \sqrt{2}\frac{\lambda_T A_0}{d}\,[\sin(\omega t - z/d + \pi/4)]\,e^{-z/d} \end{aligned} \tag{G.11}$$

In practice, the soil temperatures are always taken at a certain depth z_1, which means that they are never taken in the layer that is in direct thermal contact with the surface. Consequently, this measurement is damped by a factor $e^{-z_1/d}$ and delayed by $-z_1/d$ rad compared to the observed surface temperature.

Surprisingly, advancing the observed soil temperature at 0cm by **90min**, and amplifying it by a factor **2.1** gives a daily variation in surface/soil temperature differences that is more consistent with the estimated ground heat flux (figure G.2), e.g the ground heat flux is positive (resp. negative) when the surface is warmer (resp. colder) than the 'extrapolated' soil temperature.

This is a strong indication that an artificial negative Λ_{skin} can be obtained by subtracting delayed and damped soil temperature measurements from the observed surface temperature. Correcting for this delay and dampening may in fact reduce the time period when Λ_{skin} is estimated below zero. The physical reason being that the measurements are never taken from a soil layer that is in direct thermal contact with the surface, hence heat diffusion delays and dampens the observed signal compared to the temperature we wish to estimate.

It is also interesting to notice that this correction also greatly reduces the temperature difference between the surface and the soil. This translates in higher estimated Λ_{skin} values, especially during night-time due to the fact that the observed magnitude of the ground

flux is much smaller than during day-time. For July, Λ_{skin} was found to be ranging between 17 W/m^2/s during night-time and 30 W/m^2/s during daytime (not shown), which is substantially more than previous estimates (figure 4.11)

It is in practice, however, challenging to find the proper phase difference and dampening factors as the soil properties are not homogeneous and change in time (change in water contents, vegetation growth, biological activity, etc...). Furthermore, day-night transitions occur at very small time-scales, but we are always limited by the temporal resolution of the measured soil temperature, surface temperature and ground flux.

Bibliography

Beljaars, A. C. M. and Bosveld, F. C. (1997), 'Cabauw data for the validation of land surface parameterization schemes', *Journal of Climate* **10**(6), 1172–1193.

Beljaars, A. C. M. and Holtslag, A. A. M. (1991), 'Flux parameterization over land surfaces for atmospheric models', *Journal of Applied Meteorology* **30**(3), 327–341.

Bengtsson, L., Andrae, U., Aspelien, T., Batrak, Y., Calvo, J., de Rooy, W., Gleeson, E., Hansen-Sass, B., Homleid, M., Hortal, M., Ivarsson, K.-I., Lenderink, G., Niemelä, S., Nielsen, K. P., Onvlee, J., Rontu, L., Samuelsson, P., Muñoz, D. S., Subias, A., Tijm, S., Toll, V., Yang, X. and Køltzow, M. Ø. (2017), 'The HARMONIE–AROME model configuration in the ALADIN–HIRLAM NWP system', *Monthly Weather Review* **145**(5), 1919–1935.

Boers, R., Baltink, H. K., Hemink, H. J., Bosveld, F. C. and Moerman, M. (2013), 'Ground-based observations and modeling of the visibility and radar reflectivity in a radiation fog layer', *Journal of Atmospheric and Oceanic Technology* **30**(2), 288–300.

Briegleb, B. P. (1992), 'Delta-eddington approximation for solar radiation in the NCAR community climate model', *Journal of Geophysical Research* **97**(D7), 7603.

Brown, R. N., Percivalle, C., Narkiewicz, S. and DeCuollo, S. (2010), 'Relative rooting depths of native grasses and amenity grasses with potential for use on roadsides in new england', *HortScience* **45**(3), 393–400.

Brutsaert, W. (1979), 'Heat and mass transfer to and from surfaces with dense vegetation or similar permeable roughness', *Boundary-Layer Meteorology* **16**(3), 365–388.

Campbell, G. S. (1974), 'A simple method for determining unsaturated conductivity from moisture retention data', *Soil Science* **117**(6), 311–314.

Canadell, J., Jackson, R. B., Ehleringer, J. B., Mooney, H. A., Sala, O. E. and Schulze, E.-D. (1996), 'Maximum rooting depth of vegetation types at the global scale', *Oecologia* **108**(4), 583–595.

Clapp, R. B. and Hornberger, G. M. (1978), 'Empirical equations for some soil hydraulic properties', *Water Resources Research* **14**(4), 601–604.

de Roode, S. R., Bosveld, F. C. and Kroon, P. S. (2010), 'Dew formation, eddy-correlation latent heat fluxes, and the surface energy imbalance at cabauw during stable conditions', *Boundary-Layer Meteorology* **135**(3), 369–383.

Deardorff, J. W. (1978), 'Efficient prediction of ground surface temperature and moisture, with inclusion of a layer of vegetation', *Journal of Geophysical Research* **83**(C4), 1889.

Dingman, S. (2015), *Physical Hydrology: Third Edition*, Waveland Press.

Duynkerke, P. G. (1992), 'The roughness length for heat and other vegetation parameters for a surface of short grass', *Journal of Applied Meteorology* **31**(6), 579–586.

ECMWF (2017), *Part IV: Physical Processes*, IFS Documentation Cy43R3, ECMWF.
URL: *https://www.ecmwf.int/en/elibrary/17736-part-iv-physical-processes*

Ek, M. B. and Holtslag, A. A. M. (2004), 'Evaluation of a land-surface scheme at cabauw', *Theoretical and Applied Climatology* **80**(2-4), 213–227.

Farouki, O. T. (1981), *Thermal Properties of Soils*, US Army Corps of Engineers, Cold Regions Research and Engineering Laboratory.

Heuff, F. (2016), Stratocumulus predictions with a large-eddy simulation model, Master's thesis, TU Delft.
URL: *https://repository.tudelft.nl/islandora/object/uuid:2ce21fdd-9e82-4605-8e33-16ebfc7e7655?collection=education*

Heus, T., van Heerwaarden, C. C., Jonker, H. J. J., Siebesma, A. P., Axelsen, S., van den Dries, K., Geoffroy, O., Moene, A. F., Pino, D., de Roode, S. R. and de Arellano, J. V.-G. (2010), 'Formulation of the dutch atmospheric large-eddy simulation (DALES) and overview of its applications', *Geoscientific Model Development* **3**(2), 415–444.

Jackson, R. B., Canadell, J., Ehleringer, J. R., Mooney, H. A., Sala, O. E. and Schulze, E. D. (1996), 'A global analysis of root distributions for terrestrial biomes', *Oecologia* **108**(3), 389–411.

Jager, C. J., Nakken, T. C. and Palland, C. L. (1976), Bodemkundig onderzoek van twee graslandpercelen nabij cabauw, Technical report, NV Heidemaatschappij Beheer.

Jarvis, P. (1976), 'The interpretation of the variations in leaf water potential and stomatal conductance found in canopies in the field', *Philosophical Transactions of the Royal Society of London B: Biological Sciences* **273**(927), 593–610.

Johansen, O. (1977), 'Thermal conductivity of soils'.

Le Moigne, P., Boone, A., Calvet, J., Decharme, B., Faroux, S., Gibelin, A., Lebeaupin, C., Mahfouf, J., Martin, E., Masson, V. et al. (2009), 'Surfex scientific documentation', *Note de centre (CNRM/GMME), Météo-France, Toulouse, France* .

Lohmann, U. and Feichter, J. (2005), 'Global indirect aerosol effects: a review', *Atmospheric Chemistry and Physics* **5**(3), 715–737.

Maronga, B. and Bosveld, F. C. (2017), 'Key parameters for the life cycle of nocturnal radiation fog: a comprehensive large-eddy simulation study', *Quarterly Journal of the Royal Meteorological Society* **143**(707), 2463–2480.

Masson, V., Champeaux, J.-L., Chauvin, F., Meriguet, C. and Lacaze, R. (2003), 'A global database of land surface parameters at 1-km resolution in meteorological and climate models', *Journal of Climate* **16**(9), 1261–1282.

Mira, M., Valor, E., Boluda, R., Caselles, V. and Coll, C. (2007), 'Influence of soil water content on the thermal infrared emissivity of bare soils: Implication for land surface temperature determination', *Journal of Geophysical Research* **112**(F4).

Moene, A. F. and van Dam, J. C. (2014), *Transport in the atmosphere-vegetation-soil continuum*, Cambridge University Press.

Mualem, Y. (1976), 'A new model for predicting the hydraulic conductivity of unsaturated porous media', *Water Resources Research* **12**(3), 513–522.

Peters-Lidard, C. D., Blackburn, E., Liang, X. and Wood, E. F. (1998), 'The effect of soil thermal conductivity parameterization on surface energy fluxes and temperatures', *Journal of the Atmospheric Sciences* **55**(7), 1209–1224.

Porporato, A., Laio, F., Ridolfi, L. and Rodriguez-Iturbe, I. (2001), 'Plants in water-controlled ecosystems: active role in hydrologic processes and response to water stress', *Advances in Water Resources* **24**(7), 725–744.

Russchenberg, H. (2005), 'Ground-based atmospheric remote sensing in the netherlands: European outlook', *IEICE Transactions on Communications* **E88-B**(6), 2252–2258.

Salisbury, J. W. and D'Aria, D. M. (1992), 'Emissivity of terrestrial materials in the 8–14 m atmospheric window', *Remote Sensing of Environment* **42**(2), 83–106.

Salisbury, J. W. and D'Aria, D. M. (1994), 'Emissivity of terrestrial materials in the 3–5 m atmospheric window', *Remote Sensing of Environment* **47**(3), 345–361.

Schuurbiers, M. (2014), Forecasting stratocumulus under a strong thermal inversion and in regions of subsidence, with a large-eddy simulation model, Master's thesis, TU Delft.

Seifert, A. and Beheng, K. D. (2001), 'A double-moment parameterization for simulating autoconversion, accretion and selfcollection', *Atmospheric Research* **59-60**, 265–281.

Seneviratne, S. I., Corti, T., Davin, E. L., Hirschi, M., Jaeger, E. B., Lehner, I., Orlowsky, B. and Teuling, A. J. (2010), 'Investigating soil moisture–climate interactions in a changing climate: A review', *Earth-Science Reviews* **99**(3-4), 125–161.

Stephens, G. L., Li, J., Wild, M., Clayson, C. A., Loeb, N., Kato, S., L'Ecuyer, T., Stackhouse, P. W., Lebsock, M. and Andrews, T. (2012), 'An update on earth's energy balance in light of the latest global observations', *Nature Geoscience* **5**(10), 691–696.

Stull, R. B., ed. (1988), *An Introduction to Boundary Layer Meteorology*, Springer Netherlands.

van Dam, J. C. (2000), *Field-scale water flow and solute transport: SWAP model concepts, parameter estimation and case studies*, [sn].

van den Hurk, B., Viterbo, P., Beljaars, A. and Betts, A. (2000), 'Offline validation of the era40 surface scheme', Shinfield Park, Reading.

van Genuchten, M. T. (1980), 'A closed-form equation for predicting the hydraulic conductivity of unsaturated soils1', *Soil Science Society of America Journal* **44**(5), 892.

van Meijgaard, E., van Ulft, L., van de Berg, W., Bosveld, F., van den Hurk, B., Lenderink, G. and Siebesma., A. (2008), 'The KNMI regional atmospheric climate model RACMO, version 2.1', *Koninklijk Nederlands Meteorologisch Instituut* **43**.

van Wijk, W. R. (1963), *Physics of Plant Environment*, John Wiley & Sons.

Verhoef, A. and Vidale, P. (2012), The role of skin layer heat transfer in the surface energy balance, *in* 'Workshop on Workshop on Diurnal cycles and the stable boundary layer, 7-10 November 2011', ECMWF, ECMWF, Shinfield Park, Reading, pp. 223–233.

Vilà-Guerau de Arellano, J., Ouwersloot, H. G., Baldocchi, D. and Jacobs, C. M. J. (2014), 'Shallow cumulus rooted in photosynthesis', *Geophysical Research Letters* **41**(5), 1796–1802.

Wösten, J., Veerman, G., de Groot, W. and Stolte, J. (2001), Waterretentie-en doorlatendheidskarakteristieken van boven-en ondergronden in nederland: de staringreeks; vernieuwde uitgave 2001, Technical report, Alterra.

Zeng, X. (2001), 'Global vegetation root distribution for land modeling', *Journal of Hydrometeorology* **2**(5), 525–530.